



AFRL-RI-RS-TR-2011-055

WAVEFORM DESIGN FOR MULTIMEDIA AIRBORNE NETWORKS

TEXAS ENGINEERING EXPERIMENT STATION

MARCH 2011

FINAL TECHNICAL REPORT

APPROVED FOR PUBLIC RELEASE; DISTRIBUTION UNLIMITED.

STINFO COPY

**AIR FORCE RESEARCH LABORATORY
INFORMATION DIRECTORATE**

NOTICE AND SIGNATURE PAGE

Using Government drawings, specifications, or other data included in this document for any purpose other than Government procurement does not in any way obligate the U.S. Government. The fact that the Government formulated or supplied the drawings, specifications, or other data does not license the holder or any other person or corporation; or convey any rights or permission to manufacture, use, or sell any patented invention that may relate to them.

This report is the result of contracted fundamental research deemed exempt from public affairs security and policy review in accordance with SAF/AQR memorandum dated 10 Dec 08 and AFRL/CA policy clarification memorandum dated 16 Jan 09. This report is available to the general public, including foreign nationals. Copies may be obtained from the Defense Technical Information Center (DTIC) (<http://www.dtic.mil>).

AFRL-RI-RS-TR-2011-055 HAS BEEN REVIEWED AND IS APPROVED FOR
PUBLICATION IN ACCORDANCE WITH ASSIGNED DISTRIBUTION STATEMENT.

FOR THE DIRECTOR:

/s/
STEPHEN REICHHART
Work Unit Manager

/s/
WARREN H. DEBANY JR., Technical Advisor
Information Grid Division
Information Directorate

This report is published in the interest of scientific and technical information exchange, and its publication does not constitute the Government's approval or disapproval of its ideas or findings.

REPORT DOCUMENTATION PAGE*Form Approved*
OMB No. 0704-0188

Public reporting burden for this collection of information is estimated to average 1 hour per response, including the time for reviewing instructions, searching data sources, gathering and maintaining the data needed, and completing and reviewing the collection of information. Send comments regarding this burden estimate or any other aspect of this collection of information, including suggestions for reducing this burden to Washington Headquarters Service, Directorate for Information Operations and Reports, 1215 Jefferson Davis Highway, Suite 1204, Arlington, VA 22202-4302, and to the Office of Management and Budget, Paperwork Reduction Project (0704-0188) Washington, DC 20503.

PLEASE DO NOT RETURN YOUR FORM TO THE ABOVE ADDRESS.**1. REPORT DATE (DD-MM-YYYY)**

March 2011

2. REPORT TYPE

Final Technical Report

3. DATES COVERED (From - To)

March 2009 – September 2010

4. TITLE AND SUBTITLE

WAVEFORM DESIGN FOR MULTIMEDIA AIRBORNE NETWORKS

Sub-Title:

ROBUST MULTIMEDIA DATA TRANSMISSION IN COGNITIVE RADIO NETWORKS

5a. CONTRACT NUMBER

FA8750-09-1-0151

5b. GRANT NUMBER

N/A

5c. PROGRAM ELEMENT NUMBER

62788F

6. AUTHOR(S)

Annamalai Annamalai

5d. PROJECT NUMBER

AN09

5e. TASK NUMBER

PV

5f. WORK UNIT NUMBER

AA

7. PERFORMING ORGANIZATION NAME(S) AND ADDRESS(ES)

Texas Engineering Experiment Station (TEES)

Prairie View A&M University

Prairie View, TX 77446

8. PERFORMING ORGANIZATION REPORT NUMBER**9. SPONSORING/MONITORING AGENCY NAME(S) AND ADDRESS(ES)**

Air Force Research Laboratory/Information Directorate

Rome Research Site/RIGF

525 Brooks Road

Rome NY 13441

10. SPONSOR/MONITOR'S ACRONYM(S)

AFRL/RI

11. SPONSORING/MONITORING AGENCY REPORT NUMBER

AFRL-RI-RS-TR-2011-055

12. DISTRIBUTION AVAILABILITY STATEMENT

Approved for Public Release; Distribution Unlimited. This report is the result of contracted fundamental research deemed exempt from public affairs security and policy review in accordance with SAF/AQR memorandum dated 10 Dec 08 and AFRL/CA policy clarification memorandum dated 16 Jan 09.

13. SUPPLEMENTARY NOTES

14. ABSTRACT: The concept of compressive sampling has the potential of overcoming the hardware limitations for wideband radio frequency spectrum sensing in cognitive radio applications. Adaptive-link cooperative relaying strategies could also dramatically improve the range, reliability, bandwidth efficiency and energy efficiency of wireless networks. This report first examines whether it is possible to protect the best basis function for effective reconstruction of different types of signals using a variety of compressive sensing algorithms. Subsequently, the feasibility of dynamic wideband spectrum sensing via two distinct compressive sensing techniques are investigated. Tight bounds for the link spectral efficiency of amplify-and-forward cooperative diversity networks with independent but non-identically distributed fading statistics are studied by deriving the ergodic capacity of three distinct adaptive transmission techniques. The proposed new mathematical framework allows system designers to gain insights as to how adaptive transmission policies, fade distributions and dissimilar fading statistics across the diversity paths affect the maximum transmission rate in a cooperative relay network. Analytical expressions are also derived for the achievable spectral efficiency and average bit error rate of amplify-and-forward cooperative diversity network with a practical discrete-rate adaptive modulation scheme over Nakagami-m channels.

15. SUBJECT TERMS

Compressive sampling, cognitive radio, cooperative relaying, ergodic capacity

16. SECURITY CLASSIFICATION OF:

a. REPORT

U

b. ABSTRACT

U

c. THIS PAGE

U

17. LIMITATION OF ABSTRACT

UU

18. NUMBER OF PAGES

101

19a. NAME OF RESPONSIBLE PERSON

STEPHEN P. REICHHART

19b. TELEPHONE NUMBER (Include area code)

N/A

TABLE OF CONTENTS

LIST OF FIGURES	iii
LIST OF TABLES.....	vi
1. INTRODUCTION AND SUMMARY	1
1.1 Introduction.....	1
2. COMPRESSIVE SENSING APPLICATION IN SPECTRUM ACCESS	2
2.1 Methods Assumptions and Procedures for Compressive Sensing Applications	2
2.1.1 Reconstruction (Sparsifying) Bases.....	2
2.1.2 Measurement (Sampling) Bases	4
2.1.3 Minimization Algorithms.....	5
2.2 Sparseness Measure of Signals for Compressive Sampling	7
2.2.1 Sparseness Measures.....	7
2.2.2 Results and Discussion of 1-D Compressive Sampling Signal Reconstruction without Noise	9
2.2.3 Results and Discussions of 1-D Compressive Sampling Signal Reconstruction with Noise	19
2.3 Nyquist folding analog-to-information receiver in fading environment.....	27
2.3.1 Nyquist Folding Analog-to-Information Receiver.....	28
2.3.2 Ricean Noise and Gaussian Noise	29
2.3.3 Automatic Detection Algorithm	30
2.3.4 Results and Discussions of Nyquist Folding A-2-I Receiver	31
2.4 Dynamic Spectrum Sensing Using Compressive Sensing Algorithms	33
2.4.1 Problem Statement.....	33
2.4.2 Results and Discussions of Dynamic Spectrum Sensing.....	34
3. ERGODIC CAPACITY OF COOPERATIVE AIRBORNE NETWORKS WITH ADAPTIVE SOURCE TRANSMISSION	55
3.1 Methods, Assumption and Procedures for Efficient Computation of Ergodic Capacity for Cooperative Relay Networks	55
3.2 System Model	57
3.3 Ergodic Capacity Computation in Fading Channels.....	60
3.3.1 Optimal Rate Adaptation with Fixed Transmit Power (ORA)	60
3.3.2 Channel Inversion with Fixed Rate (CIFR)	61
3.3.3 Optimal Power and Rate Adaptation (OPRA)	61
3.4 Adaptive M-QAM Modulation	63
3.4.1 Adaptive Scheme	63
3.5 Results and Discussions of Ergodic Capacity of Cooperative Networks	65
3.5.1 Ergodic Capacity of Cooperative Relay Networks	65
3.5.2 Adaptive M-QAM Modulation in Cooperative Relay Networks.....	74
4. CONCLUSIONS.....	79
5. REFERENCES	81
APPENDIX A.....	85
APPENDIX B	85
APPENDIX C	86
APPENDIX D.....	87

PUBLICATIONS.....	88
LIST OF ABBREVIATIONS.....	90

LIST OF FIGURES

Figure 1 L0 norm measures	9
Figure 2 Lp norm measure, $p = 0.5$	10
Figure 3 L_1 norm measure.....	10
Figure 4 Log measure.	11
Figure 5 Tanh measure of sparseness.	11
Figure 6 Kurtosis measure of sparseness.	12
Figure 7 Gini Index measure of sparseness.	12
Figure 8 Block signal reconstruction, signal length 4096, number of samples 400.	19
Figure 9 Heavisine signal reconstruction, signal length 4096, number of samples 400...	19
Figure 10 CS Signal reconstruction in a Noisy Channel.	20
Figure 11 CS Signal reconstruction in a Noiseless Channel with original noisy signal...	20
Figure 12 Blocks Sparsity – l_0 Pseudo-Norm (noisy).	21
Figure 13 Blocks Sparsity – l_1 Norm (noisy).	21
Figure 14 Blocks Sparsity – Log Measure (noisy).	22
Figure 15 Blocks Sparsity – Tanh Measure (noisy).	22
Figure 16 Blocks Sparsity – Gini Index Measure.	23
Figure 17 Noisy Block signal reconstruction, signal length 4096, samples size 400.	23
Figure 18 Heavisine Signal-mean square error vs SNR using OMP.	24
Figure 19 Bumps Signal-mean square error vs SNR using OMP.....	25
Figure 20 Blocks Signal mean square error vs SNR using OMP.	25
Figure 21 Doppler Signal-mean square error vs SNR using OMP.....	26
Figure 22 Ramp Signal mean square error vs SNR using OMP.....	26
Figure 23 Nyquist Folding A-to-I Receiver Architecture.....	28
Figure 24 Flow Chart for the detection algorithm	31
Figure 25 Spectrogram of data (Noiseless).....	32
Figure 26 Spectrogram of data (Gaussian and Rice channel).....	32
Figure 27 PSD of a wideband spectrum	34
Figure 28 Noiseless Signal frequency response at a compression ratio of 70%	34
Figure 29a Noisy Signal (10 dB) frequency response at a compression ratio of 70%	35
Figure 29b Noisy signal (10 dB) frequency response at a compression ratio of 80%	35
Figure 29c Noisy signal (10 dB) frequency response at a compression ratio of 20%	36
Figure 30a RMS error using BP algorithm and different no. of samples for AWGN channel at 1 iteration	36
Figure 30b RMS error using BP algorithm and different no. of samples for AWGN channel at 200 iterations	37
Figure 30c RMS error using BP algorithm and different lower no. of samples for AWGN channel at 5 iterations	37
Figure 30d RMS error using BP algorithm and different lower no. of samples for AWGN channel at 200 iterations	38
Figure 31 CS Based Spectrum Detection in an AWGN and Fading Channel	39
Figure 32 Noisy PSD (Rayleigh) at a Compression Ratio of 60%.	41
Figure 33 Noisy PSD (Rayleigh) at a Compression Ratio of 80%.	41
Figure 34 RMS Error Using CS Algorithms of Noisy PSD (10 dB) at 70% Sampling Measurement.....	42

Figure 35 RMS Error Using BP Algorithm at Different Number of Samples for Noisy Channel	43
Figure 36 RMS Error Using LASSO Algorithm at Different Number of Samples for Noisy Channel.....	43
Figure 37 RMS Error Using OMP Algorithm at Different Number of Samples for Noisy Channel	44
Figure 38 Noisy PSD (Rice fading + Gaussian) at a Compression Ratio of 70%.....	45
Figure 39 Noisy PSD (Rayleigh Fading Channel + Gaussian) Frequency Responses at a Compression Ratio of 60%.....	46
Figure 40 RMS Error Using CS Algorithms of Noisy (Rice Fading+AWGN) PSD (10 dB) at 70% Sampling Measurement	46
Figure 41 RMS Error Using CS Algorithms of Noisy (Rice fading+AWGN) PSD (10 dB) at 60% Sampling Measurement	47
Figure 42 RMS Error Using BP algorithm at Different Number of Samples for Rice Fading plus AWGN Noise.....	47
Figure 43 RMS Error Using BP Algorithm at Different Sample Number for Rice Fading plus AWGN Noise	48
Figure 44 RMS Error Using OMP Algorithm at Different Number of Samples for Rice Fading plus AWGN Noise.....	48
Figure 45 RMS Error Using OMP Algorithm at Different Sample Number for Rice Fading plus AWGN Noise	49
Figure 46 RMS Error Using LASSO Algorithm at Different Number of Samples for Rice fading plus AWGN Noise.....	49
Figure 47 RMS Error Using LASSO Algorithm at Different Sample Number for Rice fading plus AWGN Noise.....	50
Figure 48 Frequency Reponses PSD Passed Through Fading Channel at 150 Max. Doppler Shift	51
Figure 49 Root Mean Square Error of CS Algorithms in (fading plus AWGN) Environment at 150 Max. Doppler Shift.....	52
Figure 50 Frequency Response of PSD Passed through Fading Channel at 100 Max. Doppler Shift	52
Figure 51 Root Mean Square Error of CS Algorithms in (fading plus AWGN) Environment at 100 Max. Doppler Shift.....	53
Figure 52 Frequency Response of PSD Passed through Fading Channel at 10 Max. Doppler Shift	53
Figure 53 Root Mean Square Error of CS Algorithms in (Fading plus AWGN) Environment at 10 Max. Doppler Shift.....	54
Figure 54: Link-adaptive cooperative diversity system model.....	57
Figure 55 Ergodic capacities of ORA, OPRA and TCIFR policies in an i.n.d Rayleigh channel (N = 2).	66
Figure 56 Ergodic capacity of TCIFR versus cut-off SNR (γ_0) in an i.n.d Rayleigh channel (N=2).....	67
Figure 57 Ergodic capacities of ORA, OPRA and TCIFR policies in an i.i.d Nakagami channel (N = 1).	68
Figure 58 Ergodic capacity of N relays with ORA policy as a function of fixed transmit power assignment $\delta_{s,i}$ in a Nakagami-m channel.....	69

Figure 59a: Ergodic capacity of N relays with ORA policy in a Nakagami-m channel...	69
Figure 59b: Different transmit power assignment, $\delta_{s,i}$ of N relays with ORA policy ($c = 10^{-1}$)	70
Figure 59c: Ergodic capacity of N relays with ORA policy in a Nakagami-m ($m=1.5$) fading channel.....	70
Figure 60 Ergodic capacities in an i.n.d Nakagami-m fading channel with N relays	72
Figure 61a Outage probability (“Upper Bound Case”) of source adaptive policies in an i.n.d Nakagami-m fading channel with N relays.	73
Figure 61b Cut-off SNR (γ_0) versus SNR E_s/N_0 in an i.n.d Nakagami-m fading channel	74
Figure 62 Outage probability of i.n.d. Nakagami-m fading channels for 2 relay diversity.	75
Figure 63 Outage probability of i.i.d. Nakagami-m fading channels for 2 relay diversity.	75
Figure 64 Average BER for i.n.d. Nakagami-m fading channel for 2 relay diversity.....	76
Figure 65 Average BER for i.n.d. Rayleigh fading channel for 2 relay diversity	77
Figure 66 Achievable rates for i.n.d. Nakagami-m fading channels for 2 relay diversity	78
Figure 67 Achievable rates for i.n.d. Rayleigh fading channels for 2 relay diversity	78

LIST OF TABLES

Table 1 Sparseness Measures.....	7
Table 2 Sparseness Measure of Various 1-D signals (signal length=128).....	13
Table 3 Sparseness Measure of Various 1-D signals (signal length=256).....	14
Table 4 Sparseness Measure of Various 1-D signals (signal length=512).....	15
Table 5 Sparseness Measure of Various 1-D signals (signal length=1024).....	16
Table 6 Sparseness Measure of 1-D Signals (signal length=2048, sample=256).....	17
Table 7 Sparseness Measure of 1-D Signals (signal length=4096, sample=512).....	18
Table 8 Percentage Error Analysis.....	33

1. INTRODUCTION AND SUMMARY

1.1 Introduction

The theory of Compressive Sampling has the potential of achieving a reduction in the communication and computation costs at the sensor. A discussion of the theory of compressive sensing is in section 2.1, while in section 2.2 we discussed about the research work carried out to determine whether it is possible to predict the best basis for effective reconstruction of different types of signals using compressive sensing algorithms. The performance of the Nyquist Folding analog-to-information receiver (NYFR), a compressive sampling based application for signal detection, for wideband signal detection in multipath fading environment is discussed in section 2.3, while another compressive sensing based method for spectrum sensing, which makes use of signal reconstruction is discussed in section 2.4.

In section 3, upper bounds on the link spectral efficiency of amplify-and-forward cooperative diversity networks with independent but non-identically distributed wireless fading statistics are studied by deriving the ergodic capacity of three distinct adaptive source transmission techniques: (i) constant power with optimal rate adaptation (ORA); (ii) optimal joint power and rate adaptation (OPRA); and (iii) fixed rate with truncated channel inversion (TCIFR). Asymptotic capacity bound is also derived which shows that optimal rate adaptation with constant power policy provides roughly the same ergodic capacity as the optimal joint power and rate adaptation policy at high mean signal-to-noise ratios (SNRs). Different from previous related studies, we advocate a simple numerical procedure for unified analysis of ergodic channel capacity in a myriad of fading environments. This framework allows us to gain insights as to how fade distributions and dissimilar fading statistics across the diversity paths affect the maximum transmission rates, without imposing any restrictions on the fading parameters. Analytical expressions are also derived for the achievable spectral efficiency and average bit error rate for M-QAM transmission with amplify-and-forward cooperative diversity network in a Nakagami-m fading environment. The analysis is based on upper bound, lower bound and tight approximation.

2. COMPRESSIVE SENSING APPLICATION IN SPECTRUM ACCESS

2.1 Methods Assumptions and Procedures for Compressive Sensing Applications

One of the recent research areas in the area of signal processing is Compressive Sampling or Compressed Sensing as it may be referred to by other. This theory tends to enable a reduction in the communication and computation costs at the sensor. According to Candes, Tao and Romberg [1], a small number of random projections of a signal that is compressible is all the information required in order to effectively and adequately reconstructs the signal. In other words, the computational burden is shifted to the receiver side of the communication system and will also result in efficient usage of the transmission or communication bandwidth.

Signal compression, in the traditional sense of it, heuristically we know of bases or frame that can be used to model a particular type of signal. In this sense, compression for a lot of signals is possible; simply by specifying the largest coefficients in the transform domain and using this set of coefficients, a good reconstruction is achievable. Compressed sensing on the other hand, illustrates that an N -sample signal that is K -sparse requires just a number of projections of the order $O(K \log(N))$ along random directions in order to reconstruct the signal in good quality with high probability. By K -sparse we meant that the sparse representation of the signal has K non-zero elements. In compressive sampling theory, the largest coefficients are not measured directly. Instead, the projections of the signal onto a second set of basis functions are measured. These are referred to as the measurement basis. The two bases, sparsifying basis and the measurement basis are required to be incoherent. One of the fundamental theorems of compressive sampling is stated below [1]:

Theorem 1: Assume that a signal x is K -sparse and that we are given P Fourier coefficients with frequencies selected uniformly at random. Suppose that the number of observations obeys

$$P \geq C \cdot K \cdot \log N. \quad (1)$$

Then minimizing l_1 reconstructs x exactly with overwhelming probability. In details, if the constant C is of the form $22(\delta + 1)$ in Equation (1), then the probability of success exceeds

$$1 - O(N^{-\delta}).$$

Considering the above stated theorem, we can conclude that it is possible to reconstruct signal x without suffering any information loss, just by taking any set of P frequency coefficients. Also we can recover signal x by minimizing a convex functional which does not assume any knowledge about the number of nonzero coordinates of x , their locations, and their amplitudes which we assume are all completely unknown a priori. According to Candes [5], P is in general the optimal number of coefficients required. There are situations whereby the minimum number of samples required for exact reconstruction regardless of the method must be about $K \log N$.

2.1.1 Reconstruction (Sparsifying) Bases

Transform bases can be used to make the signal sparse. As mentioned earlier, the reconstruction bases that are considered for this work includes Fast Fourier Transform

(FFT), Discrete Cosine Transform (DCT) and Discrete Wavelet Transform (DWT) with Haar, Daubechies 4, Coiflet and Symlet filters.

Fast Fourier Transform

The Fourier transform is widely used over linear time-invariant signal processing because sinusoidal waves $e^{i\omega t}$ are eigenvectors of linear time-invariant operators. It involves the transformation of signal waveforms into an infinite summation (the integral) of sinusoids with the frequency differences between adjacent sinusoids infinitesimally small. Fourier Transform can be expressed as [6]

$$S(f) = \int_{-\infty}^{\infty} s(t)e^{-i2\pi ft} dt \quad (2)$$

where $S(f)$ is the Fourier transform of the signal $s(t)$, f is the frequency and t is time. The Fourier transform provides simple answers to most questions. For a signal $s(t)$ of N points, a direct calculation of the N discrete Fourier sums is defined by;

$$\hat{S}[k] = \sum_{n=0}^{N-1} s[n] \exp\left(\frac{-i2\pi kn}{N}\right), \text{ for } 0 \leq k < N, \quad (3)$$

The Fast Fourier Transform (FFT) algorithm reduces the numerical complexity to $O(N \log_2 N)$ by reorganizing the calculations. Fast Fourier Transform (FFT) has been used extensively for signal analysis in the past and is still being used. Frequency resolution, phase measurements and error calculations are some of the application areas of FFT. It has the ability to localize signals in the frequency domain.

Discrete Cosine Transform

Discrete Cosine Transforms (DCT) has been applied in the past in the area of data compressions, feature extraction, multiframe detection, etc. Basis vectors in the DCT domain have been proved to provide good energy compaction for natural images. Given an N -dimensional vector input x , the N point DCT Y , is defined as

$$Y = D_N \cdot x \quad (4)$$

where D_N is the DCT transformation matrix of size N by N , with elements $D_N(i,j)$ defined as;

$$D_N(i, j) = c_i \sqrt{\frac{2}{N}} \cos \frac{(2j+1)i\pi}{2N} \quad (5)$$

where

$$c_i = \begin{cases} 1/\sqrt{2} & i = 0 \\ 1 & i > 0 \end{cases} \quad (6)$$

The DCT is orthogonal, hence the inverse transformation can be written as

$$x = D_N^T \cdot Y \quad (7)$$

Wavelet Transform

Wavelet transform has the capability of localizing signals in both time and frequency domains. As a result of this special characteristic, it has found usage in various applications such as image processing, biomedical image system, electromagnetic

systems, data compression, signal detection [7, 8], and so on. By definition, a wavelet ψ is a function of zero average [6]:

$$\int_{-\infty}^{\infty} \psi(t) dt = 0 \quad (8)$$

which is dilated with a scale parameter s , and translated by u :

$$\psi_{u,s}(t) = \frac{1}{\sqrt{s}} \psi\left(\frac{t-u}{s}\right) \quad (9)$$

where $\psi(t)$ is the mother wavelet equation, u is the translation parameter and s is the dilation factor also referred to as the scale. The wavelet transform of a function or signal f , at the scale s and position u is computed by correlating f with a wavelet atom as shown in equation 9.

$$Wf(u, s) = \int_{-\infty}^{\infty} f(t) \frac{1}{\sqrt{s}} \psi^*\left(\frac{t-u}{s}\right) dt \quad (10)$$

where $Wf(u, s)$ is the wavelet transform, $f(t)$ is the original signal [6]. The integral function represents the Continuous Wavelet Transform (CWT).

2.1.2 Measurement (Sampling) Bases

One of the goals of compressive sampling signal reconstruction is to be able to design a matrix Φ , which satisfies the requirement of orthogonality for any subset of columns of size K . Though it might be difficult to prove that there exists a matrix that will obey UUP for large values of K , we know that trivial randomized construction will do so with good probability. Examples of such random matrices that are capable of achieving results are discussed below:

- a) Gaussian measurements: The sensing matrix Φ is obtained by taking independent samples from the normal distribution with zero mean and a variance of value $1/P$. Then if

$$K \leq C \cdot P / \log(N/P) \quad (11)$$

[9], [10].

- b) Binary measurements: In this case, the sensing matrix Φ is obtained by taking independent samples from the symmetric Bernoulli distribution with parameter;

$$\text{Prob}(\Phi_{si} = \pm 1/\sqrt{P}) = 1/2 \quad (12)$$

- c) Fourier measurements: Let us assume that the sensing matrix Φ is a partial Fourier matrix obtained by taking P rows uniformly at random, but renormalizing the columns such that they are unit-normed. Candes and Tao [11] have shown that CS theorem holds with overwhelming probability if

$$K \leq C \cdot P / (\log N)^6 \quad (13)$$

This result was recently improved by Rudelson and Vershynin [12] to

$$K \leq C \cdot P / (\log N)^4 \quad (14)$$

- d) Incoherent measurements: Let us assume now that the sensing matrix Φ is obtained by selecting P rows uniformly at random from an N by N orthonormal matrix U and renormalizing the columns so that they are unit-normed. U can be considered as the

matrix $\Phi\Psi^*$ which maps the object from the Ψ to the Φ -domain. The argument used to prove that UUP holds for the Fourier measurements can be extended to this case as well. CS theorem holds with high probability provided that Equation (15) is satisfied.

$$K \leq C \cdot \frac{1}{\mu^2} \cdot \frac{P}{(\log N)^4} \quad (15)$$

where $\mu := \sqrt{N} \max_{i,j} |U_{i,j}|$.

2.1.3 Minimization Algorithms

Minimization algorithm methods for CS come in two different categories namely;

- i. Greedy methods – makes a sequence locally optimal choice in an effort to determine a globally optimal solution. Example includes Matching Pursuit and Orthogonal Matching Pursuit.
- ii. Convex relaxation methods – replaces a combinatorial sparse approximation problem with a related convex program. Example includes Basis Pursuit. The minimization algorithms are discussed below:

Matching Pursuit: If the dictionary is orthonormal, the sparse approximation problem admits a straightforward algorithm. It is possible to build a solution one term at a time by selecting at each step the atom that correlates most strongly with the residual signal. Matching pursuit (MP) extends this idea to other types of dictionary. MP begins by setting the initial residual equal to the input signal and making a trivial initial approximation. That is,

$$r_0 = s \quad \text{and} \quad a_0 = 0.$$

At step k , MP chooses another index λ_k by solving an easy optimization problem

$$\lambda_k \in \arg \max \left| \langle r_{k-1}, \varphi_{\omega} \rangle \right| \quad (16)$$

Then it calculates a new approximation and a new residual

$$a_k = a_{k-1} + \langle r_{k-1}, \varphi_{\lambda_k} \rangle \varphi_{\lambda_k} \quad (17)$$

and

$$r_k = r_{k-1} - \langle r_{k-1}, \varphi_{\lambda_k} \rangle \varphi_{\lambda_k} \quad (18)$$

The residual can also be expressed as

$$r_k = s - a_k \quad (19)$$

When the dictionary is an orthonormal basis, the approximant is always an optimal-term representation of the signal. MP is considered as the pure greedy algorithm [13].

Orthogonal Matching Pursuit: OMP adds a least-squares minimization to each step of MP to obtain the best approximation over the atoms that have already been chosen. This revision significantly improves the behavior of the algorithm. OMP is initialized the same way as MP, and at each step, a new atom is selected according to the same rule as MP, via Equation (17). But the approximants are calculated differently. Let $\Lambda_k = [\lambda_1, \dots, \lambda_k]$ list the atom that has been chosen at step k . Then the k th approximant is

$$\begin{aligned}
a_k &\stackrel{def}{=} \arg \min_a \|s - a\|_2 \\
&\text{subject to } a \in \text{span} \{ \varphi_\lambda : \lambda \in \Lambda_k \}
\end{aligned} \tag{20}$$

This minimization can be performed incrementally with standard least-squares techniques. As before, the residual is calculated as,

$$r_k = s - a_k.$$

Note that OMP never selects the same atom twice because the residual is orthogonal to the atoms that have already been chosen. Consequently, the residual must equal zero after d steps.

Basis Pursuit: Convex relaxation offers another approach to sparse approximation. The fundamental idea is that the number of terms in a representation can be approximated by the absolute sum of the coefficients. This absolute sum is a convex function, and so it can be minimized in polynomial time. Given an input signal s , the BP problem is

$$\min_{\{b_\omega\}} \sum_{\omega \in \Omega} |b_\omega| \tag{21}$$

$$\text{subject to } \sum_{\omega \in \Omega} |b_\omega \varphi_\omega = s| \tag{22}$$

where b_ω is a collection of complex coefficients. One hopes that the nonzero coefficients in the solution of the BP problem will identify the atoms in the optimal representation of the input signal and their coefficients.

Least Absolute Shrinkage and Selection Operator (LASSO)

LASSO (Least Absolute Shrinkage and Selection Operator) is derivatives of LARS (Least Angle Regression) minimum ℓ_1 norm reconstruction algorithm. This greedy algorithm take advantage of geometric correlation between the targeted and the coefficients most correlated with the measured response. LASSO algorithms take advantage of quadratic programming concepts because they produce a weighted minimum ℓ_1 and ℓ_2 norm solution. The LASSO algorithm specifically solves

$$\min \left\{ \frac{1}{2m} \|Y - \dot{S}\|_2^2 + \lambda \|\dot{S}\| \right\} \quad \text{such that } Y = \Phi \dot{S} \tag{23}$$

for any parameter λ . The value of λ typically corresponds to the maximum correlation between the measurements Y and the observation matrix Φ .

Stepwise Orthogonal Matching Pursuit (StOMP)

For n large, Stepwise Orthogonal Matching Pursuit (StOMP) correctly recovers the sparsest solution of $Y = \Phi \chi$ over a region of the sparsity/indeterminacy plane comparable to the region where ℓ_1 minimization is successful. StOMP successively transforms the signal into a negligible residual. Starting with initial residual $r_0 = Y$, at the s -th stage it forms the ‘matched filter’ $\Phi^T r_{s-1}$, identifies all coordinates with amplitudes exceeding a specially-chosen threshold, solves a least-squares problem using the selected coordinates, and subtracts the least squares fit, producing a new residual. After a fixed number of stages it stops. In contrast to Orthogonal Matching Pursuit (OMP), many coefficients can enter the model at each stage in StOMP while only one enters per stage in OMP; and StOMP takes a fixed number of stages, while OMP can take many StOMP runs much

faster than competing proposals for sparse solutions, such as ℓ^1 minimization and OMP, and so is attractive for solving large-scale problems[14].

2.2 Sparseness Measure of Signals for Compressive Sampling

Choice of reconstruction or sparsity basis is one of the major criteria in order to achieve a good CS signal reconstruction. One of the goals of this research work is to be able to show how different choice of sparsity basis affects the quality of the reconstructed signal. One of the objectives of this work is to be able to adequately predict the best basis.

2.2.1 Sparseness Measures

Sparse signal representation helps a great deal in achieving robust methods for compression, detection, denoising, and signal separation [15, 16]. The concept of sparsity has been used to find meaningful data representation in the areas of image analysis, vision research, speech and music analysis [17, 18, 19]. In simple terms, sparsity of a signal can be defined as the number of non-zero elements in a vector representation of the signal. This implies that a signal that is considered sparse has most of its components to be zero. In a practical sense however, sparsity means that most signal components are small enough not to contribute significantly to the information content of the signal.

Some of the sparseness measures found in literature [16][16, 20] are described in Table 1 and discussed below. A common measure is the ℓ^0 pseudo-norm given by the number of non-zero elements as described earlier. The ℓ^0 measure does not take into consideration the magnitude of the non-zero element. Hence replacing a non-zero element with another one, does not affect the sparseness measure. This does not give a true representation of the distribution of the component. In the presence of noise, $\ell^0(\epsilon)$ is used because the noise results in very few of the components being exactly zero.

Table 1 Sparseness Measures.

ℓ^0	$\#\{j, x_j \neq 0\}$
$\ell^0(\epsilon)$	$\#\{j, x_j \geq \epsilon\}$
ℓ^1	$\left(\sum_j x_j \right)$
ℓ^p	$\left(\sum_j x_j ^p\right)^{1/p}, \quad 0 < p < 1$
Log	$\sum_j \log(1 + x_j ^2)$
$\tanh(a,b)$	$\sum_j \tanh(ax_j ^b)$
Kurtosis (k_4)	$\frac{\sum_j x_j ^4}{\left(\sum_j x_j ^2\right)^2}$
Gini Index	Discussed in text

Adding noise to a signal can change the sparseness measure when using l^0 norm measure, hence $l^0(\varepsilon)$ is used instead. The l^p norm is often used instead of $l^0(\varepsilon)$ because it has a useable gradient and thus NP-hard combinatoric optimization problems can be avoided. The $\tanh(a,b)$ measure is sometimes used instead of l^p , $p < 1$ norm because each component contribution is limited to range (0, 1). The concave property of both of them enforces sparsity. The log measure is concave outside some range but convex near the origin. In all of the sparseness measures described in Table 1 with the exception of kurtosis and the Gini index, lower values correspond to more sparsity.

The Gini index is a measure used by economists in evaluating the inequality of wealth distribution. Dalton defines four properties that a sparse measure should satisfy [21] and the Gini index satisfies all conditions [20]. To define the Gini index for a real-valued data set $\{Z\}$, let $x = \{x_1, x_2, \dots, x_N\}$ represent the data elements of $\{Z\}$ ordered in ascending absolute value such that $|x_1| \leq |x_2| \leq |x_3| \leq \dots \leq |x_N|$, and define a piecewise linear function with values between 0 and 1 as

$$L(i) = \frac{\sum_{j=1}^i |x_j|}{\sum_{k=1}^N |x_k|}, \quad \text{for } i = 1, \dots, N \quad (24)$$

where $L(\cdot)$ is denoted as the Lorenz curve. The Lorenz curve equation can be rewritten as,

$$L(i) = \frac{\sum_{j=1}^i |x_j|}{\sum_{k=1}^N |x_k|}, \quad \text{for } i = 1, \dots, N \quad (25)$$

where $\sum_{k=1}^N |x_k|$ is the l^1 norm sparseness measure.

The Lorenz curve can be likened to the cumulative distribution plot of a statistical data; it does give a good representation of how sparsely distributed the data is. The Gini index is twice the area between the Lorenz curve and the 45 degree line. The area underneath the Lorenz curve is

$$A(x) = \frac{1}{2N} \sum_{n=1}^N (L(n-1) + L(n)) \quad (26)$$

Therefore, the Gini index is defined as

$$G(x) = 1 - 2A(x) \quad (27)$$

In economic parlance, the distribution where all individuals have equal wealth is the least sparse, whereas the distribution where one individual controls/possesses all the wealth is the sparsest. In a similar manner, the data distribution whereby all the data have equal value is the least sparse, whereas the one where there is one big value and the rest are zero, is the sparsest.

The value of the Gini index $G(x)$ always lies between 0 and 1, with 1 being the sparsest and 0 representing no sparsity. One of the advantages of this sparseness measure is that normalization is not required when comparing vectors of different lengths; for the other sparseness measures discussed in this section, some form of normalization is required before comparing vectors of different lengths. Also the Gini Index gives an adequate sparseness measurement in the presence of noise unlike the l^0 norm which treats every value other than zero as the same.

2.2.2 Results and Discussion of 1-D Compressive Sampling Signal Reconstruction without Noise

Six different types of signals were simulated, namely Heavisine, Bump, Blocks, Ramp, Doppler and Linear chirp. The bases considered are Fast Fourier Transform (FFT), Discrete Cosine Transform (DCT), and different families of Discrete Wavelet Transform (DWT). We investigated how sparse each of the signals is while represented in the bases being considered using the various sparseness measures listed in Table 1. Thereafter, CS reconstruction was carried out to determine if there is a relationship between the best basis choice of the sparseness measures and the mean square error of the CS reconstruction carried out.

The signals were considered with varying signal lengths of 128, 256, 512, 1024, 2048 and 4096. Figure(s) 1 to 7 show the plot of the sparseness measures for the block signal type, at different original signal lengths. It can be seen from the plots that for the block signal type, all the sparseness measures except kurtosis, predicted that the best sparsifying basis is the haar wavelet.

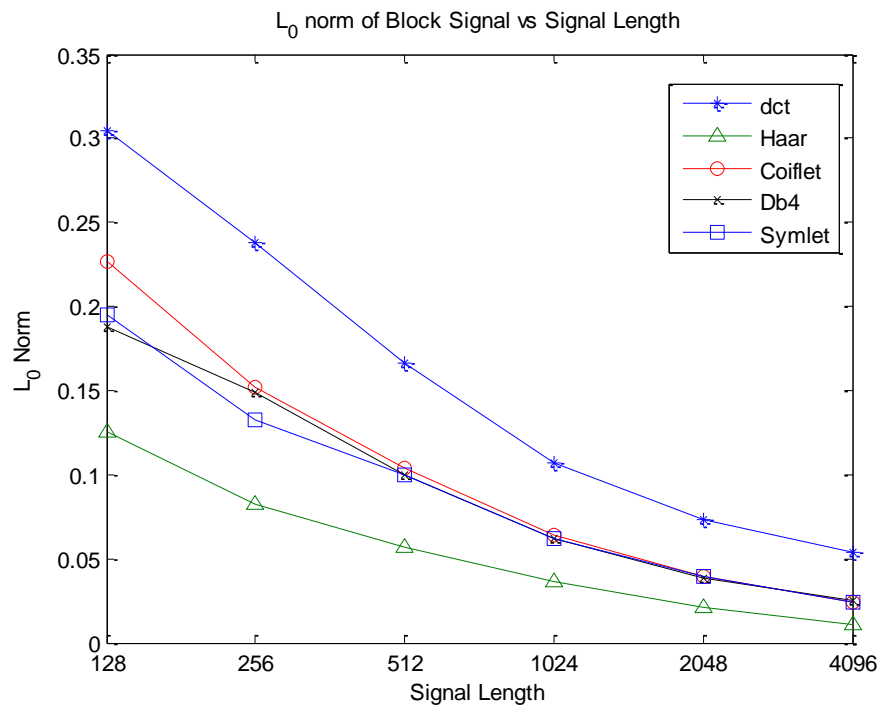


Figure 1 L_0 norm measures.

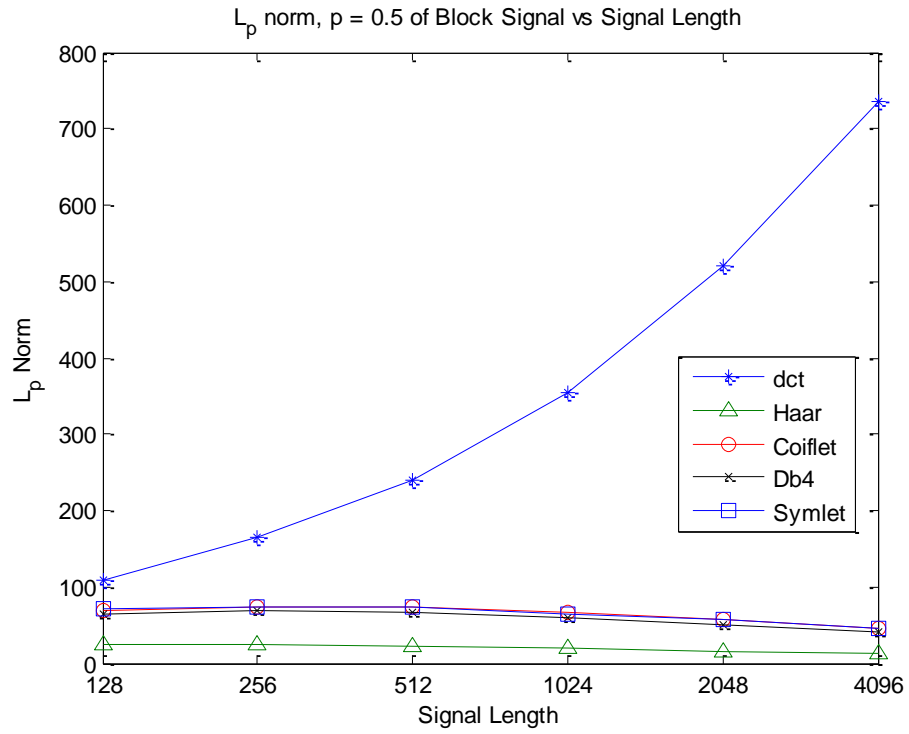


Figure 2 L_p norm measure, $p = 0.5$.

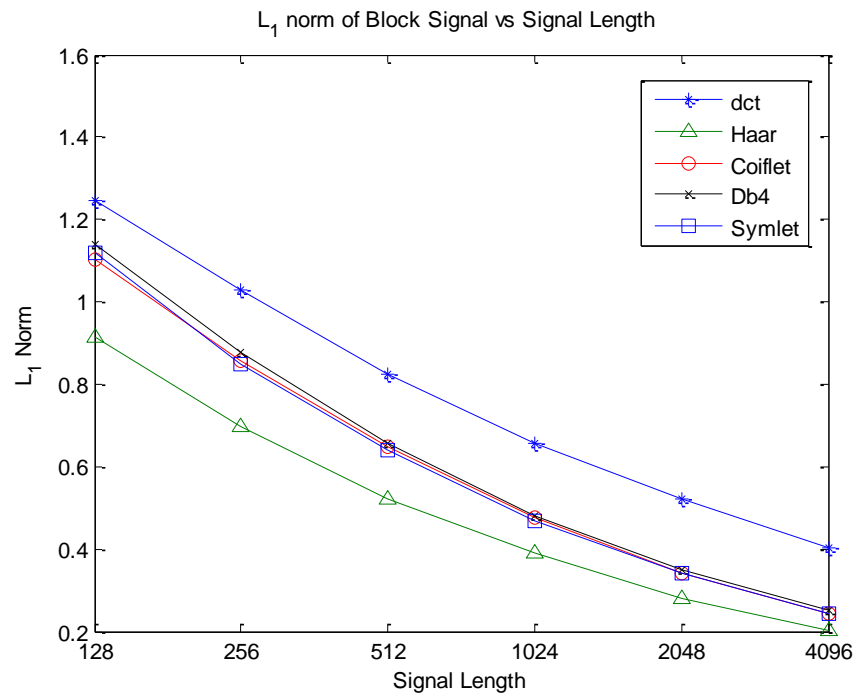


Figure 3 L_1 norm measure.

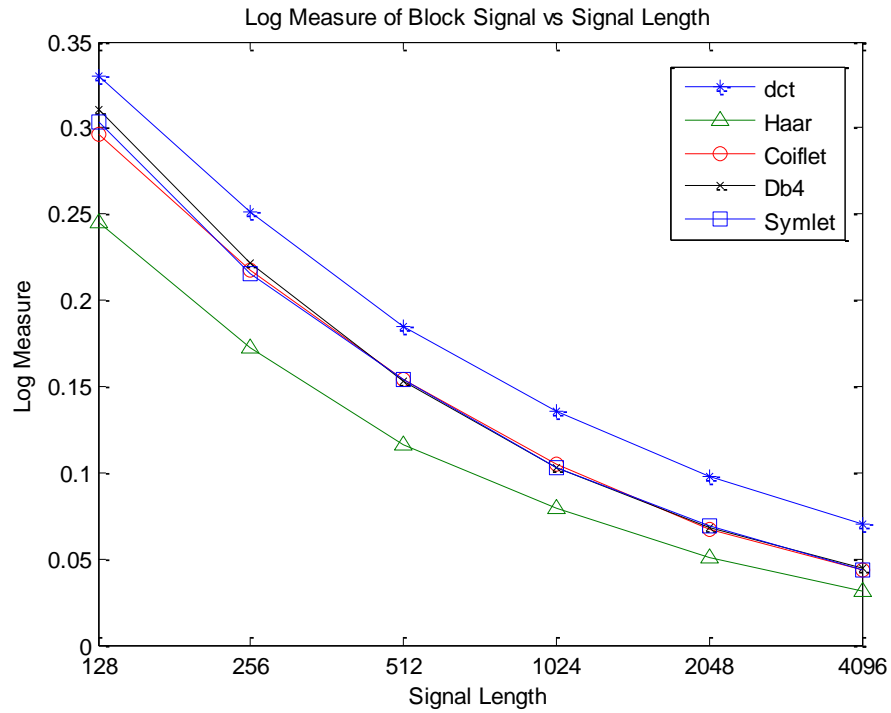


Figure 4 Log measure.

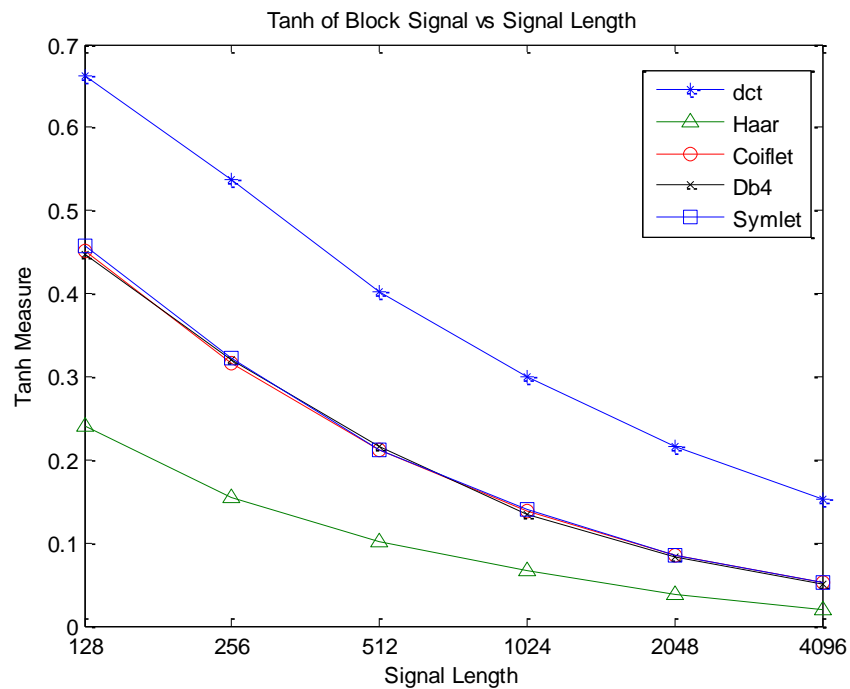


Figure 5 Tanh measure of sparseness.

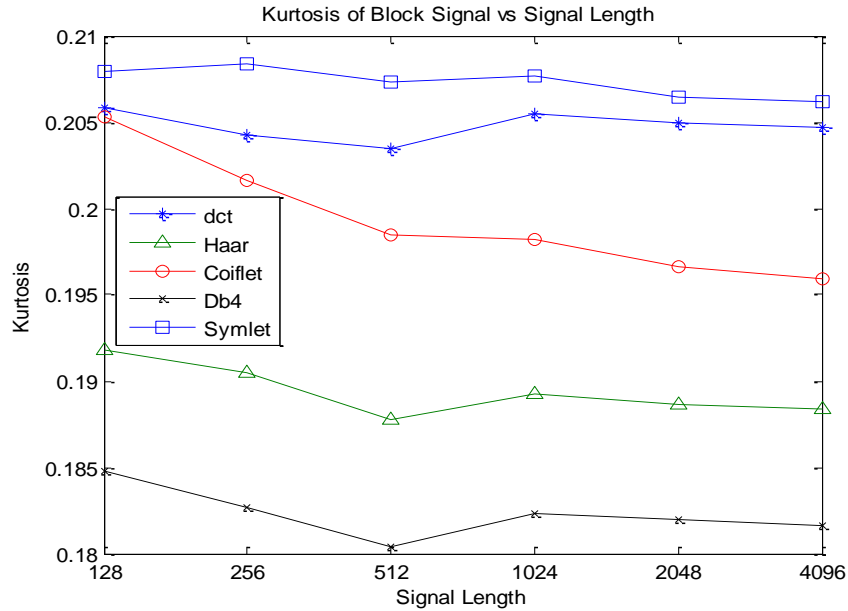


Figure 6 Kurtosis measure of sparseness.

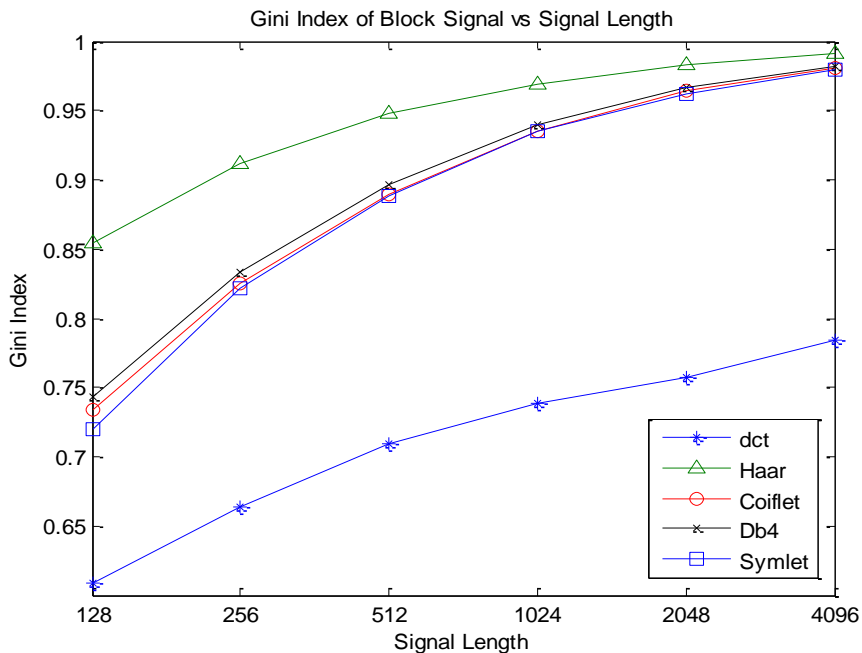


Figure 7 Gini Index measure of sparseness.

Similar data were obtained for the other type of signal that was considered. Tables 2 to 7, contains the data obtained for all the signal type considered. Tables 2 to 5 illustrated the sparsifying basis predicted by each of the sparseness measures for each of the signal type considered at different signal length. However, two particular cases of signal lengths 2048 and 4096 were considered and the results obtained were tabulated in Tables 6 to 7. For these two signal lengths, the sparseness of the signals was measured and the signals were reconstructed using compressive sampling at a decimation ratio of 4:1. The reconstruction was carried out using basis pursuit and orthogonal matching pursuit. Mean

square error of the reconstructed signals in comparison to the original signals were computed and used as performance metric. Apart from Kurtosis which was mostly wrong in its prediction, the other measures performed averagely well with Gini index and l_0 norm having the best prediction across board.

Table 2 Sparseness Measure of Various 1-D signals (signal length = 128).

		FFT	DCT	WAVELET			
				Haar	Coiflet	Db4	Symlet
Heavisine	L ₀	0.6172	0.0547	0.1797	0.0859	0.0859	0.0547
	L _p (p=1)	8.9261	0.8684	1.0995	0.8688	0.9144	0.8630
	L _p (p=0.5)	482.35	43.64	77.712	18.803	22.684	18.402
	Log	0.9157	0.1577	0.2423	0.1625	0.1833	0.1628
	Tanh	0.9157	0.2471	0.4423	0.1633	0.1933	0.1618
	Kurtosis	0.3511	0.2787	0.3812	0.1398	0.1577	0.1539
	Gini Index	0.8017	0.8300	0.7261	0.9176	0.9083	0.9188
Bumps	L ₀	0.7109	0.2500	0.1094	0.1172	0.1328	0.1484
	L _p (p=1)	7.0946	0.5714	0.3607	0.3807	0.4016	0.3901
	L _p (p=0.5)	828.48	61.291	19.042	25.097	26.648	24.484
	Log	1.5714	0.1450	0.1049	0.1010	0.1098	0.1095
	Tanh	0.9848	0.5729	0.2535	0.3012	0.3105	0.2918
	Kurtosis	0.0317	0.0376	0.0704	0.0912	0.0657	0.0708
	Gini Index	0.3142	0.4224	0.7694	0.7098	0.7005	0.7204
Blocks	L ₀	0.7188	0.3047	0.1250	0.2266	0.1875	0.1953
	L _p (p=1)	15.277	1.2464	0.9151	1.1021	1.1401	1.1173
	L _p (p=0.5)	1468.2	108.93	25.253	68.707	65.362	70.559
	Log	1.9230	0.3296	0.2452	0.2959	0.3111	0.3037
	Tanh	0.9910	0.6616	0.2399	0.4515	0.4471	0.4569
	Kurtosis	0.1889	0.2058	0.1918	0.2053	0.1848	0.2080
	Gini Index	0.5465	0.6087	0.8539	0.7337	0.7435	0.7202
	L ₀	0.6172	0.0469	0.0391	0.0469	0.0391	0.0469
	L _p (p=1)	2.2908	0.1806	0.1604	0.1097	0.1274	0.1121
	L _p (p=0.5)	244.01	17.670	13.028	4.1286	6.2330	4.5294
	Log	0.6384	0.0284	0.0275	0.0240	0.0249	0.0234
	Tanh	0.9950	0.1231	0.1285	0.1006	0.1053	0.0973
	Kurtosis	0.0531	0.0822	0.1030	0.1863	0.1538	0.2097
	Gini Index	0.4565	0.5342	0.6535	0.8484	0.7879	0.8331
Doppler	L ₀	0.4531	0.0313	0.0078	0.0156	0.0156	0.0234
	L _p (p=1)	1.7133	0.1445	0.0958	0.0859	0.0841	0.0852
	L _p (p=0.5)	157.4500	12.0380	4.6317	1.6738	1.4626	1.5895
	Log	0.4041	0.0264	0.0228	0.0225	0.0220	0.0224
	Tanh	0.9316	0.0858	0.0633	0.0638	0.0692	0.0646
	Kurtosis	0.1668	0.1527	0.2350	0.2411	0.2774	0.2613
	Gini Index	0.5686	0.6417	0.8413	0.9223	0.9254	0.9235
Ramp	L ₀	0.7344	0.3203	0.2578	0.1875	0.2578	0.1797
	L _p (p=1)	7.7159	0.6115	0.5353	0.4285	0.4526	0.4519
	L _p (p=0.5)	985.50	71.0530	55.8450	32.5980	37.6560	36.9180
	Log	1.7783	0.1543	0.1376	0.1198	0.1225	0.1242
	Tanh	1.0000	0.7077	0.5533	0.3631	0.4204	0.3977
	Kurtosis	0.0080	0.0122	0.0224	0.0330	0.0345	0.0301
	Gini Index	0.0309	0.2872	0.4434	0.6389	0.5938	0.6012
Linear Chirp	L ₀	0.7344	0.3203	0.2578	0.1875	0.2578	0.1797
	L _p (p=1)	7.7159	0.6115	0.5353	0.4285	0.4526	0.4519
	L _p (p=0.5)	985.50	71.0530	55.8450	32.5980	37.6560	36.9180
	Log	1.7783	0.1543	0.1376	0.1198	0.1225	0.1242
	Tanh	1.0000	0.7077	0.5533	0.3631	0.4204	0.3977
	Kurtosis	0.0080	0.0122	0.0224	0.0330	0.0345	0.0301
	Gini Index	0.0309	0.2872	0.4434	0.6389	0.5938	0.6012

Table 3 Sparseness Measure of Various 1-D signals (signal length = 256).

		FFT	DCT	WAVELET			
				Haar	Coiflet	Db4	Symlet
Heavisine	L ₀	0.6016	0.0313	0.1016	0.0391	0.0547	0.0430
	L _p (p=1)	9.4953	0.6508	0.8223	0.5928	0.6583	0.6173
	L _p (p=0.5)	923.39	56.318	93.769	14.007	18.821	14.920
	Log	0.8948	0.1047	0.1651	0.0950	0.1149	0.0991
	Tanh	0.9202	0.1593	0.2706	0.0954	0.1217	0.1026
	Kurtosis	0.3515	0.2779	0.3796	0.1716	0.1585	0.1442
	Gini Index	0.8212	0.8575	0.8001	0.9594	0.9496	0.9564
Bumps	L ₀	0.7188	0.1797	0.0938	0.1016	0.1133	0.0898
	L _p (p=1)	8.2609	0.4740	0.2979	0.3079	0.3099	0.3158
	L _p (p=0.5)	1815.60	96.201	27.146	30.532	29.971	31.632
	Log	1.5997	0.1136	0.0844	0.0845	0.0866	0.0879
	Tanh	1.0000	0.4359	0.2173	0.2271	0.2193	0.2288
	Kurtosis	0.0342	0.0399	0.0562	0.0581	0.0556	0.0557
	Gini Index	0.4213	0.4947	0.8113	0.7901	0.7931	0.7844
Blocks	L ₀	0.7109	0.2383	0.0820	0.1523	0.1484	0.1328
	L _p (p=1)	17.7490	1.0280	0.6957	0.8575	0.8791	0.8498
	L _p (p=0.5)	3129.60	164.95	23.732	74.103	69.725	73.673
	Log	1.9342	0.2512	0.1720	0.2178	0.2216	0.2152
	Tanh	0.9996	0.5365	0.1539	0.3156	0.3199	0.3220
	Kurtosis	0.1878	0.2043	0.1905	0.2016	0.1827	0.2084
	Gini Index	0.6098	0.6639	0.9120	0.8254	0.8332	0.8219
Doppler	L ₀	0.5469	0.0273	0.0313	0.0313	0.0234	0.0195
	L _p (p=1)	2.5805	0.1438	0.1278	0.0837	0.0940	0.0807
	L _p (p=0.5)	488.93	24.958	18.197	4.2194	5.9734	3.9437
	Log	0.6222	0.0240	0.0230	0.0200	0.0204	0.0193
	Tanh	0.9705	0.0859	0.0862	0.0624	0.0757	0.0635
	Kurtosis	0.0533	0.0850	0.1054	0.1409	0.1545	0.1711
	Gini Index	0.5634	0.6207	0.7230	0.9041	0.8741	0.9090
Ramp	L ₀	0.4219	0.0195	0.0156	0.0195	0.0078	0.0195
	L _p (p=1)	1.9359	0.1147	0.0692	0.0620	0.0603	0.0627
	L _p (p=0.5)	326.96	17.403	4.9767	1.3670	1.1357	1.3434
	Log	0.4111	0.0210	0.0174	0.0168	0.0168	0.0173
	Tanh	0.9316	0.0564	0.0400	0.0436	0.0401	0.0429
	Kurtosis	0.1667	0.1527	0.2343	0.2401	0.2770	0.2642
	Gini Index	0.6174	0.6839	0.8924	0.9571	0.9608	0.9572
Linear Chirp	L ₀	0.7383	0.3242	0.2266	0.1836	0.2305	0.1953
	L _p (p=1)	11.0300	0.6189	0.5344	0.4286	0.4387	0.4386
	L _p (p=0.5)	2819.10	144.25	110.1900	63.3050	70.4190	66.3740
	Log	2.0859	0.1570	0.1380	0.1194	0.1183	0.1224
	Tanh	1.0000	0.7140	0.5357	0.3739	0.3953	0.3872
	Kurtosis	0.0040	0.0060	0.0116	0.0189	0.0267	0.0179
	Gini Index	0.0241	0.2832	0.4550	0.6438	0.6121	0.6290

Table 4 Sparseness Measure of Various 1-D signals (signal length = 512).

		FFT	DCT	WAVELET			
				Haar	Coiflet	Db4	Symlet
Heavisine	L ₀	0.5918	0.0273	0.0664	0.0254	0.0293	0.0215
	L _p (p=1)	10.0470	0.4836	0.6087	0.4103	0.4684	0.4346
	L _p (p=0.5)	1793.1	74.011	110.16	10.811	14.619	11.437
	Log	0.8837	0.0686	0.1125	0.0575	0.0708	0.0601
	Tanh	0.9192	0.1027	0.1769	0.0587	0.0712	0.0598
	Kurtosis	0.3520	0.2769	0.3775	0.1871	0.1584	0.1529
	Gini Index	0.8348	0.8734	0.8545	0.9786	0.9736	0.9775
Bumps	L ₀	0.7090	0.1152	0.0762	0.0703	0.0820	0.0723
	L _p (p=1)	10.1470	0.4090	0.2651	0.2593	0.2643	0.2603
	L _p (p=0.5)	3996.4	147.35	39.5760	35.775	36.647	36.486
	Log	1.6058	0.0983	0.0763	0.0734	0.0752	0.0730
	Tanh	0.9970	0.3198	0.1675	0.1683	0.1718	0.1717
	Kurtosis	0.0330	0.0389	0.0459	0.0503	0.0480	0.0510
	Gini Index	0.5356	0.5950	0.8543	0.8574	0.8547	0.8542
Blocks	L ₀	0.7168	0.1660	0.0566	0.1035	0.0996	0.0996
	L _p (p=1)	20.2330	0.8229	0.5204	0.6463	0.6579	0.6413
	L _p (p=0.5)	6553.0	239.22	21.882	74.505	67.6290	73.1190
	Log	1.9430	0.1846	0.1160	0.1543	0.1535	0.1537
	Tanh	0.9997	0.4022	0.1015	0.2121	0.2163	0.2119
	Kurtosis	0.1861	0.2035	0.1878	0.1985	0.1804	0.2073
	Gini Index	0.6570	0.7098	0.9485	0.8890	0.8967	0.8880
Doppler	L ₀	0.4941	0.0215	0.0215	0.0176	0.0215	0.0156
	L _p (p=1)	2.8054	0.1109	0.1002	0.0623	0.0687	0.0604
	L _p (p=0.5)	895.96	32.532	24.326	3.7409	5.4810	3.6227
	Log	0.5707	0.0196	0.0187	0.0160	0.0163	0.0155
	Tanh	0.8450	0.0622	0.0612	0.0408	0.0543	0.0409
	Kurtosis	0.0537	0.0843	0.1061	0.1189	0.1552	0.1450
	Gini Index	0.6735	0.7105	0.7819	0.9456	0.9278	0.9469
Ramp	L ₀	0.4434	0.0117	0.0078	0.0078	0.0078	0.0137
	L _p (p=1)	2.1556	0.0900	0.0503	0.0455	0.0435	0.0462
	L _p (p=0.5)	670.98	25.06	5.4547	1.1547	0.9322	1.1349
	Log	0.4145	0.0160	0.0124	0.0125	0.0123	0.0130
	Tanh	0.9316	0.0374	0.0260	0.0264	0.0238	0.0276
	Kurtosis	0.1667	0.1507	0.2472	0.2362	0.2770	0.2623
	Gini Index	0.6560	0.7155	0.9247	0.9760	0.9787	0.9758
Linear Chirp	L ₀	0.7383	0.3203	0.2266	0.1719	0.2070	0.1758
	L _p (p=1)	15.7160	0.6239	0.5294	0.4232	0.4441	0.4338
	L _p (p=0.5)	8037.3	291.04	215.33	119.29	137.51	126.72
	Log	2.3924	0.1589	0.1371	0.1193	0.1226	0.1216
	Tanh	1.0000	0.7189	0.5252	0.3617	0.3985	0.3796
	Kurtosis	0.0020	0.0030	0.0068	0.0111	0.0103	0.0103
	Gini Index	0.0182	0.2808	0.4669	0.6558	0.6195	0.6393

Table 5 Sparseness Measure of Various 1-D signals (signal length = 1024).

		FFT	DCT	WAVELET			
				Haar	Coiflet	Db4	Symlet
Heavisine	L ₀	0.5918	0.0176	0.0449	0.0146	0.0186	0.0156
	L _p (p=1)	10.6070	0.3577	0.4440	0.2852	0.3325	0.3063
	L _p (p=0.5)	3506.9000	98.7320	124.6000	8.0445	11.0660	8.7073
	Log	0.8779	0.0448	0.0752	0.0343	0.0434	0.0365
	Tanh	0.9173	0.0689	0.1122	0.0360	0.0414	0.0358
	Kurtosis	0.3519	0.2759	0.3764	0.1921	0.1582	0.1592
	Gini Index	0.8453	0.8839	0.8956	0.9890	0.9863	0.9884
Bumps	L ₀	0.6650	0.0752	0.0469	0.0361	0.0557	0.0508
	L _p (p=1)	11.2080	0.3167	0.2098	0.1926	0.1958	0.1936
	L _p (p=0.5)	7381.3	189.07	49.617	33.173	33.605	32.931
	Log	1.4435	0.0761	0.0583	0.0537	0.0552	0.0542
	Tanh	0.9815	0.2041	0.1130	0.1064	0.1109	0.1089
	Kurtosis	0.0327	0.0390	0.0440	0.0512	0.0472	0.0500
	Gini Index	0.6603	0.7041	0.8971	0.9158	0.9160	0.9160
Blocks	L ₀	0.7197	0.1065	0.0361	0.0645	0.0615	0.0615
	L _p (p=1)	22.7540	0.6584	0.3909	0.4747	0.4812	0.4694
	L _p (p=0.5)	13561.	353.67	20.58	67.345	59.926	65.456
	Log	1.9510	0.1358	0.0798	0.1045	0.1030	0.1032
	Tanh	0.9994	0.3007	0.0662	0.1386	0.1347	0.1394
	Kurtosis	0.1880	0.2055	0.1893	0.1982	0.1824	0.2077
	Gini Index	0.6935	0.7385	0.9687	0.9345	0.9403	0.9346
Doppler	L ₀	0.3604	0.0146	0.0166	0.0107	0.0166	0.0098
	L _p (p=1)	2.9376	0.0819	0.0767	0.0445	0.0498	0.0438
	L _p (p=0.5)	1405.8	34.259	30.87	2.9673	4.8014	3.0399
	Log	0.4948	0.0155	0.0147	0.0121	0.0125	0.0117
	Tanh	0.6310	0.0449	0.0441	0.0247	0.0351	0.0246
	Kurtosis	0.0537	0.0841	0.1063	0.1080	0.1551	0.1305
	Gini Index	0.7862	0.8140	0.8324	0.9717	0.9593	0.9710
Ramp	L ₀	0.4365	0.0088	0.0039	0.0078	0.0039	0.0068
	L _p (p=1)	2.3767	0.0698	0.0359	0.0337	0.0311	0.0344
	L _p (p=0.5)	1366.5	35.802	5.6859	0.9825	0.7052	0.9895
	Log	0.4163	0.0119	0.0087	0.0091	0.0086	0.0095
	Tanh	0.9316	0.0262	0.0153	0.0175	0.0144	0.0179
	Kurtosis	0.1667	0.1507	0.2470	0.2336	0.2769	0.2598
	Gini Index	0.6878	0.7420	0.9483	0.9862	0.9889	0.9859
Linear Chirp	L ₀	0.7432	0.3330	0.2178	0.1748	0.1982	0.1719
	L _p (p=1)	22.3430	0.6276	0.5285	0.4239	0.4396	0.4285
	L _p (p=0.5)	22861.0	586.11	426.32	235.48	268.07	241.42
	Log	2.6977	0.1602	0.1373	0.1196	0.1210	0.1208
	Tanh	1.0000	0.7224	0.5171	0.3687	0.3939	0.3730
	Kurtosis	0.0010	0.0015	0.0035	0.0056	0.0074	0.0055
	Gini Index	0.0135	0.2787	0.4732	0.6576	0.6243	0.6504

Table 6 Sparseness Measures of 1-D Signals (Signal length =2048, sample=256).

		FFT	DCT	WAVELET			
				Haar	Coiflet	Db4	Symlet
Heavisine	L ₀	0.5889	0.0137	0.0278	0.0088	0.0107	0.0107
	L _p (p=1)	11.1700	0.2643	0.3195	0.2005	0.2359	0.2167
	L _n (p=0.5)	6903.00	133.98	135.82	6.0631	8.2454	6.5401
	Log	0.8748	0.0296	0.0493	0.0209	0.0265	0.0223
	tanh (a=2, b=3)	0.9170	0.0477	0.0697	0.0218	0.0242	0.0215
	Kurtosis	0.3520	0.2757	0.3761	0.1936	0.1583	0.1626
	Gini Index	0.8540	0.8913	0.9261	0.9942	0.9930	0.9940
	MSE-BP	9.5246	0.04213	0.22923	0.005685	0.0071205	0.0050828
	MSE-OMP	0.013563	0.083194	0.24258	8.73E-07	2.61E-06	1.78E-07
Bumps	L ₀	0.6226	0.0479	0.0342	0.0239	0.0322	0.0337
	L _p (p=1)	11.9480	0.2382	0.1634	0.1363	0.1430	0.1364
	L _n (p=0.5)	12410.0	224.95	61.465	26.204	28.434	26.146
	Log	1.2137	0.0570	0.0426	0.0367	0.0391	0.0366
	tanh (a=2, b=3)	0.9479	0.1321	0.0790	0.0633	0.0684	0.0638
	Kurtosis	0.0325	0.0388	0.0431	0.0537	0.0468	0.0524
	Gini Index	0.7648	0.7927	0.9259	0.9554	0.9538	0.9555
	MSE-BP	0.5198	0.3227	0.2442	0.1867	0.1686	0.1842
	MSE-OMP	0.1329	0.5740	0.3862	0.3495	0.4997	0.2243
Blocks	L ₀	0.7256	0.0728	0.0210	0.0391	0.0386	0.0391
	L _p (p=1)	25.1980	0.5197	0.2812	0.3401	0.3485	0.3416
	L _n (p=0.5)	27473.0	521.46	16.236	56.216	50.545	56.939
	Log	1.9378	0.0979	0.0503	0.0674	0.0680	0.0690
	tanh (a=2, b=3)	0.9995	0.2155	0.0374	0.0846	0.0823	0.0857
	Kurtosis	0.1875	0.2050	0.1887	0.1966	0.1819	0.2064
	Gini Index	0.7263	0.7576	0.9833	0.9638	0.9664	0.9622
	MSE-BP	6.0433	1.0951	0.21728	0.43873	0.63497	0.46815
	MSE-OMP	0.22351	1.0854	1.02E-29	0.38539	0.40262	0.48042
Doppler	L ₀	0.2217	0.0117	0.0127	0.0073	0.0098	0.0073
	L _p (p=1)	2.9407	0.0582	0.0571	0.0328	0.0354	0.0320
	L _n (p=0.5)	1573.3	28.841	36.7560	2.4776	3.8096	2.4683
	Log	0.3922	0.0118	0.0112	0.0089	0.0093	0.0086
	tanh (a=2, b=3)	0.3679	0.0316	0.0300	0.0171	0.0210	0.0165
	Kurtosis	0.0537	0.0841	0.1065	0.1025	0.1551	0.1225
	Gini Index	0.8914	0.9027	0.8763	0.9845	0.9787	0.9844
	MSE-BP	0.085698	0.017692	0.014163	0.00070946	0.0027596	0.00094719
	MSE-OMP	0.0040537	0.030266	0.021305	1.92E-05	6.80E-04	8.70E-05
Ramp	L ₀	0.4390	0.0059	0.0049	0.0039	0.0034	0.0039
	L _p (p=1)	2.5971	0.0538	0.0259	0.0235	0.0221	0.0241
	L _n (p=0.5)	2768.0	50.986	6.0158	0.6948	0.5388	0.7179
	Log	0.4171	0.0086	0.0060	0.0061	0.0058	0.0064
	tanh (a=2, b=3)	0.9316	0.0183	0.0102	0.0096	0.0087	0.0102
	Kurtosis	0.1667	0.1502	0.2504	0.2336	0.2769	0.2594
	Gini Index	0.7142	0.7638	0.9641	0.9932	0.9943	0.9930
	MSE-BP	0.099817	0.0052462	0.00017928	1.21E-05	2.29E-07	2.00E-05
	MSE-OMP	0.0014906	0.010011	1.41E-04	1.87E-11	2.90E-14	1.67E-11
Linear Chirp	L ₀	0.7451	0.3330	0.2227	0.1670	0.1914	0.1670
	L _n (p=1)	31.7160	0.6302	0.5267	0.4228	0.4420	0.4290
	L _n (p=0.5)	64916.0	1177.90	845.56	460.15	532.37	477.22
	Log	3.0019	0.1612	0.1370	0.1201	0.1227	0.1212
	tanh (a=2, b=3)	1.0000	0.7250	0.5140	0.3624	0.3925	0.3731
	Kurtosis	0.0005	0.0007	0.0020	0.0029	0.0030	0.0028
	Gini Index	0.0098	0.2771	0.4773	0.6623	0.6276	0.6522
	MSE-BP	0.4914	0.6083	0.5527	0.5452	0.5486	0.5575
	MSE-OMP	0.3728	1.1850	1.1756	1.1411	1.0732	1.2488

Table 7 Sparseness Measures of 1-D Signals (Signal length =4096, sample=512).

		FFT	DCT	WAVELET			
				Haar	Coiflet	Db4	Symlet
Heavisine	L ₀	0.5933	0.0103	0.0193	0.0054	0.0063	0.0063
	L _p (p=1)	11.7330	0.1949	0.2292	0.1415	0.1674	0.1536
	L _n (p=0.5)	13650	184.39	146.36	4.5271	6.1765	4.9255
	Log	0.8732	0.0196	0.0321	0.0127	0.0161	0.0136
	tanh (a=2, b=3)	0.9175	0.0335	0.0450	0.0127	0.0144	0.0128
	Kurtosis	0.3519	0.2755	0.3760	0.1941	0.1583	0.1643
	Gini Index	0.8614	0.8966	0.9476	0.9970	0.9964	0.9969
	MSE-BP	9.5268	0.019721	0.053432	1.57E-05	8.52E-06	1.62E-05
	MSE-OMP	0.0075	0.0187	0.0321	2.25E-06	1.42E-06	1.88E-06
Bumps	L ₀	0.4763	0.0332	0.0208	0.0149	0.0188	0.0193
	L _p (p=1)	12.1710	0.1715	0.1223	0.0998	0.1016	0.0988
	L _n (p=0.5)	18003	230.590	71.547	21.516	21.879	20.813
	Log	0.9151	0.0409	0.0295	0.0257	0.0264	0.0254
	tanh (a=2, b=3)	0.8296	0.0838	0.0504	0.0384	0.0391	0.0378
	Kurtosis	0.0326	0.0389	0.0429	0.0525	0.0468	0.0519
	Gini Index	0.8545	0.8708	0.9477	0.9757	0.9761	0.9761
	MSE-BP	0.5196	0.2010	0.0593	0.0804	0.0470	0.0794
	MSE-OMP	0.0606	0.0187	0.0346	0.0141	0.0122	0.0244
Blocks	L ₀	0.7173	0.0535	0.0112	0.0237	0.0247	0.0244
	L _p (p=1)	27.6350	0.4018	0.2007	0.2434	0.2514	0.2430
	L _n (p=0.5)	55271.0000	736.4300	12.1950	45.1550	41.1600	44.6570
	Log	1.9268	0.0698	0.0309	0.0435	0.0444	0.0440
	tanh (a=2, b=3)	0.9954	0.1519	0.0200	0.0518	0.0506	0.0515
	Kurtosis	0.1872	0.2047	0.1884	0.1960	0.1817	0.2062
	Gini Index	0.7537	0.7841	0.9914	0.9802	0.9815	0.9799
	MSE-BP	6.055	0.40919	7.60E-09	0.15354	0.17859	0.1532
	MSE-OMP	0.1446	0.4088	1.41E-29	0.0824	0.0462	0.0655
Doppler	L ₀	0.1274	0.0078	0.0076	0.0039	0.0051	0.0044
	L _p (p=1)	2.9415	0.0412	0.0419	0.0231	0.0250	0.0228
	L _n (p=0.5)	1688.6000	22.6940	42.3990	1.7667	2.8356	1.7841
	Log	0.2892	0.0088	0.0084	0.0061	0.0066	0.0059
	tanh (a=2, b=3)	0.2053	0.0217	0.0202	0.0098	0.0120	0.0100
	Kurtosis	0.0537	0.0841	0.1066	0.1000	0.1551	0.1186
	Gini Index	0.9453	0.9501	0.9096	0.9923	0.9893	0.9922
	MSE-BP	0.085693	0.006159	0.0071591	6.46E-05	0.00027183	9.24E-05
	MSE-OMP	0.0018	0.0065	0.0053	5.06E-06	3.33E-05	5.16E-06
Ramp	L ₀	0.4387	0.0042	0.0027	0.0022	0.0017	0.0024
	L _p (p=1)	2.8176	0.0411	0.0185	0.0166	0.0158	0.0172
	L _n (p=0.5)	5585.6000	72.4820	6.2066	0.5263	0.4087	0.5595
	Log	0.4175	0.0061	0.0040	0.0040	0.0038	0.0043
	tanh (a=2, b=3)	0.9316	0.0130	0.0061	0.0060	0.0050	0.0065
	Kurtosis	0.1667	0.1500	0.2522	0.2337	0.2769	0.2593
	Gini Index	0.7365	0.7819	0.9750	0.9965	0.9970	0.9963
	MSE-BP	0.10012	0.0028821	6.78E-05	8.58E-09	2.25E-09	3.39E-09
	MSE-OMP	0.0009	0.0032	2.54E-05	1.28E-11	4.82E-14	9.97E-12
Linear Chirp	L ₀	0.7466	0.3276	0.2188	0.1694	0.1848	0.1704
	L _p (p=1)	44.9710	0.6321	0.5263	0.4229	0.4409	0.4269
	L _n (p=0.5)	184120.0000	2363.5000	1683.5000	915.4600	1058.1000	940.0700
	Log	3.3053	0.1619	0.1371	0.1200	0.1222	0.1207
	tanh (a=2, b=3)	1.0000	0.7268	0.5102	0.3662	0.3906	0.3700
	Kurtosis	0.0002	0.0004	0.0010	0.0015	0.0021	0.0016
	Gini Index	0.0071	0.2761	0.4801	0.6624	0.6280	0.6555
	MSE-BP	0.4943	0.5862	0.5781	0.6071	0.5748	0.5872
	MSE-OMP	0.4044	0.9545	1.0680	0.9360	0.9230	1.0400

The reconstructed block and Heavisine signal from an original signal length of 4096, using 400 CS samples are shown in Figure(s) 8 - 9.

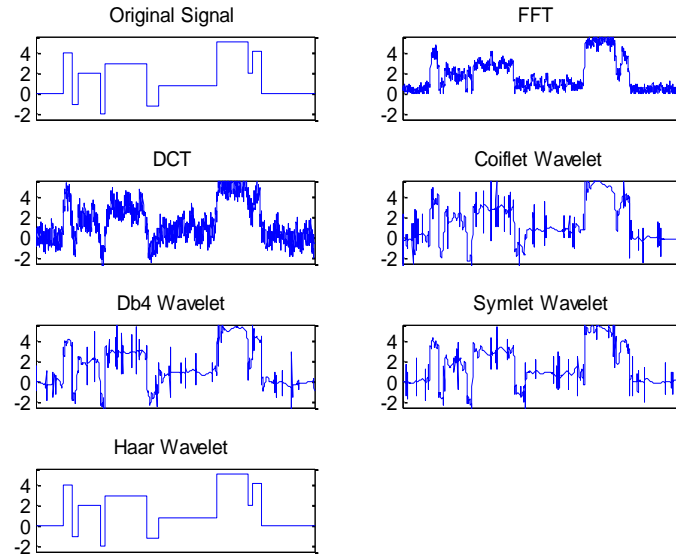


Figure 8 Block signal reconstruction, signal length 4096, number of samples 400.

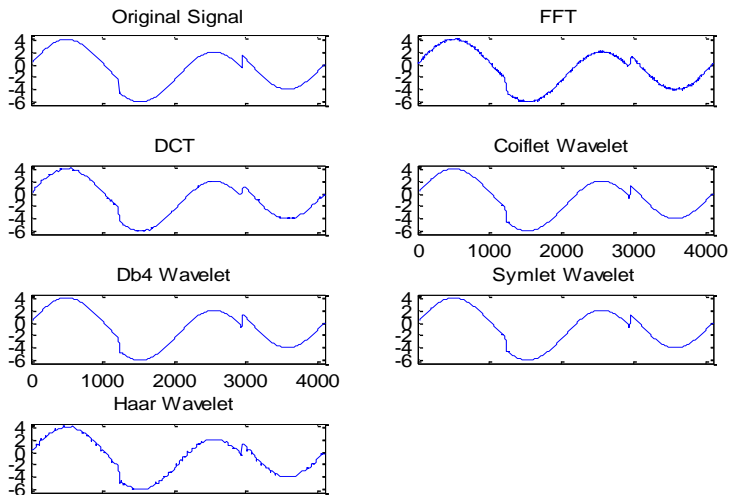


Figure 9 Heavisine signal reconstruction, signal length 4096, number of samples 400.

2.2.3 Results and Discussions of 1-D Compressive Sampling Signal Reconstruction with Noise

For the noisy situation, two different scenarios were considered and they are illustrated in Figure(s) 10 and 11. In the first scenario shown in Figure 10, an additive

white Gaussian noisy channel was considered. In this case, it was assumed that the original signal does not contain noise and noise was added to the decimated data during transmission. Hence the result of the sparseness measure is not affected. However, we tried to investigate which basis result in the best signal reconstruction, even after the transmitted decimated samples have been corrupted by noise.

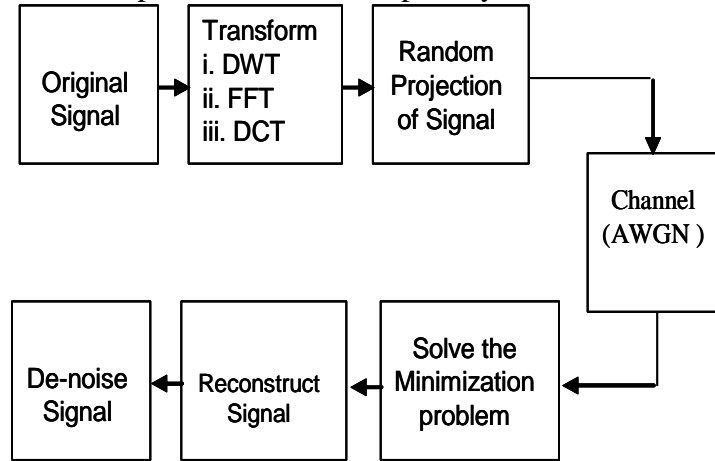


Figure 10 CS Signal reconstruction in a Noisy Channel.

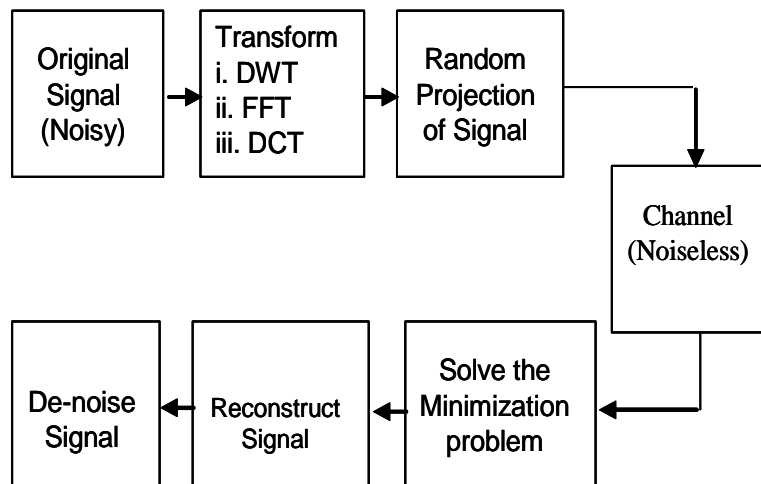


Figure 11 CS Signal reconstruction in a Noiseless Channel with original noisy signal.

In Figure 11, a situation whereby the original signal is corrupted by Gaussian noise before being transformed by the basis was considered. In this case, the sparseness measures were re-evaluated and the results obtained for the 10 dB noise level in the original signal for the Block signal, are shown in Figure(s) 12- 16. All the sparseness measures predicted that the best basis for the block signal reconstruction is Haar wavelet, only the Kurtosis measure predicted otherwise, the plot from the kurtosis was not included.

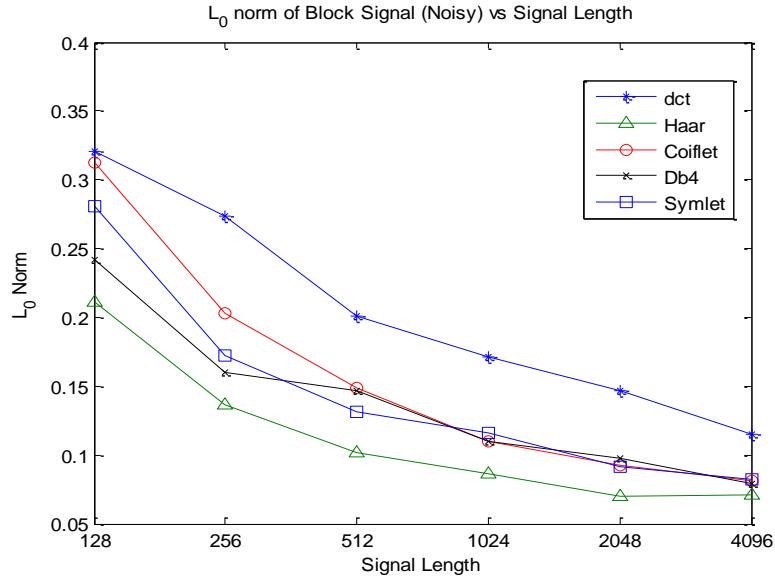


Figure 12 Blocks Sparsity – l_0 Pseudo-Norm (noisy).

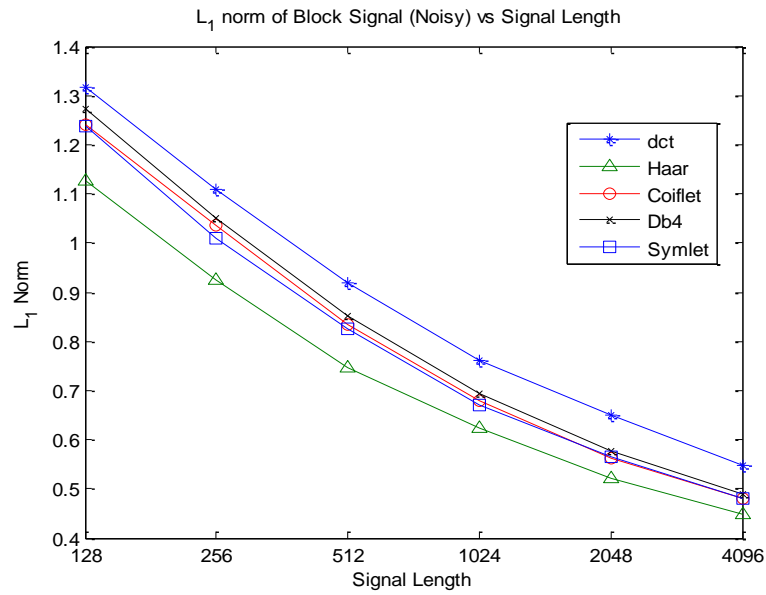


Figure 13 Blocks Sparsity – l_1 Norm (noisy).

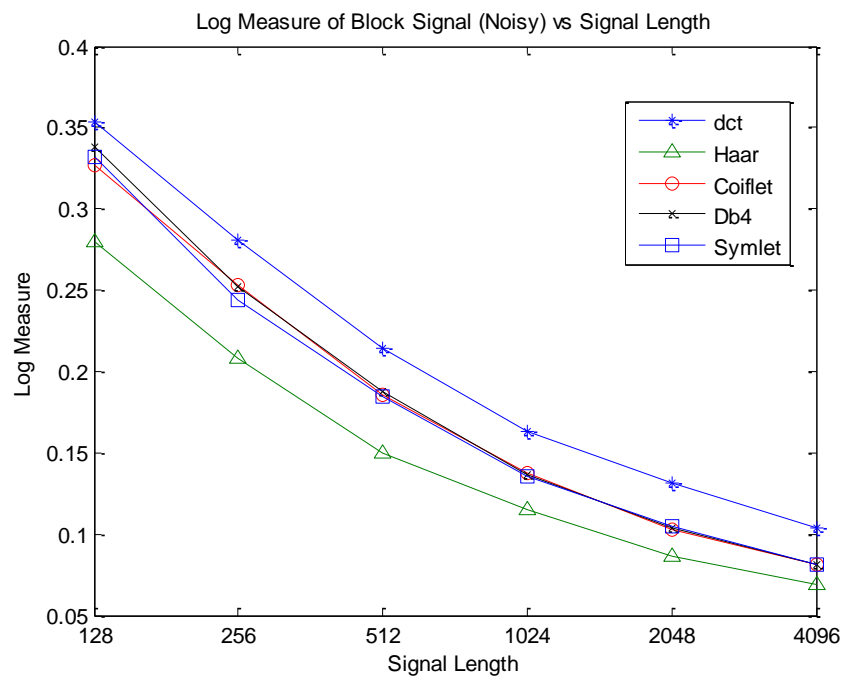


Figure 14 Blocks Sparsity – Log Measure (noisy).

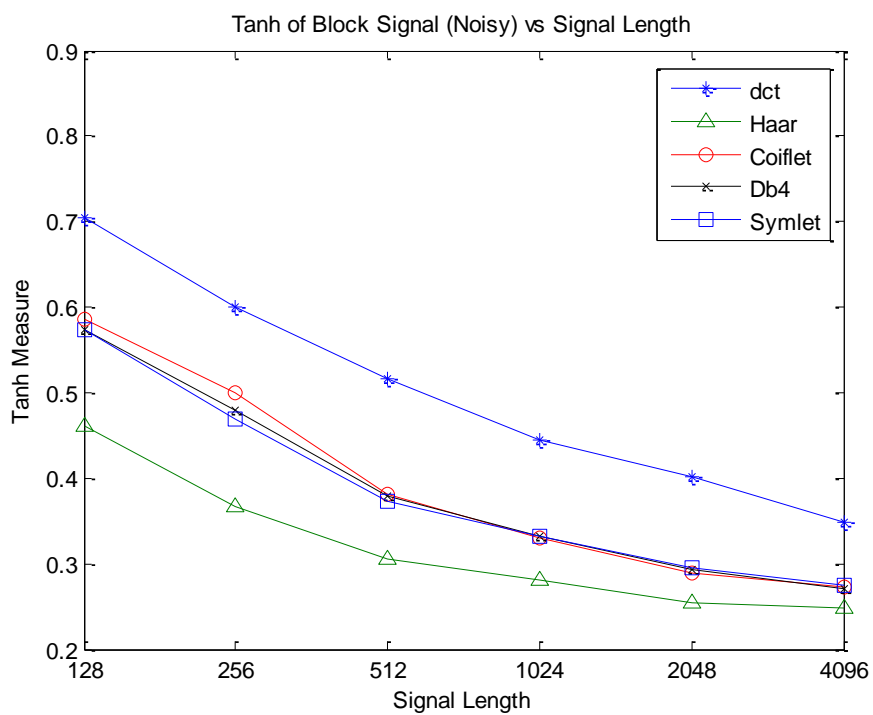


Figure 15 Blocks Sparsity – Tanh Measure (noisy).

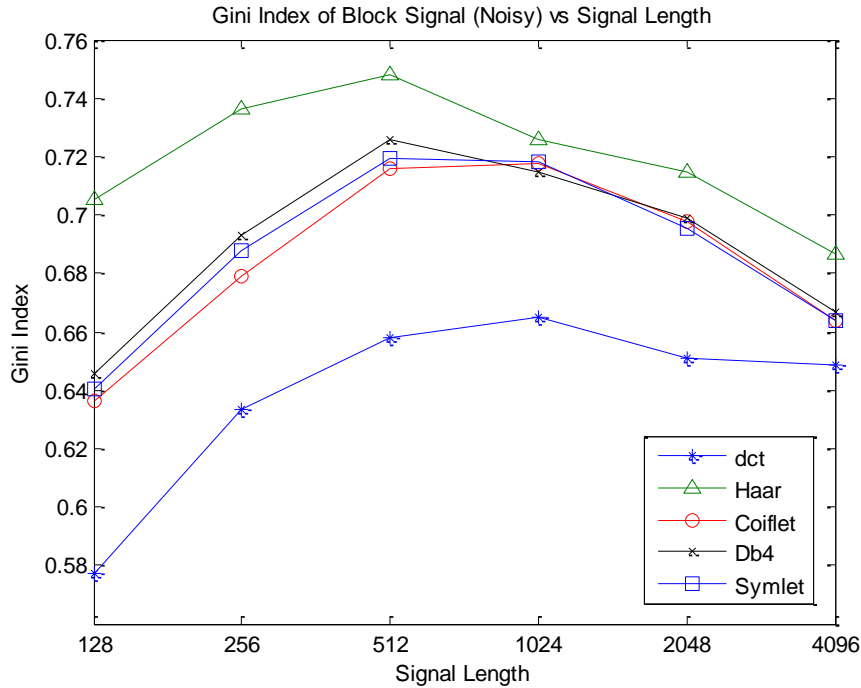


Figure 16 Blocks Sparsity – Gini Index Measure.

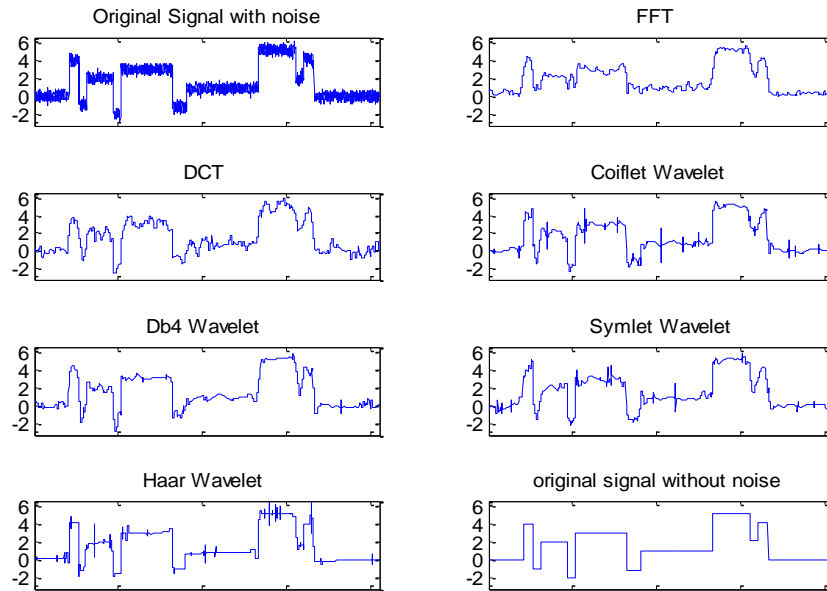


Figure 17 Noisy Block signal reconstruction, signal length 4096, samples size 400.

For each one of the sparse signals considered earlier, the effect of a noisy communication channel on the reconstructed signals using compressive sampling based signal reconstruction was also investigated. At different noise level, using the orthogonal matching pursuit algorithm, the results obtained were shown in Figure(s) 18 to 22. For the Heavisine signal type at different SNR, the bases with the lowest MSE are symlet,

coiflet and Db4 which correlates with the earlier prediction of the sparseness measures. Figure 19 is the plot obtained for the bump signal while the plot for the block signal is shown in Figure 20. For the block signal, under different noise condition, the haar wavelet was clearly the best basis for signal reconstruction as predicted by the sparseness measures while for the bump signal, it can be seen that the DCT is obviously not a good sparsifying basis to be used. Similar results were obtained for the Doppler and ramp signals and the plots are shown in Figure(s) 21 and 22 respectively.

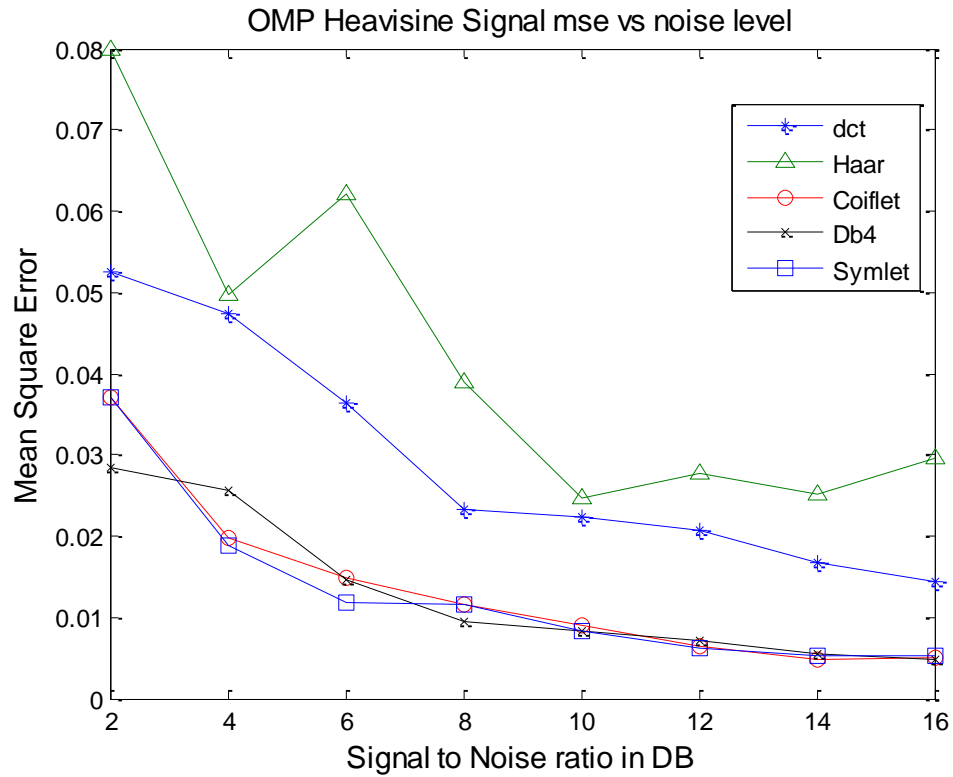


Figure 18 Heavisine Signal-mean square error vs SNR using OMP.

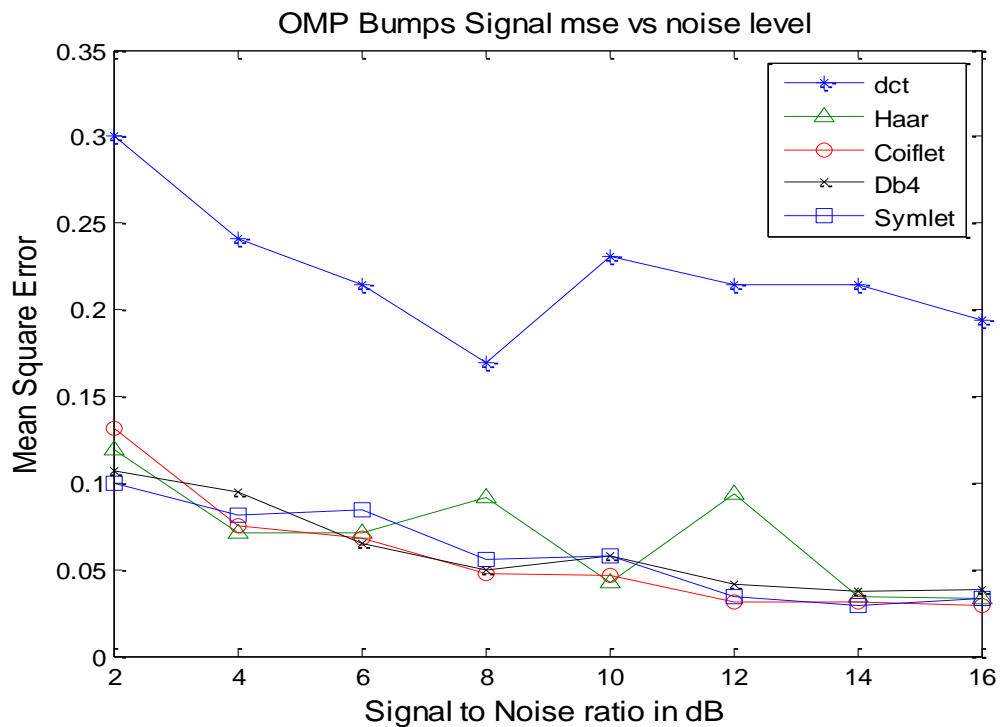


Figure 19 Bumps Signal-mean square error vs SNR using OMP.

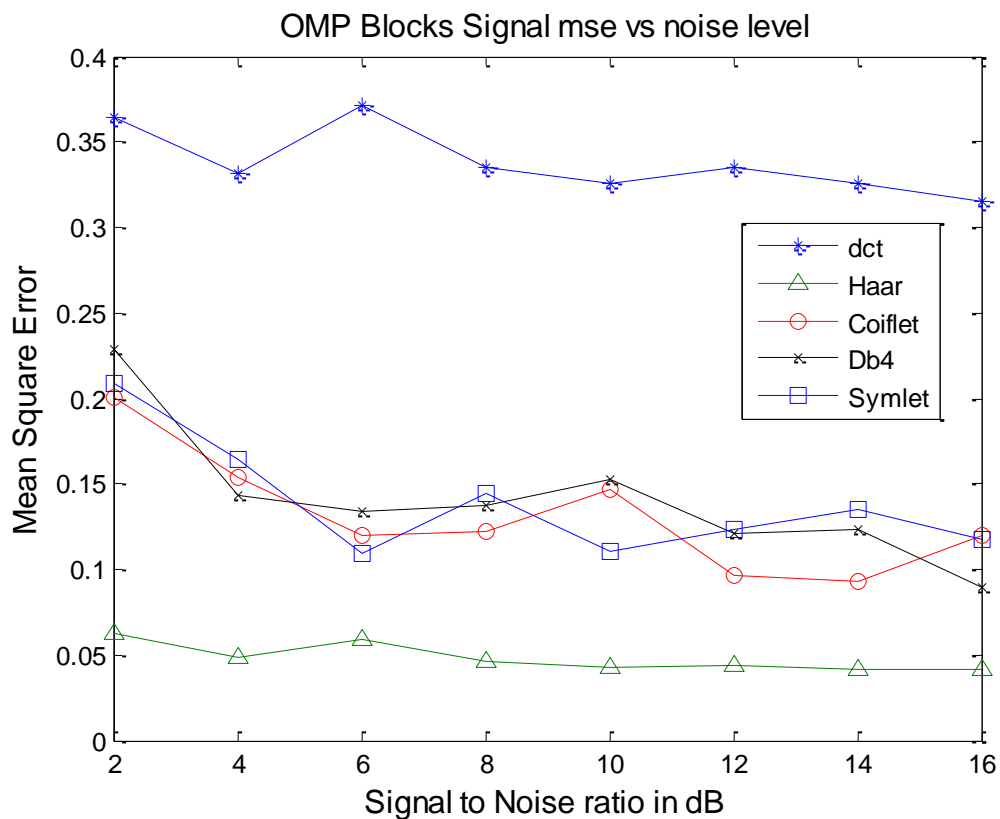


Figure 20 Blocks Signal mean square error vs SNR using OMP.

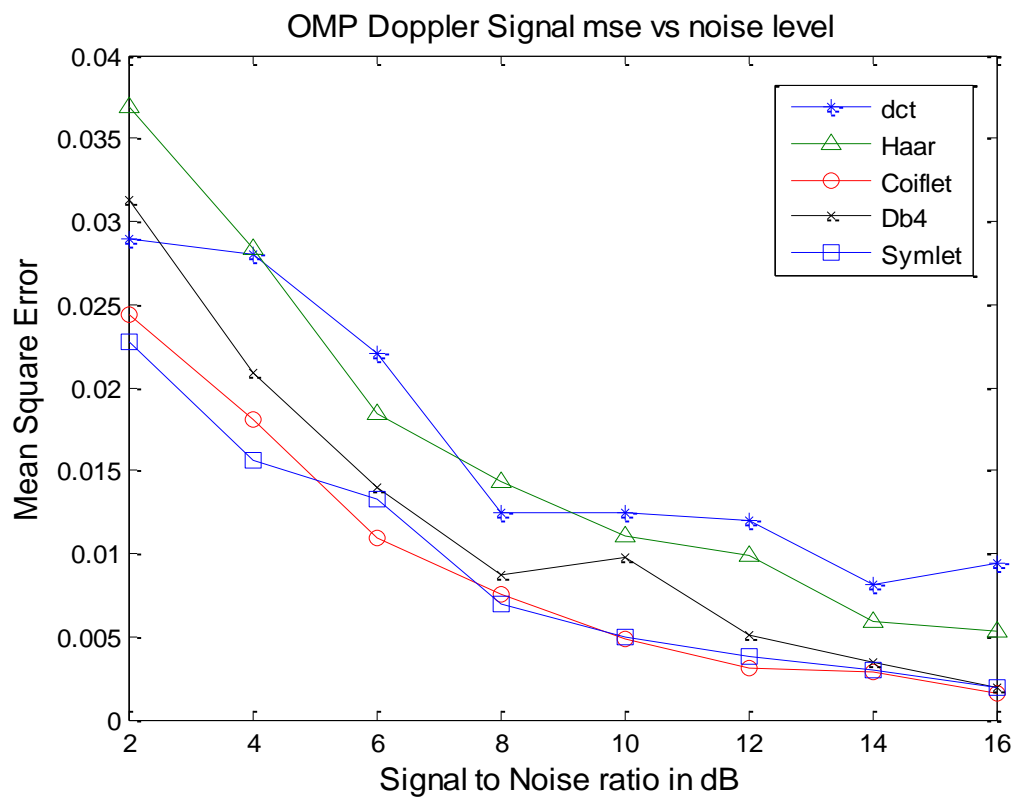


Figure 21 Doppler Signal-mean square error vs SNR using OMP.

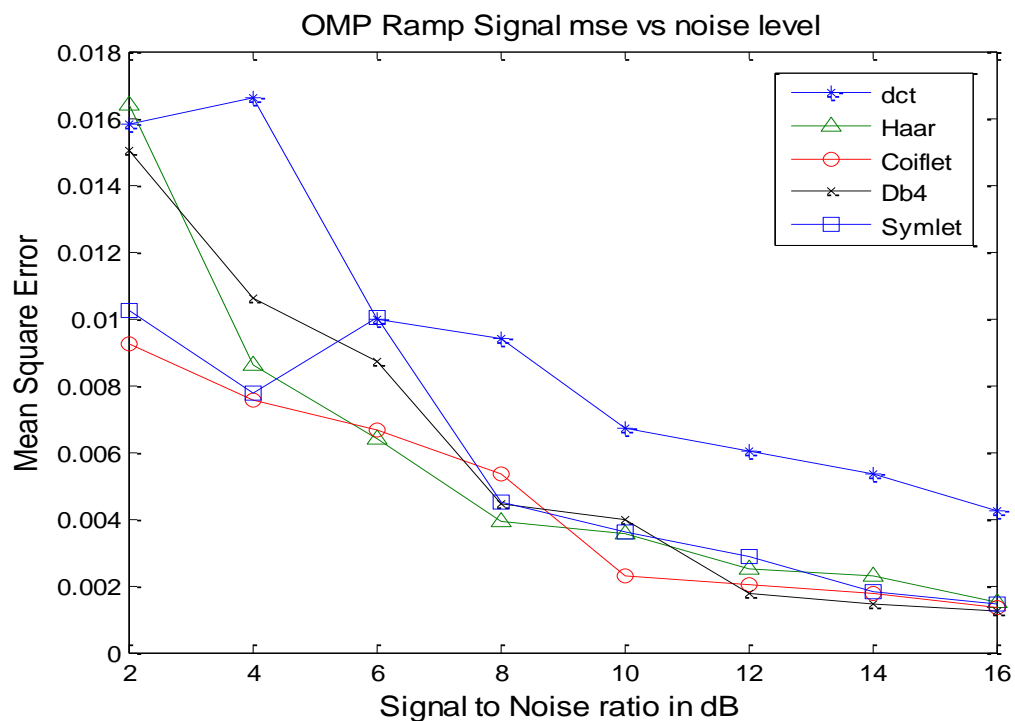


Figure 22 Ramp Signal mean square error vs SNR using OMP.

Observations from the various results and data obtained from the simulation show that although the CS measurements may be performed with no *a priori* knowledge about the signal (other than the fact that the signal is sparse or compressible in some basis), the reconstruction error can depend strongly on the choice of basis functions. Hence a means for determining the best sparsifying basis function is necessary. It has been shown that it is possible to predict which sparsifying basis will result into the best CS signal reconstruction. With the result obtained from all the signals, it was discovered that all of the sparsity measures performed reasonably well except for kurtosis, with l_0 norm and Gini index giving a much better performance. The Gini index has some advantages over the other measures. In addition to providing a good indication of signal sparsity, it does not require normalization. Its value always lies between 0 and 1, regardless of the signal length, and is thus a better pointer for decision making when different signal lengths are being considered. The l_0 norm measure, apart from requiring normalization, also requires rounding off the values, since most of the data after transformation are not truly zero.

2.3 Nyquist folding analog-to-information receiver in fading environment

In Cognitive Radio applications as well as battlefield communication systems, dynamic spectrum access or detection is of great importance. In the United States, the FCC recently made a decision to allow white spaces to be used by unlicensed devices. This ruling will make available, the frequency band formally being used by TV stations for analog transmission. The ability to efficiently and effectively, sense or detect the presence of transmitted signal at specific frequencies and bandwidth in the wide banded spectrum will help a great deal in each of the application areas mentioned.

Wideband spectrum monitoring is a major challenge in Cognitive Radio [22]. Current techniques used in identifying or detecting white spaces in the frequency spectrum include; transmitter detection, cooperative detection, and interference-based detection [23]. Transmitter detection approach focuses on detecting weak signals from primary transmitter by carrying out observation at the end user. There exist three main techniques of achieving this, namely; matched filter detection, energy detection [24], and cyclostationarity feature detection [25].

Opportunistic transmission and detection requires the ability to detect holes in the spectrum, effectively and efficiently makes use of the available spectrum by sending as many information as possible within the shortest period of time. In the past few decades, there has been tremendous research efforts in the area of digital signal processing, however, the performance of analog-to-digital converter (ADC) has been much slower, averaging roughly 1.5 bits / 8 years [26], [27].

Compressive Sampling (CS) can be used to collect data at rates lower than what Nyquist specifies, hence can help in overcoming the limitations of ADC in wideband spectrum monitoring for CR applications [28]. The underlying principle of CS is that signals that are known to be sparse in some known basis, can be sampled based on the information rate as opposed to the Nyquist criteria of twice the total bandwidth. In this case, a sample rate much lower than that implemented by conventional digital receiver techniques is possible as long as the spectrum is sparsely occupied. This information sampling and recovery idea is also referred to as analog-to-information [27] (A2I).

The Nyquist Folding Receiver (NYFR) has recently been proposed as an A2I approach for sparse wideband RF applications [29]. While many CS techniques involve random projections followed by a computationally expensive reconstruction [28], [1]-[2], the NYFR performs analog compression via a non-uniform sampling process that induces a chirp-like modulation on each received signal. This induced modulation can be measured using time-frequency analysis techniques to determine the original RF band of origin without full signal reconstruction. In this paper, we investigate the viability of achieving signal detection and identification of original RF band of signals present in the NYFR data, when the original signal passes through the presence of multiplicative (Rice) and additive (white Gaussian) noise.

2.3.1 Nyquist Folding Analog-to-Information Receiver

Physical realizations of CS receivers to perform A2I conversion include random filters [30], random pre-modulation followed by integration [28], [31], structured random sampling [32], and the NYFR [29].

The NYFR performs pulsed sampling directly at RF using a frequency modulated carrier sample clock and allows multiple Nyquist zones (defined by half of the average RF sample rate) to fold into an analog interpolation filter as shown in Figure 2.23. Figure 2.23 illustrates noise being added to the original signal during transmission. The NYFR does not use an anti-aliasing filter prior to sampling; instead it makes use of a wideband pre-select filter $H(\omega)$. The interpolation filter makes it possible to decouple the ADC clock from the sampling clock. While the ADC clock is uniform, the sampling clock is not, it is modulated.

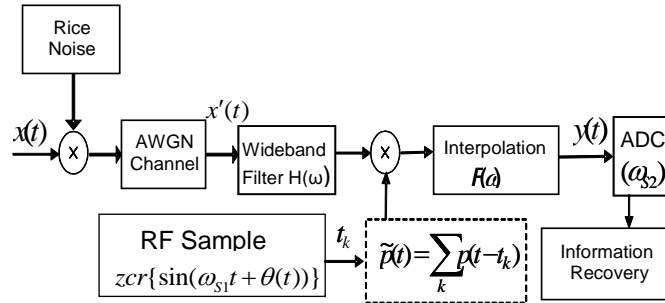


Figure 23 Nyquist Folding A-to-I Receiver Architecture

The RF sample times correspond to the zero crossing time for the rising voltage of the modulated sample clock. As shown in [29], the received signal has an induced modulation of the same form as the RF sample clock modulation with a modulation scale factor that depends on the Nyquist zone of the signal. In the special case of a narrowband modulated (phase or frequency) signal $\phi(t)$ with carrier frequency ω_{s1} such that

$$\phi(t) = \omega_{s1}t + \theta(t) \quad (28)$$

Supposing the input signal is a narrowband signal with center frequency ω_c and information modulation $\psi(t)$ defined by

$$x'(t) = \cos(\omega_c t + \psi(t)) \quad (29)$$

Then the normalized pre-envelope at the interpolation filter output will be [29]:

$$\begin{aligned}
y_p(t) &\approx e^{j(\omega_d t + \psi(t) - M\theta(t))}, \\
\omega_d &= |\omega_c - \omega_{s1} k_H| \\
M &= \text{sgn}(N_s - N_F) k_H \\
k_H &= \lceil |N_F - N_s| / 2 \rceil \quad (\lceil * \rceil \text{denotes ceil})
\end{aligned} \tag{30}$$

where ω_d is the carrier (folding frequency) after translation by bandpass sampling, M is the modulation scale factor, k_H is the harmonic selected by the interpolation filter, and N_F and N_s are the signed Nyquist zones of the interpolation filter and RF signal respectively relative to the RF sample rate f_{s1} . The signed Nyquist zone for a signal or interpolation filter centered at f_c is defined by

$$N = \pm \lfloor 2f_c / f_{s1} \rfloor \quad (\lfloor * \rfloor \text{denotes floor}) \tag{31}$$

where the sign is negative for odd (spectrally reversed) Nyquist zones and even otherwise.

Therefore, though multiple signals from different Nyquist zones may alias into the same band, the information from the different signals, including the original RF, can still be recovered based on the fact that the added modulation is different for each Nyquist zone under the condition that the signal environment is relatively sparse so that signals are separable. Because the NYFR does not rely on random projections, the NYFR output may be processed using time frequency methods rather than complex l_1 minimization.

In order to analyze the data obtained from the NYFR system, a time-frequency analysis of the data has to be carried out. The spectrogram which is based on Fast Fourier transform (FFT) has been widely used as one of the methods for time-varying spectral analysis. It has been applied for signal analysis in many applications such as radar, sonar, speech, geophysics and biological signals [33]. The wavelet analysis which is well suited for analysis of transient signals can be used as well. Wavelet uses time-frequency atoms of different sizes that depend on the frequency to break down the signal [34]. Both FFT spectrogram and AWT scalogram has been applied to the analysis of the NYFR data [29], [35].

2.3.2 Ricean Noise and Gaussian Noise

The earlier work [29] did not consider the behavior of the NYFR under noisy condition. We investigated the effect of Rice noise and Gaussian noise on the performance of the NYFR. Gaussian noise is the most widely used noise model for communication system analysis. The Rice noise has amplitude which is Rice distributed. Suppose y_1 and y_2 represents two Gaussian variables, with common variance σ^2 and mean values m_1 and m_2 , the non-centrality parameter ν equals $m_1^2 + m_2^2$. The pdf of the Rice noise is modeled as

$$f(x) = \begin{cases} \frac{x}{\sigma^2} I_0\left(\frac{x\nu}{\sigma^2}\right) e^{-\frac{x^2 + \nu^2}{2\sigma^2}} & x \geq 0 \\ 0 & x < 0 \end{cases} \tag{32}$$

Where the function $I_0(u)$ is the modified zeroth order Bessel function of the first kind defined as

$$I_0(u) = \frac{1}{2\pi} \int_{-\pi}^{\pi} e^{u \cos t} dt \quad (33)$$

The mean value of the Ricean noise is $(2+m)$ and the variance is $4(1+2m)$. The original signal was passed through a combination of both multiplicative Ricean noise and additive white Gaussian noise.

2.3.3 Automatic Detection Algorithm

FFT spectrogram plots and AWT scalogram plots can be used to determine both the folding frequency and the induced modulation bandwidth. This often requires visual inspection of the plotted images. For the purpose of automation and also to remove human error in interpretation of the plots, we worked on developing an algorithm that is capable of automatically predicting the folding frequency of the signals after passing through the NYFR system as well as the induced modulation bandwidth. The algorithm worked on either the spectrogram or the scalogram data. The pseudocode for the algorithm is listed below.

Step 1: Normalize the data from the FFT spectrogram or AWT scalogram. Let us assume that the data is A , the normalized data is define by

$$A_{norm} = \left(\frac{A_{i,j}}{A_{\max} + |A_{\min}|} \right)^p \quad (34)$$

where $p \geq 1$. The effect of p will be investigated in detail in later publication.

Step 2: Compare the data with a threshold γ^* , which was determined heuristically. This will be discussed further in the experimental result section.

Step 3: Set values below the threshold to zero and values \geq the threshold to 1. Values at the detected signal points should be greater than the threshold value.

Step 4: Compute the difference matrix of the new data and find the location of the non-zero elements. This can be used in tracking the point at which the signal begins and ends.

Step 5: Determine the maximum and minimum point for each detected signal.

Step 6: the frequency at which the various signals folds to, the mid-point of the maximum and minimum point.

Step 7: Induced modulation bandwidth is the difference between the maximum and minimum points for each signals.

A flow chart illustration of the algorithm is shown in Figure 24.

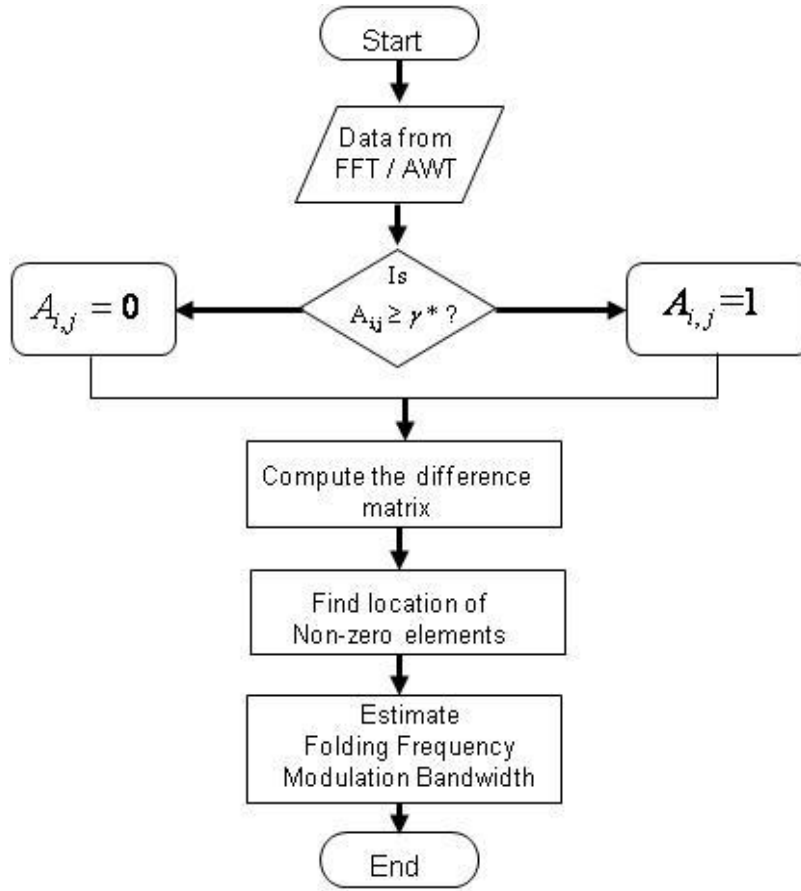


Figure 24 Flow Chart for the detection algorithm

2.3.4 Results and Discussions of Nyquist Folding A-2-I Receiver

In this section, we examine some experimental results using simulated NYFR data. In this example, the RF sample clock ramps up and down between 1995 Msps and 2005 Msps over a 2 μ sec period, resulting in a sample rate of 2 Gsps \pm 10 MHz. There are two signals in the spectrum originally, a 10.3GHz signal as well as a 10.6GHz signal. Fig. 3 shows the FFT spectrogram of the NYFR data in a noiseless situation.

The signal at 10.3 GHz will fold to 300 MHz with an induced modulation bandwidth of \pm 25 MHz ($M = \text{round}(10.3 / 2.0) = 5$). The second signal at 10.6GHz will fold to 600 MHz, with an induced modulation bandwidth of \pm 25 MHz ($M = \text{round}(10.6 / 2.0) = 5$).

The earlier work did not consider the behavior of the NYFR under multiplicative noise condition. We investigated the effect of Ricean noise and Gaussian noise on the performance of the NYFR. Figure 25 shows the plot obtained for a situation based on Figure 23 (a combination of Ricean multiplicative noise and additive Gaussian noise) whereby the SNR is 3 dB (SNR was measured by comparing $x'(t)$ to $x(t)$ in Figure 23. Plots obtained under only Gaussian or Rice channel conditions are similar to Figure 26. We carried out simulations under different signal-to-noise ratio conditions. Table 8 lists the result obtained from our analysis.

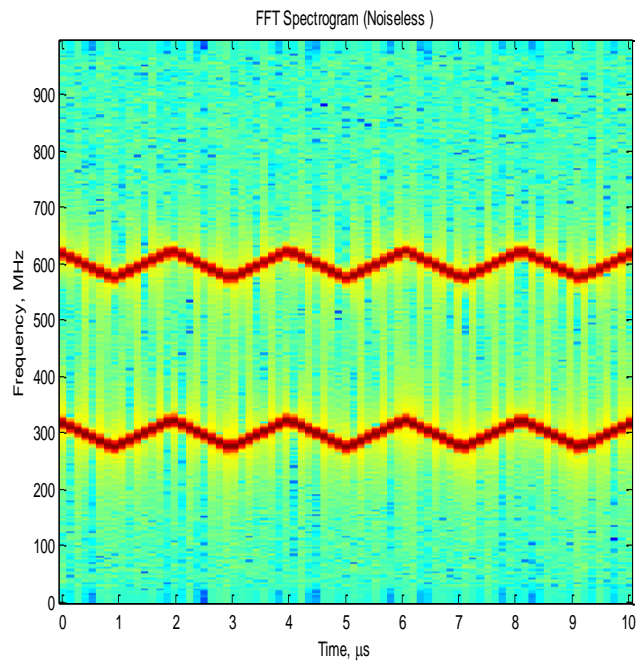


Figure 25 Spectrogram of data (Noiseless)

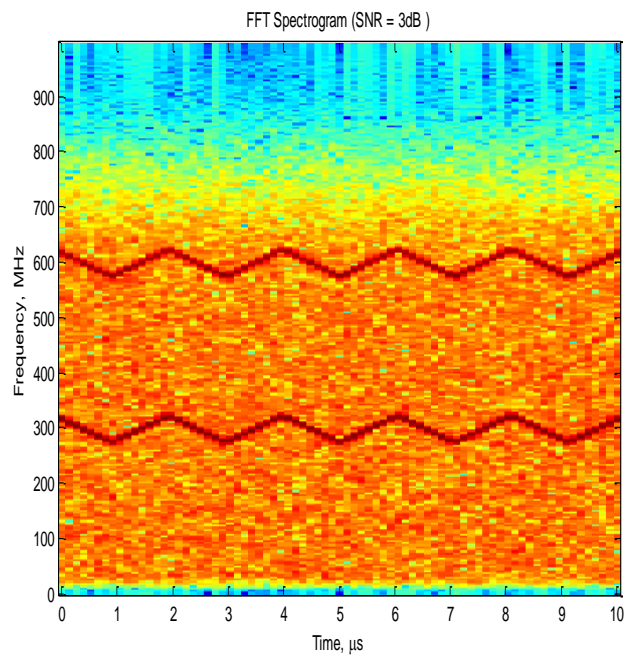


Figure 26 Spectrogram of data (Gaussian and Rice channel)

Table 8: Percentage Error Analysis

Actual Carrier Freq. (GHz)	SNR	Folding Frequency			Induced Modulation Bandwidth			Estimated Carrier Freq. (GHz)	Carrier Freq. Est. Error (%)
		Theory MHz	Estimated	Est. Error %	Theory MHz	Estimated	Est. Error %		
10.3	Noiseless	300	301	0.3	50	46.9	6.2	10.301	0.01
	9 dB	300	302	0.6	50	46.7	6.6	10.302	0.02
	6 dB	300	304	1.2	50	52.4	4.8	10.304	0.04
	3 dB	300	305	1.6	50	53.4	6.8	10.305	0.05
10.6	Noiseless	600	599	0.2	50	46.9	6.2	10.599	0.01
	9 dB	600	597	0.5	50	46.8	6.4	10.597	0.03
	6 dB	600	605	0.8	50	52.6	5.2	10.605	0.05
	3 dB	600	607	1.2	50	52.8	5.6	10.607	0.07

We have been able to show that the NYFR system is robust under Rice and Gaussian noisy channel condition. The accuracy of the prediction is very high and the automatic detection algorithm eliminates error associated with visual analyzes of the result and can aid in automated and embedded system. We also intend to look at detection capability under other types of channel conditions such as Nakagami fading channel.

2.4 Dynamic Spectrum Sensing Using Compressive Sensing Algorithms

2.4.1 Problem Statement

Assuming that a cognitive radio receiver receives a signal occupying N consecutive spectrum band with frequency boundaries located at $f_0 < f_1 < \dots < f_n$. The frequency response of the received signal can be categorized based on the level of the power spectral density of the received signal $r(t)$ and is illustrated in Figure 27. If the PSD level is high, medium or low; the spectrum can be considered as black, grey or white. Whereby white hole and sometimes gray spaces can be opportunistically used by the CR for transmission, while the black hole are not to be used in order to avoid interferences.

In a wideband frequency spectrum situation, following Nyquist sampling criteria, very large samples will be required to effectively recover signal $r(t)$. The goal of each Cognitive radio is to effectively sense, classify and estimate the frequency spectrum of signal $r(t)$. Our focus is to be able to sense and classify (identify occupied frequency bands) the signal $r(t)$.

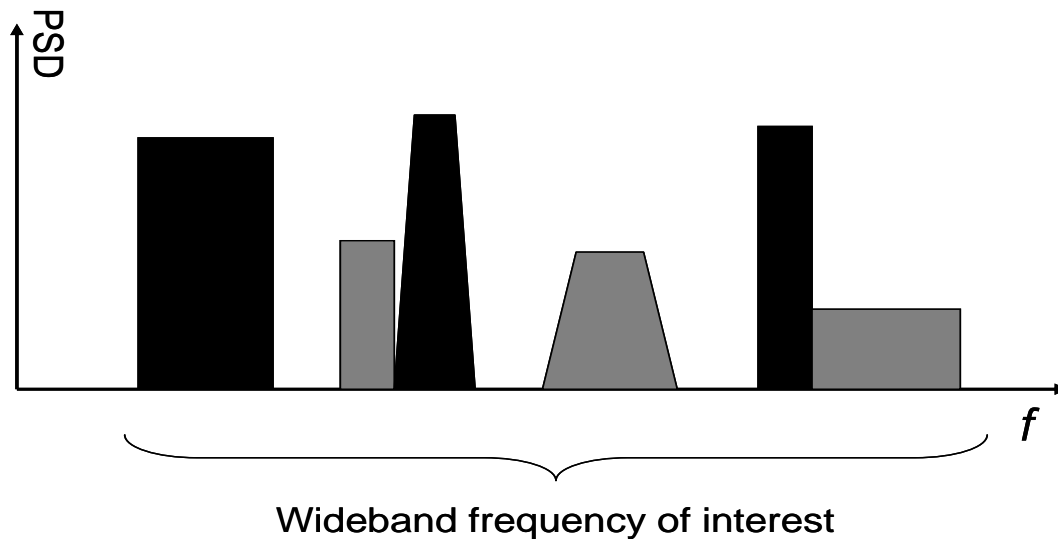


Figure 27 PSD of a wideband spectrum

2.4.2 Results and Discussions of Dynamic Spectrum Sensing

In our simulations based on the theory of compressive sensing, we considered a wideband of interest with the signal of interest being the frequency domain PSD of the spectrum. We employed the idea of CS signal reconstruction in order to detect occupied/unoccupied spectral bands. We revisited the problem discussed in [36] and solve the problem using OMP, BP and LASSO reconstruction algorithm. Our simulations revealed that reconstruction of the signal is possible using any of these three algorithms. Other CS algorithms will be investigated in our next work

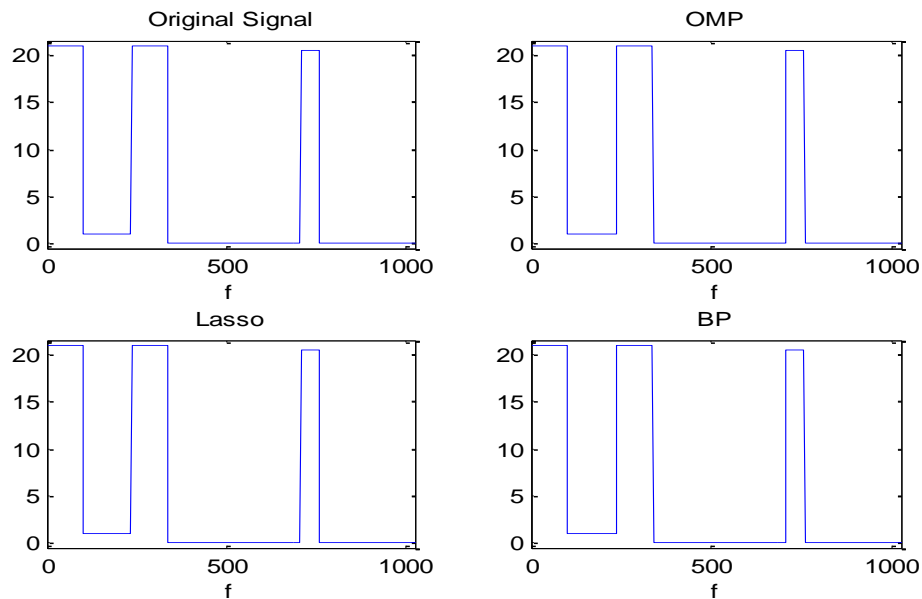


Figure 28 Noiseless Signal frequency response at a compression ratio of 70%

First we consider a noiseless condition and investigated reconstruction at different sampling rates using the earlier mentioned reconstruction algorithms. At a sampling ratio of 70%, the result obtained from the three reconstruction algorithms that were considered is shown in Figure 27.

We also investigated the effect of an AWGN channel condition on the detection through CS reconstruction and the result obtained for a situation whereby the signal to noise ratio is 10dB is shown in Figures 29.

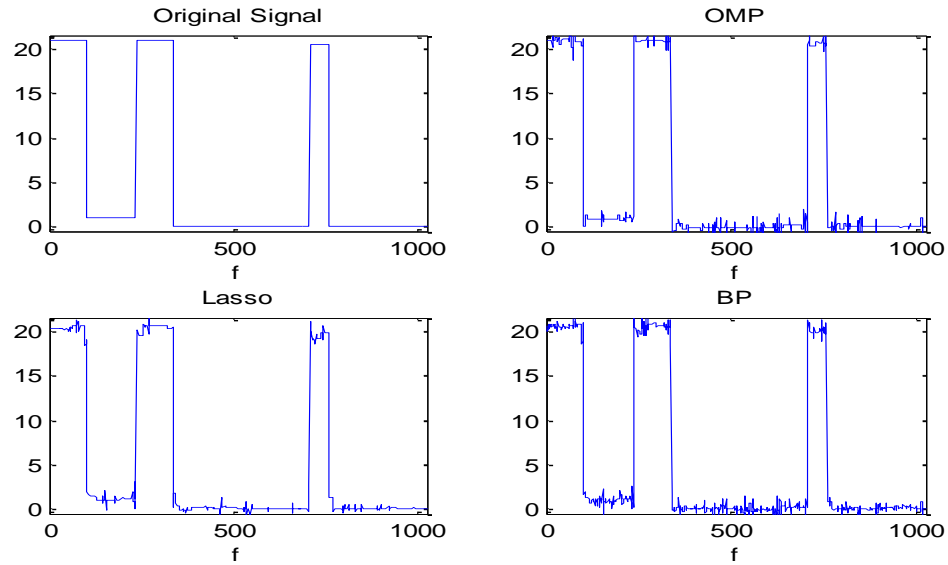


Figure 29a Noisy Signal (10 dB) frequency response at a compression ratio of 70%

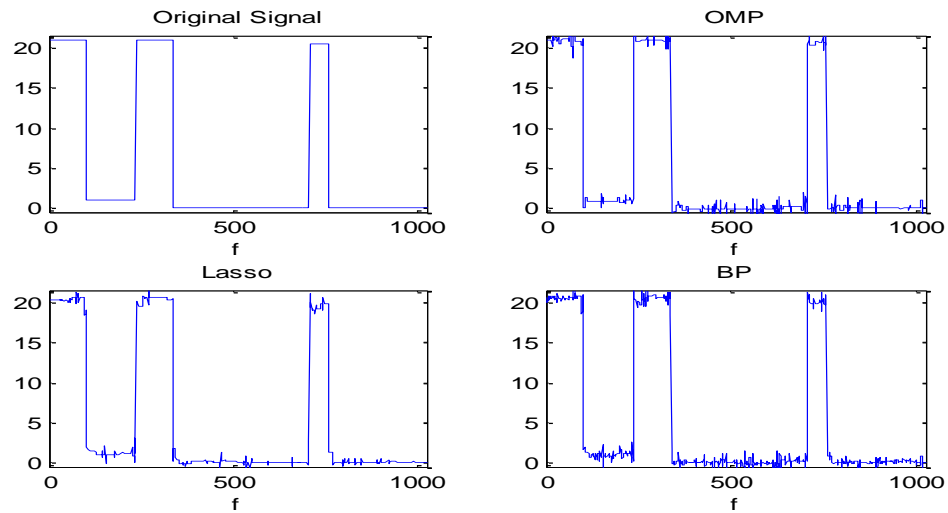


Figure 29b Noisy signal (10 dB) frequency response at a compression ratio of 80%

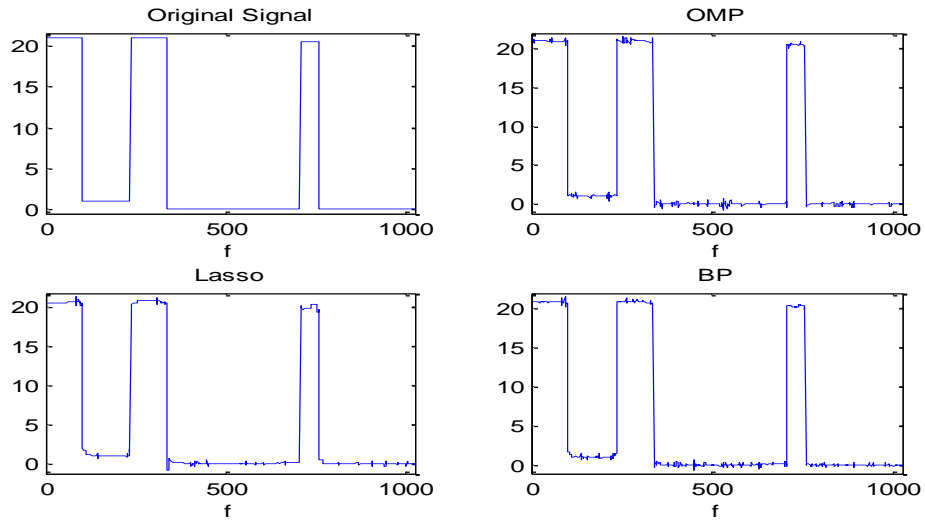


Figure 29c Noisy signal (10 dB) frequency response at a compression ratio of 20%

Figures 30 shows the characterization result obtained using Basis Pursuit algorithm under different signal to noise ratio for an additive white Gaussian noise channel condition. It is a plot of the root mean square error between the reconstructed spectrum and the original spectrum at different noise level for different sampling rates.

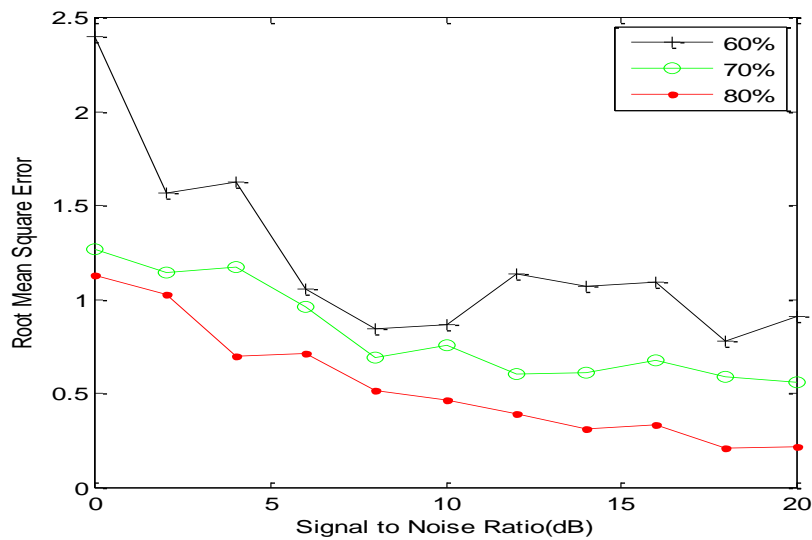


Figure 30a RMS error using BP algorithm and different no. of samples for AWGN channel at 1 iteration

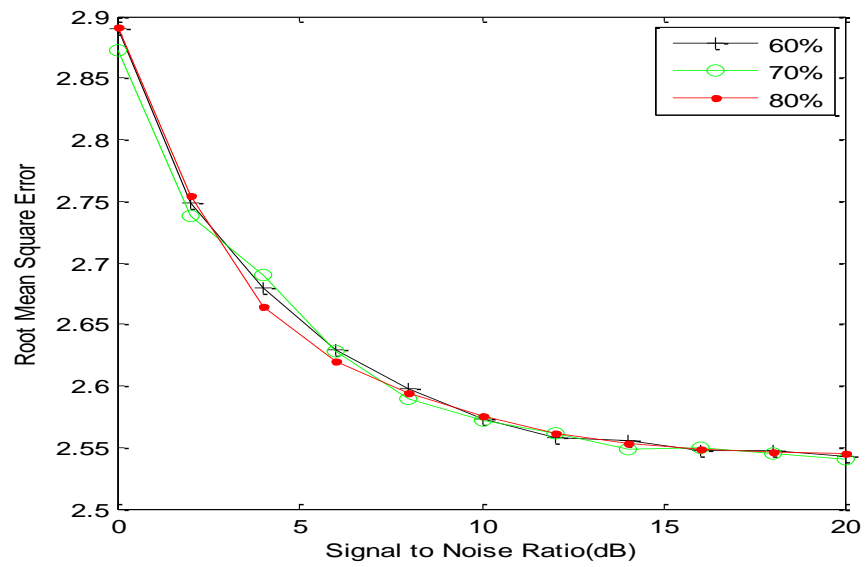


Figure 30b RMS error using BP algorithm and different no. of samples for AWGN channel at 200 iterations

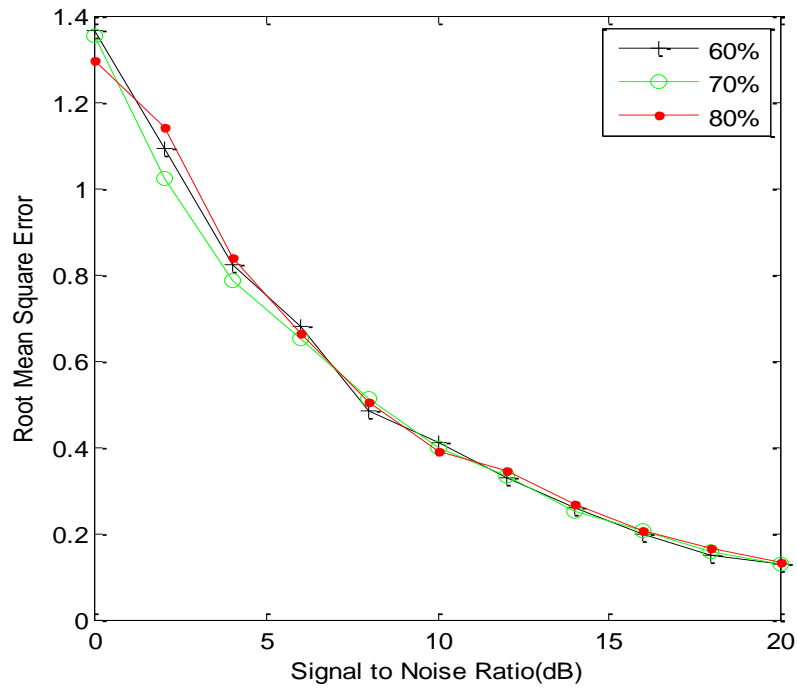


Figure 30c RMS error using BP algorithm and different lower no. of samples for AWGN channel at 5 iterations

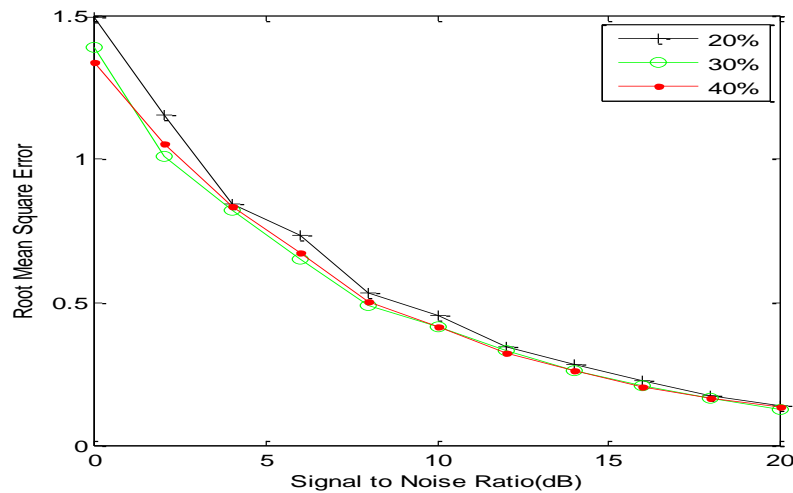


Figure 30d RMS error using BP algorithm and different lower no. of samples for AWGN channel at 200 iterations

Multipath Fading Channel

A principal feature of a cognitive radio (CR) is a reliable spectrum sensing technique which enables the CR to detect white spaces in the frequency band. This allows opportunistic access of the unlicensed (secondary) users to these unoccupied spaces without causing interference to licensed (primary) users. In many scenarios the CR may operate in a multipath fading environment where spectrum sensing must deal with the fading effects of the unknown primary PSD signal. It is important to study the effects of multipath fading on the performance of Compressive Sensing (CS) based spectrum sensing algorithms.

The detection performance of a CR network system is critically affected by the multi-path characteristic of the environment. In a high speed wideband CR network, multi-path fading is one of the most serious transmission difficulties. However, there are also long term fluctuations in the characteristics of the wireless channel depending on the actual position of the Cognitive Radio and the mobile station, that is, in urban areas the signal is affected by multi-path propagation. Theoretical results show that the channel capacity in a multi-path fading environment is always lower than that in a Gaussian noise environment. In a wideband frequency communication channel that has fading characteristics, it is very important to know what the degradations are in channel capacity due to multipath fading, and also to what degree the diversity schemes can bring the channel capacity up or down. The previous chapter centered on the effect of additive noise to CS based spectrum detection. This chapter is centered on investigating the robustness of CS algorithms in spectrum sensing in the presence of additive and multiplicative noise.

The channel amplitude in a Rayleigh fading environment is always lower than that of a Gaussian noise environment. The fading channels are modeled as frequency non-selective slow Rayleigh and Rice fading channels corrupted by AWGN. Rayleigh and Rice fading channels are useful models of real-world phenomena in wireless communications. These phenomena include multipath scattering effects, time dispersion,

and Doppler shifts that arise from relative motion between the transmitter and receiver. The transmission path between a transmitter and receiver can vary from a simple line-of-sight (LOS) path to a non-line-of-sight (NLOS) path, which is a path that is severely obstructed by buildings, mountains, and foliage. Furthermore, when a CR moves in space, the speed of motion impacts how rapidly the signal level fades.

Two widely used models for fading channels are the Rayleigh fading channel and the Rice fading channel, where the Rayleigh fading channel is actually a special case of the Rice fading channel. The Rayleigh model is used when there is NLOS between transmitter

and receiver, and all of the received signal power is due to multipath. The Rice model is used when there is a LOS between transmitter and receiver, but a substantial portion of the received signal power is also due to multipath. When there is LOS between transmitter and receiver and virtually none of the received signal power is due to multipath, the non-fading channel model is used.

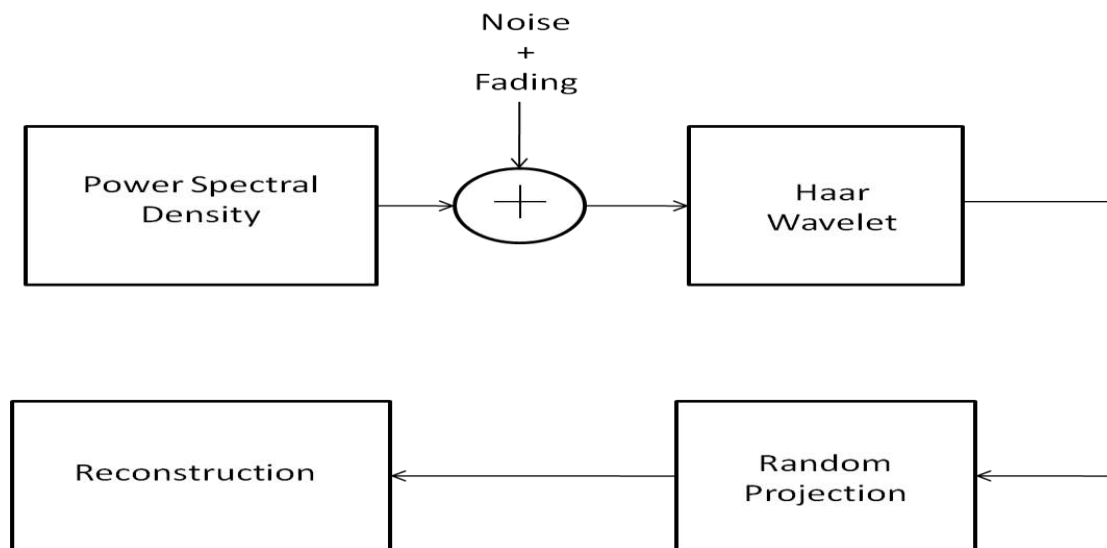


Figure 31 CS Based Spectrum Detection in an AWGN and Fading Channel

Figure 31 illustrates CS based spectrum detection in an AWGN plus fading channel. The process involves a noiseless PSD passed through a AWGN + fading channel. The noisy PSD signal is transformed using Haar wavelet sparsifying basis and fewer coefficients are taken. Random projection of the signal ensures that the PSD can be perfectly reconstructed using CS reconstruction algorithms.

Rayleigh Fading Channel

Rayleigh fading is a type of small-scale fading. If the multipath reflective paths are large in number and are all NLOS, the envelop of the received signal can be statistically expressed by using a Rayleigh fading distribution. The Rayleigh fading

distribution has a probability density function given by

$$p(r) = \begin{cases} \frac{r}{\sigma^2} \exp\left(-\frac{r^2}{2\sigma^2}\right), & r \geq 0 \\ 0, & \text{otherwise} \end{cases} \quad (35)$$

Where r is the envelop amplitude of the received signal, and σ^2 is the time-average power of the multipath signal. The probability of the envelop of the received signal not exceeding a specified value of R , is given by the expression

$$P(R) = \Pr(r \leq R) \quad (36)$$

$$= \int_0^R p(r) dr \quad (37)$$

$$1 - \exp\left(-\frac{R^2}{2\sigma^2}\right) \quad (38)$$

The Rayleigh faded component is also known as random, scatter, or diffuse component [22].

In rural areas there are only a few scatterers, hence the channel is similar to an AWGN channel. Therefore the performance of CS algorithms for the AWGN channel and the Rayleigh fading channel is investigated. A Rayleigh-type fading with arbitrary fading rate was assumed for the signal to get an understanding of the system performance in a fast fading environment. Rayleigh fading occurs when a transmitted signal passes through a medium where there are a large number of scatterers. The results (Figures 32 and 33) are generated to show the degradation of channel capacity in a Rayleigh fading and additive noise environment and the performance of CS algorithms for spectrum hole detection.

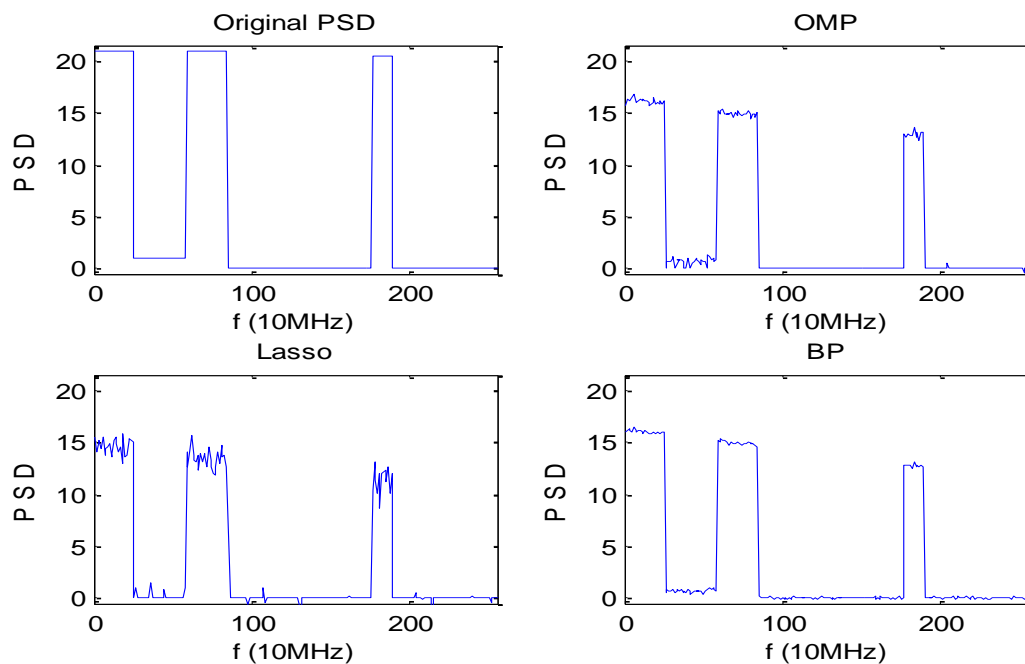


Figure 32 Noisy PSD (Rayleigh) at a Compression Ratio of 60%.

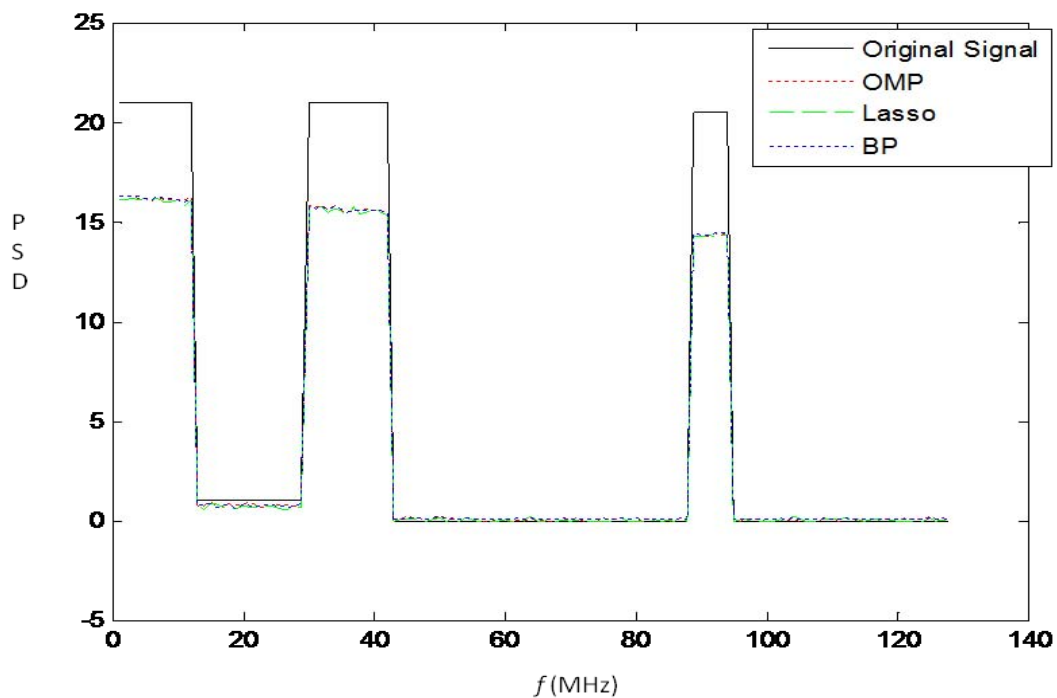


Figure 33 Noisy PSD (Rayleigh) at a Compression Ratio of 80%.

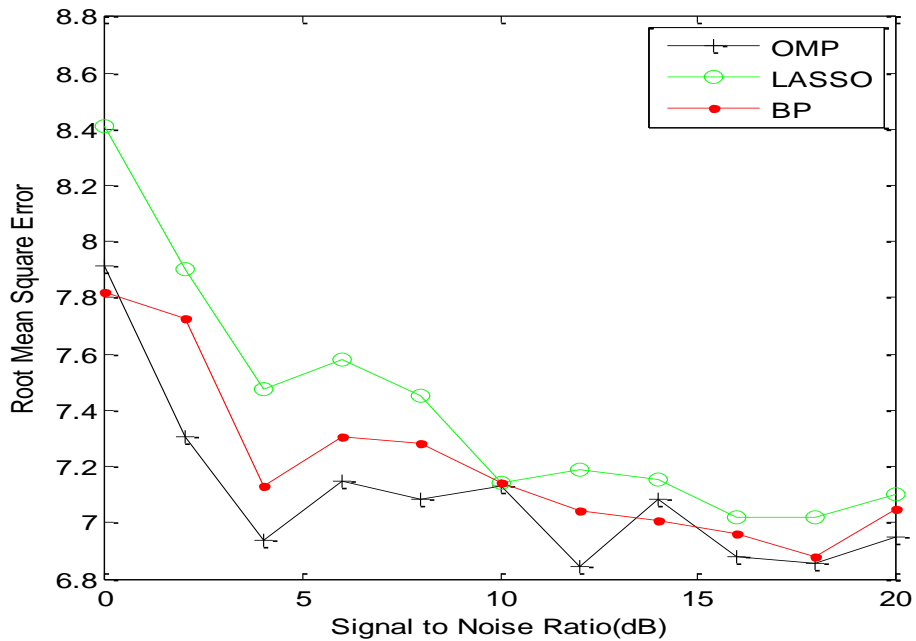


Figure 34 RMS Error Using CS Algorithms of Noisy PSD (10 dB) at 70% Sampling Measurement

Figures 32 and 33 shows the performance of BP, OMP, and LASSO in a noisy AWGN and Rayleigh fading channel. The effect of fading rate on a CR network system performance was evaluated. Figure 33 gives precise information on the amplitude degradation of the reconstructed spectrum by BP, OMP, and LASSO reconstruction algorithm. This amplitude degradation is not necessarily a problem in spectrum sensing since the frequency occupancy is distinctively known. Although significant error occurs in the magnitude of the characterization based on Rayleigh fading channel plus AWGN in comparison to just AWGN channel, this is not necessarily a problem since the goal is to determine the occupied frequency band in the spectrum.

Root mean square error is employed in Figure 34 as a performance metric to investigate the algorithm with the best performance. Despite the fact that OMP performed better at 70% sampling ratio the three algorithms had the same result at 10 dB SNR.

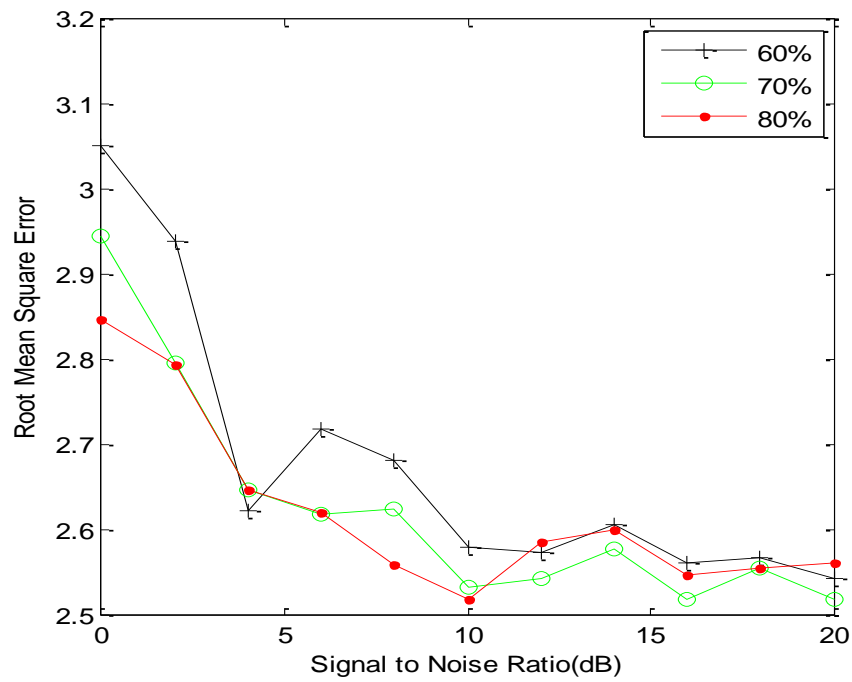


Figure 35 RMS Error Using BP Algorithm at Different Number of Samples for Noisy Channel

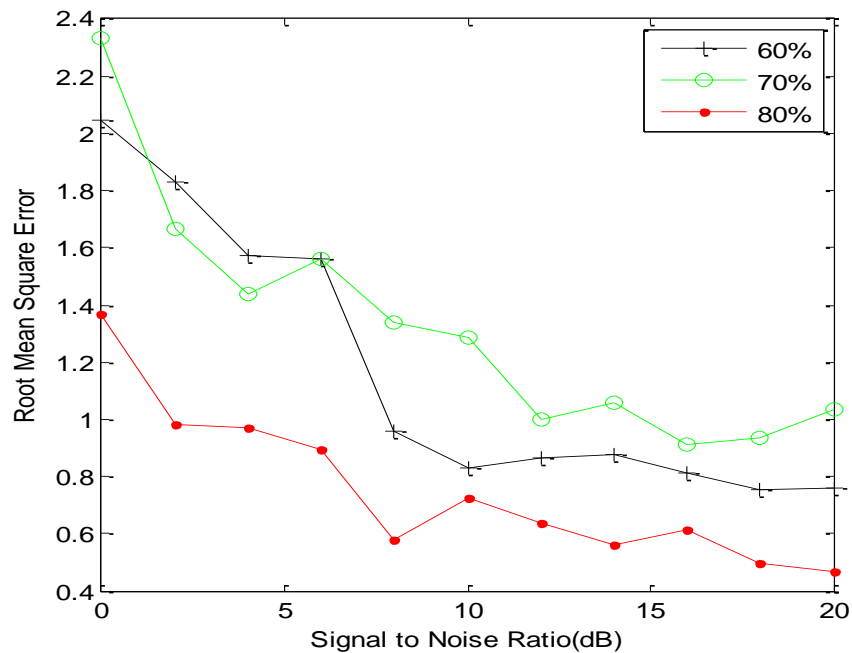


Figure 36 RMS Error Using LASSO Algorithm at Different Number of Samples for Noisy Channel

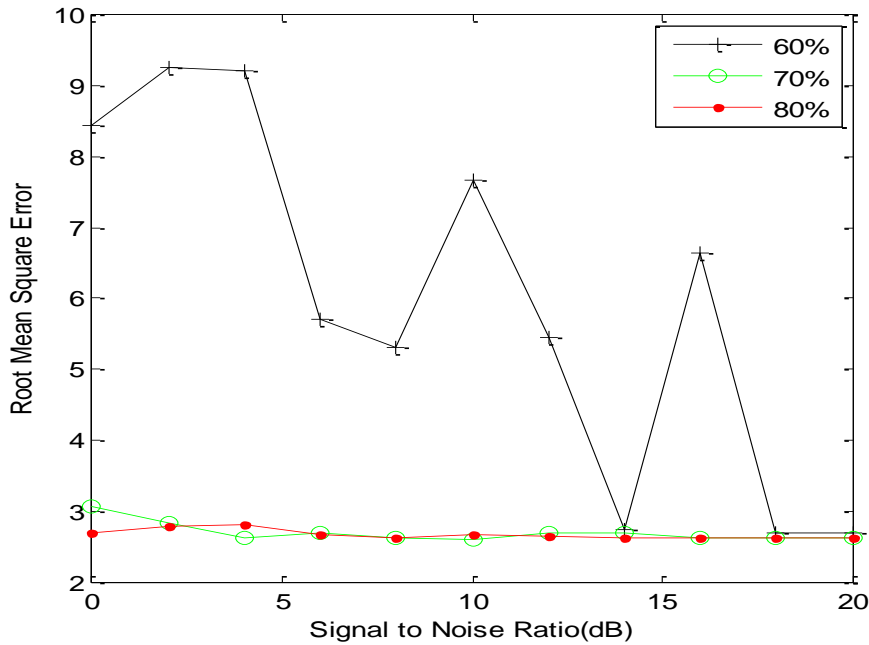


Figure 37 RMS Error Using OMP Algorithm at Different Number of Samples for Noisy Channel

Figures 35 – 37 show how different sample sizes affect the performance of the BP, OMP, and LASSO algorithm. From Figure 37, it can be deduced that OMP performs better with sampling size above 70% as compared to BP and LASSO. It is also noted that as the SNR goes from 0 to 20 dB, the effect of sample size on the reconstruction of the PSD becomes negligible as the RMSE converges. Least Absolute Shrinkage Selective Operator performs better when less than 70% compression ratio is used. The results obtained show that in noisy and Rayleigh fading channels the CS algorithms have different performances. Depending on the environment of CR network the primary user spectrum occupancy can be known and false alarm can be prevented.

Rice Fading Channel

Wireless communication channels experience fading. The fading is caused by reflections, diffractions and scatterings in the channel. The small-scale fading is Rice fading when there is a dominant non fading signal component present, such as a LOS propagation path.

The Rice fading distribution has a probability density function given by

$$p(r) = \begin{cases} \frac{r}{\sigma^2} \exp\left(-\frac{r^2 + A^2}{2\sigma^2}\right) I_0\left(\frac{Ar}{\sigma^2}\right), & r \geq 0 \text{ and } A \geq 0 \\ 0, & r < 0 \end{cases} \quad (39)$$

Where r is the envelope and σ^2 is average of the Rice fading signal. A is the peak amplitude of the dominant signal, and $I_0(\cdot)$ is the modified Bessel function of zero order, which is given by [23]

$$I_0(z) = \sum_{n=0}^{\infty} \frac{z^{2n}}{2^{2n} n! n!} \quad (40)$$

Note that the Rice fading distribution in equation (39) presents two extreme cases:

1. If the dominant signal $A = 0$, $p(r)$ become the Rayleigh fading distribution in equation (35).
2. If the dominant signal A is large, $p(r)$ becomes a Gaussian distribution.

The Rice fading distribution is usually expressed in terms of a parameter K that is defined as the ratio between the deterministic signal power and the variance of the multipath. The parameter is given by

$$k = \frac{A^2}{2\sigma^2}, \quad (41)$$

Or in decibels

$$K = 20 \log \left(\frac{A}{\sqrt{2}\sigma} \right), \quad (42)$$

Where k (or K) is known as the Rice factor that completely specifies the Rice fading distribution. Note that the Rice fading distribution becomes the Rayleigh fading distribution as $A \rightarrow 0$, $K \rightarrow -\infty$ dB.

The Multipath Rice Fading Channel in MatLab is used to model mobile wireless communication systems when the transmitted signal can travel to the receiver along a dominant LOS or direct path. The effects of an AWGN and Rice fading channels on CS based spectrum detection was highlighted and the result obtained for a situation whereby the signal to noise ratio is 10dB and Rice fading K-factor is 10 seconds is shown in Figures 38 to 39.

Comparing the result of Figure 40 and 41 shows that OMP performs better at a higher signal sampling measurement, but the performance deteriorates greatly at a sampling measurement below 70% .This characteristic performance of OMP can be justified theoretically by the fact that OMP is a compressed sensing solver that seeks to compute the minimum ℓ_0 norm solution.

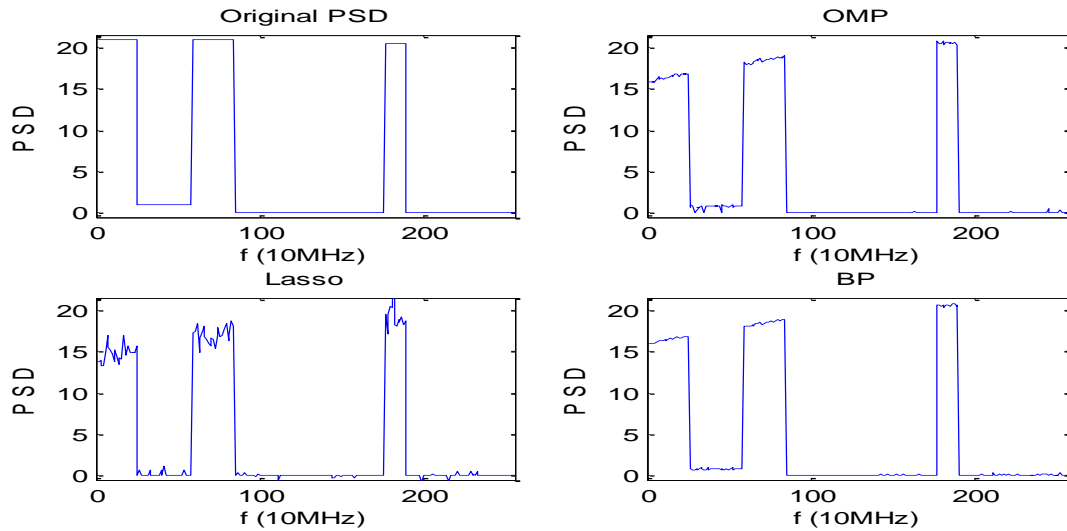


Figure 38 Noisy PSD (Rice fading + Gaussian) at a Compression Ratio of 70%.

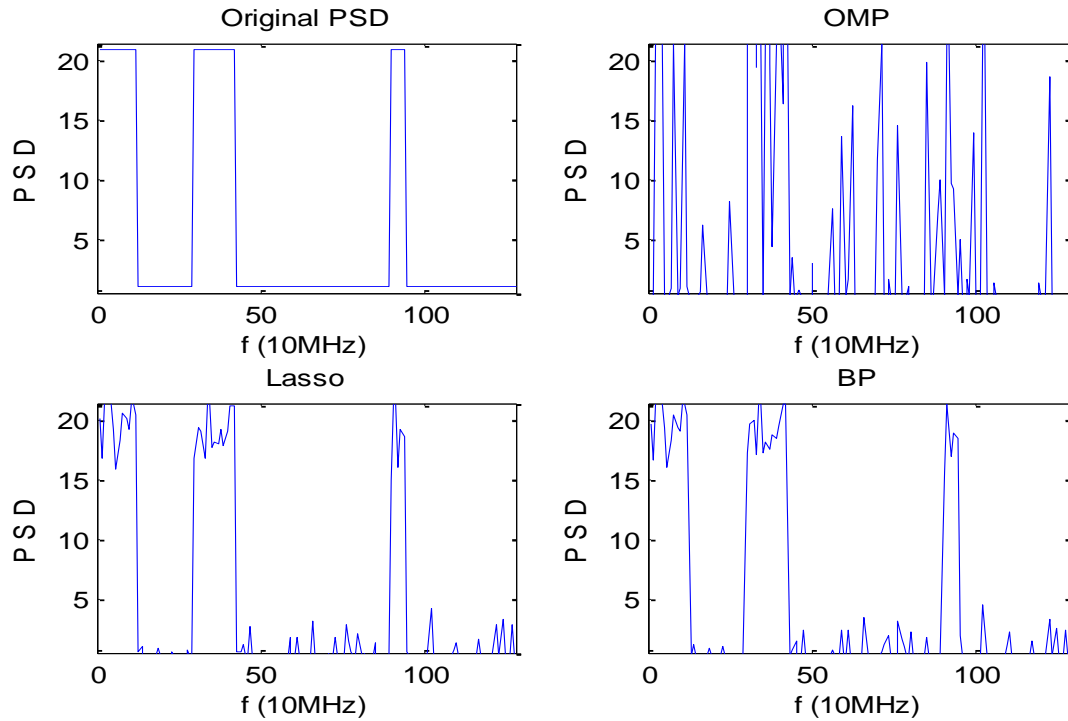


Figure 39 Noisy PSD (Rayleigh Fading Channel + Gaussian) Frequency Responses at a Compression Ratio of 60%.

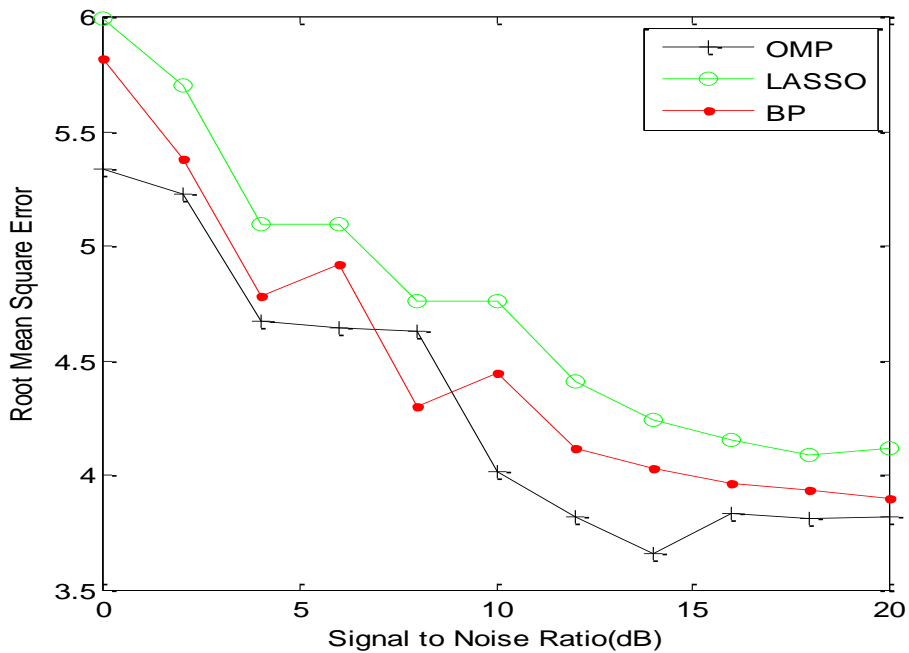


Figure 40 RMS Error Using CS Algorithms of Noisy (Rice Fading+AWGN) PSD (10 dB) at 70% Sampling Measurement

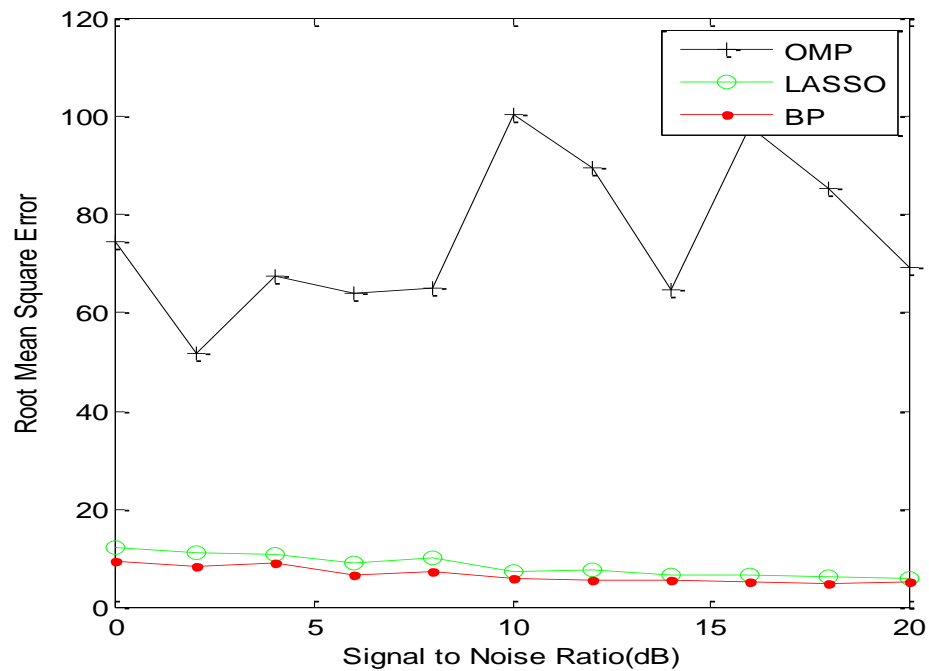


Figure 41 RMS Error Using CS Algorithms of Noisy (Rice fading+AWGN) PSD (10 dB) at 60% Sampling Measurement

A test of the performance of CS reconstruction algorithms for spectrum sensing in a Rice fading environment is accomplished by passing the PSD through Rice fading channel in AWGN channel. The reconstructed PSD is as shown in Figures 2.40 and 2.41.

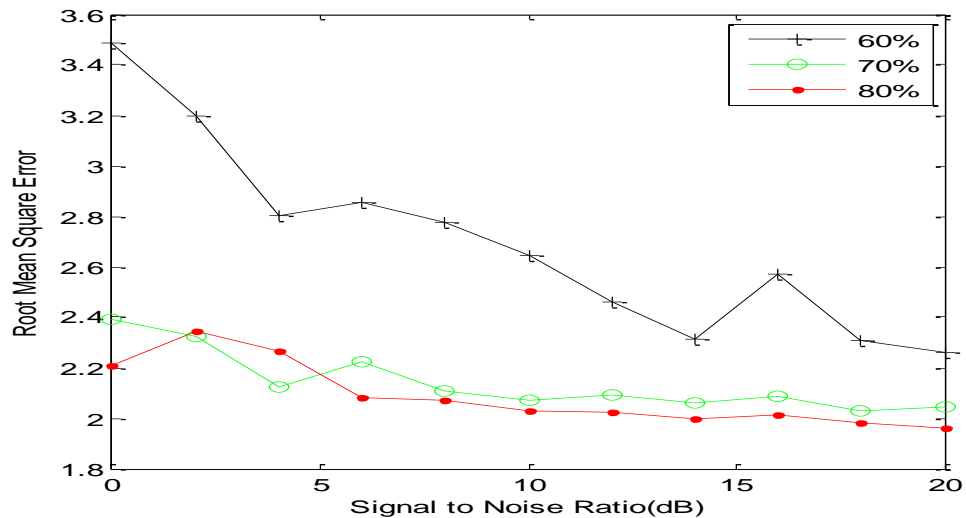


Figure 42 RMS Error Using BP algorithm at Different Number of Samples for Rice Fading plus AWGN Noise

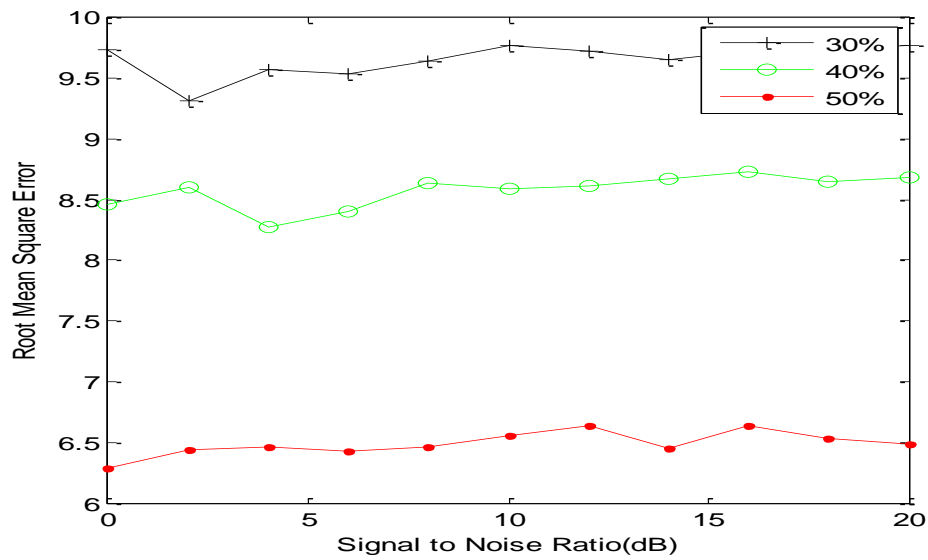


Figure 43 RMS Error Using BP Algorithm at Different Sample Number for Rice Fading plus AWGN Noise

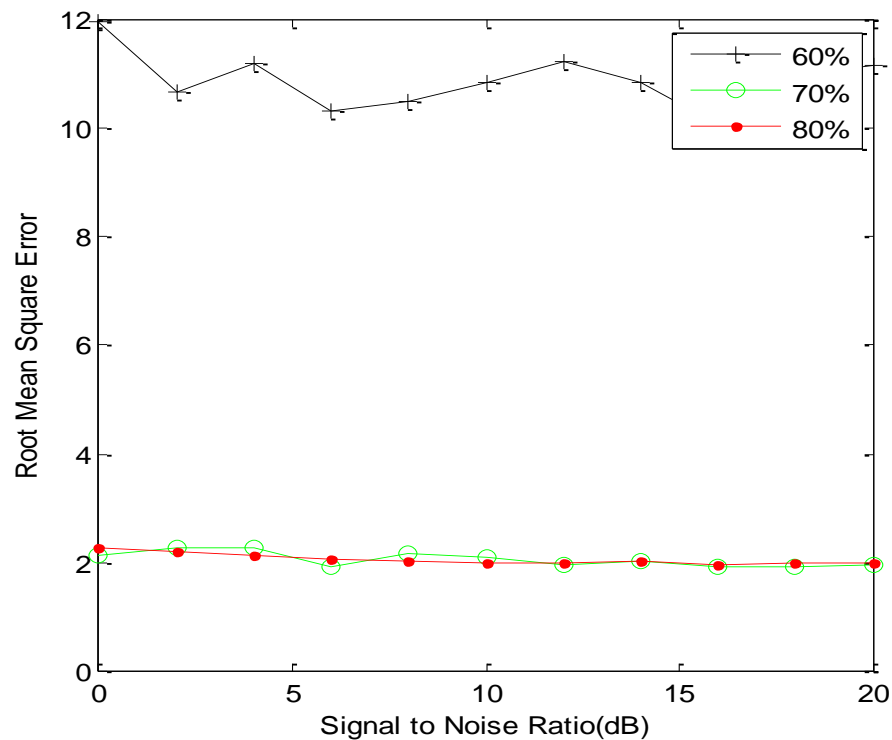


Figure 44 RMS Error Using OMP Algorithm at Different Number of Samples for Rice Fading plus AWGN Noise

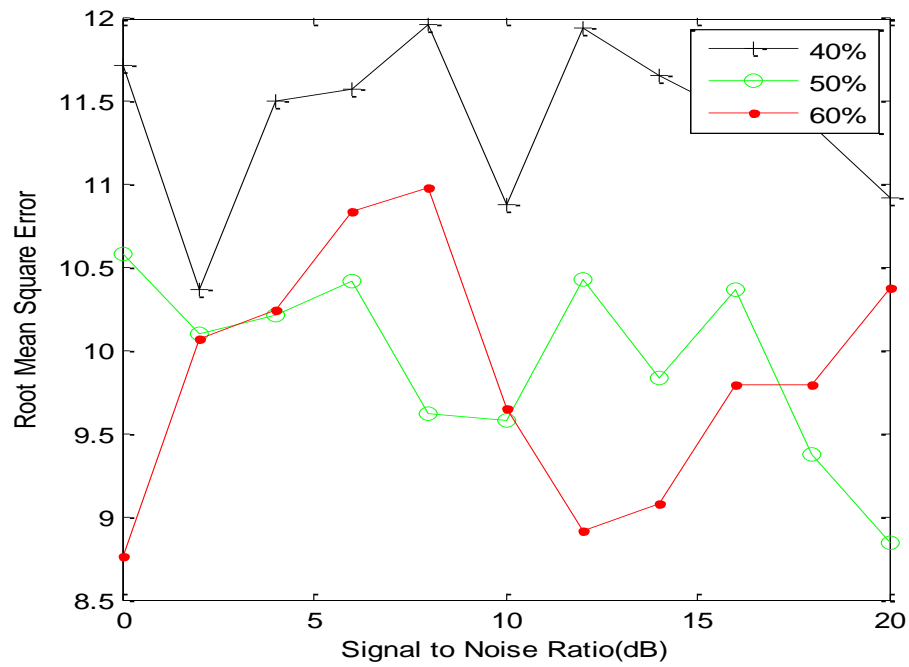


Figure 45 RMS Error Using OMP Algorithm at Different Sample Number for Rice Fading plus AWGN Noise

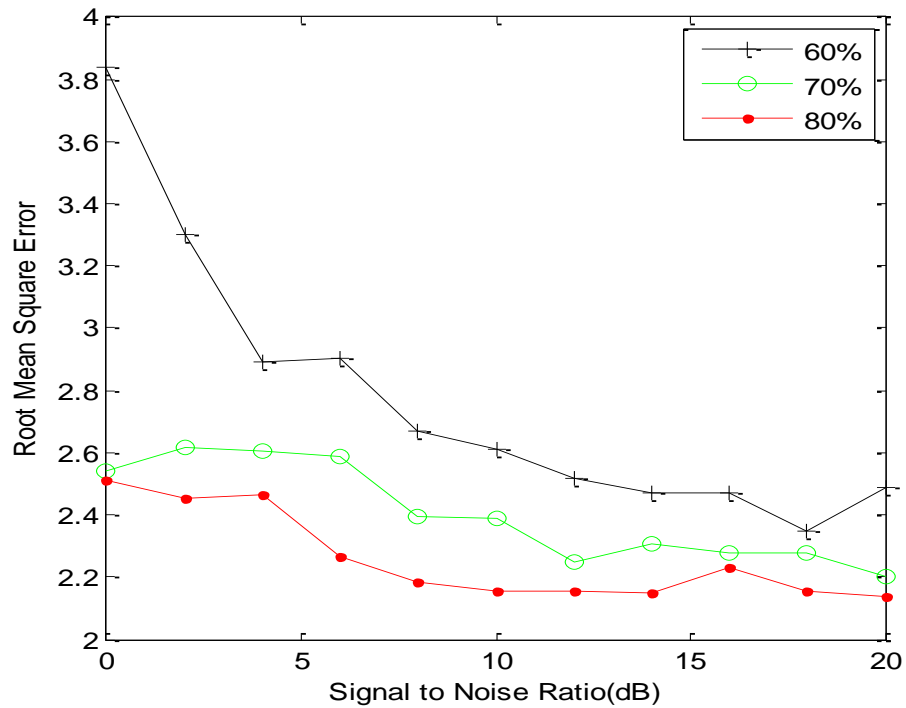


Figure 46 RMS Error Using LASSO Algorithm at Different Number of Samples for Rice fading plus AWGN Noise

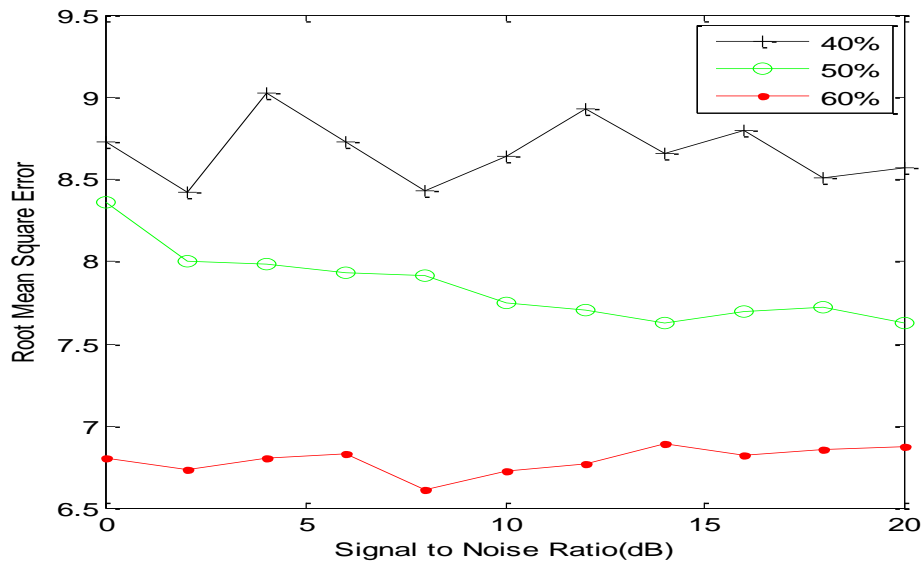


Figure 47 RMS Error Using LASSO Algorithm at Different Sample Number for Rice fading plus AWGN Noise

The characterization result of the RMSE using BP, OMP and LASSO algorithms evaluated at different sampling rates is shown in Figures 40 to 47. Due to the random nature of CS sampling, the recovery procedure is done one hundred times for each sample size of every test. The reconstruction is carried out using BP, OMP and LASSO. Root mean square error of the reconstructed PSD in comparison to the original PSD were computed and used as performance metric.

The results obtained validate the fact that the CS approach to spectrum detection is robust whether in an AWGN channel or a Rice fading channel. Although considerable errors occurs in the magnitude of the characterization based on Rice fading channel plus AWGN in comparison to AWGN channel, this is not necessarily a problem since the goal is to determine the unoccupied frequency band in the spectrum.

Doppler Spread

Due to the relative motion of transmitter and receiver in the CR networks, the Doppler shift is of great practical importance to take account of. The effect of the Doppler shift on the CR network receiver is prevalent. In a dense CR network the phenomenon of Doppler spread in which the spectrum of the transmitted signal is not displaced in the frequency by Doppler shift, but is actually spread out [24].

Doppler spread, D_s is a measure of spectral broadening, f_d caused by the time rate of change of the wideband wireless channel. The Doppler spread is defined as the range of frequencies over the received Doppler power spectrum $S(\nu)$. The components range from $(f_c - f_d)$ to $(f_c + f_d)$, where f_c is the transmitted pure sinusoidal tone of frequency and f_d is the Doppler shift.

The $S(\nu)$ at the CR receiver is then given by

$$S(v) = \begin{cases} \frac{3}{2\pi f_m} \left[1 - \left(\frac{v-f_c}{f_m} \right)^2 \right]^{-\frac{1}{2}}, & |f - f_c| < f_m \\ 0, & \text{otherwise} \end{cases} \quad (43)$$

Where v is the Doppler frequency shift and f_m is the maximum Doppler shift given by

$$f_m = \max(|f_d|) = \max\left(\frac{V}{\lambda} |\cos\theta|\right) = \frac{V}{\lambda}, \quad (44)$$

Where f_d can be either positive or negative depending on the arrival angle θ . V is the relative velocity, and λ is the signal wavelength. Thus, in this case, the Doppler spread is obtained by

$$D_s = f_m \quad (45)$$

The knowledge of the Doppler power spectrum in equation 43 allows the determination of how much spectral broadening is imposed on the signal as a function of the change in the multipath channel state.

Effect of Doppler Shift on CS algorithm Based Spectrum Detection

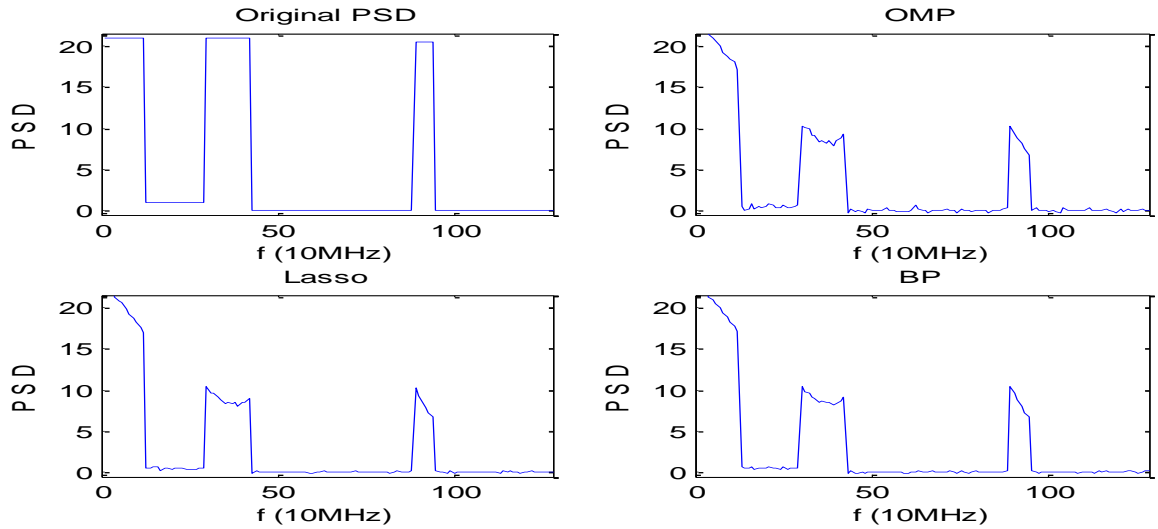


Figure 48 Frequency Responses PSD Passed Through Fading Channel at 150 Max. Doppler Shift

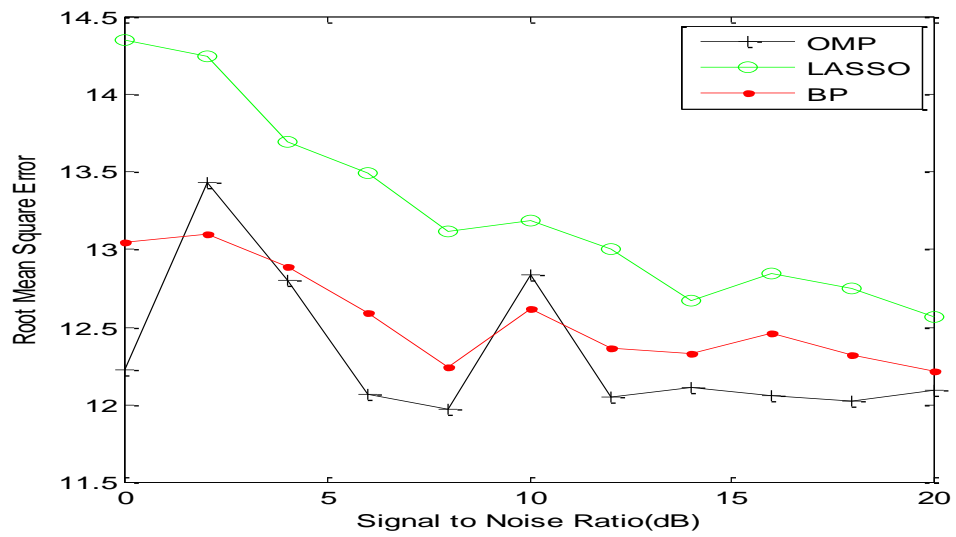


Figure 49 Root Mean Square Error of CS Algorithms in (fading plus AWGN) Environment at 150 Max. Doppler Shift

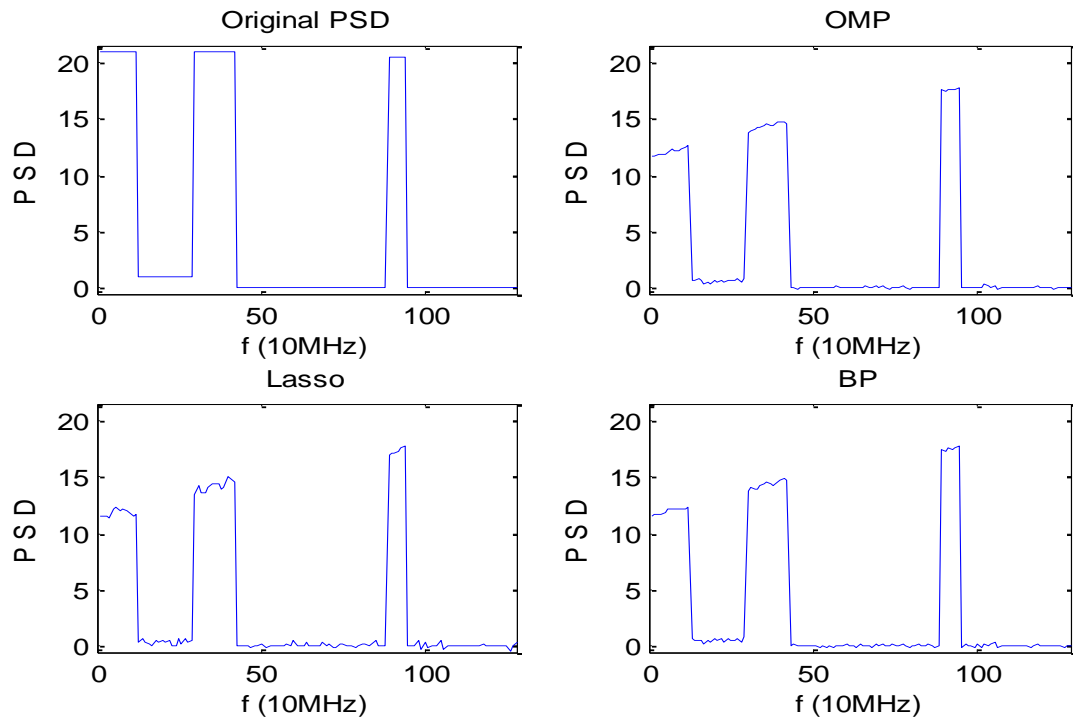


Figure 50 Frequency Response of PSD Passed through Fading Channel at 100 Max. Doppler Shift

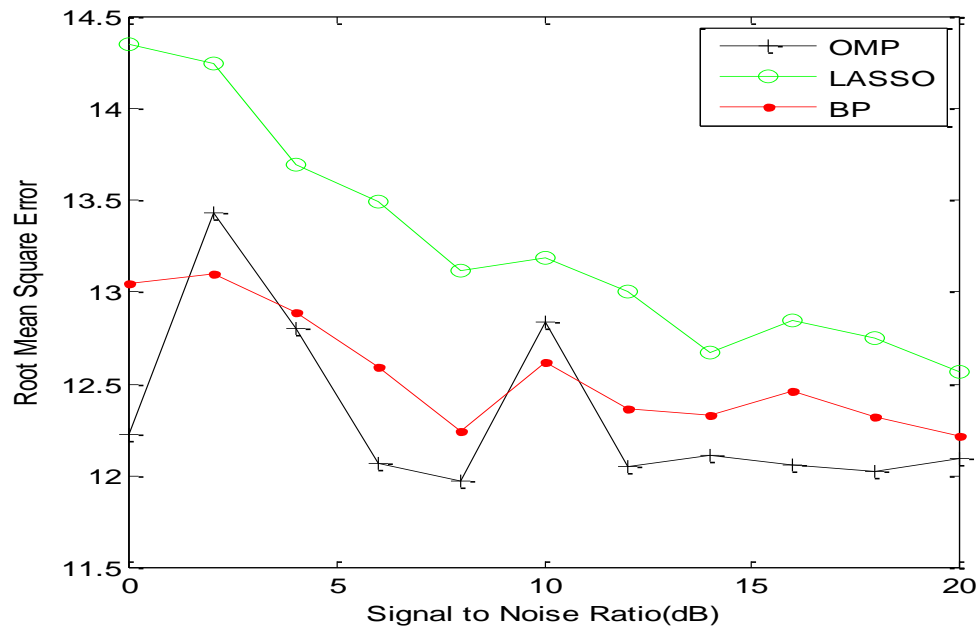


Figure 51 Root Mean Square Error of CS Algorithms in (fading plus AWGN) Environment at 100 Max. Doppler Shift

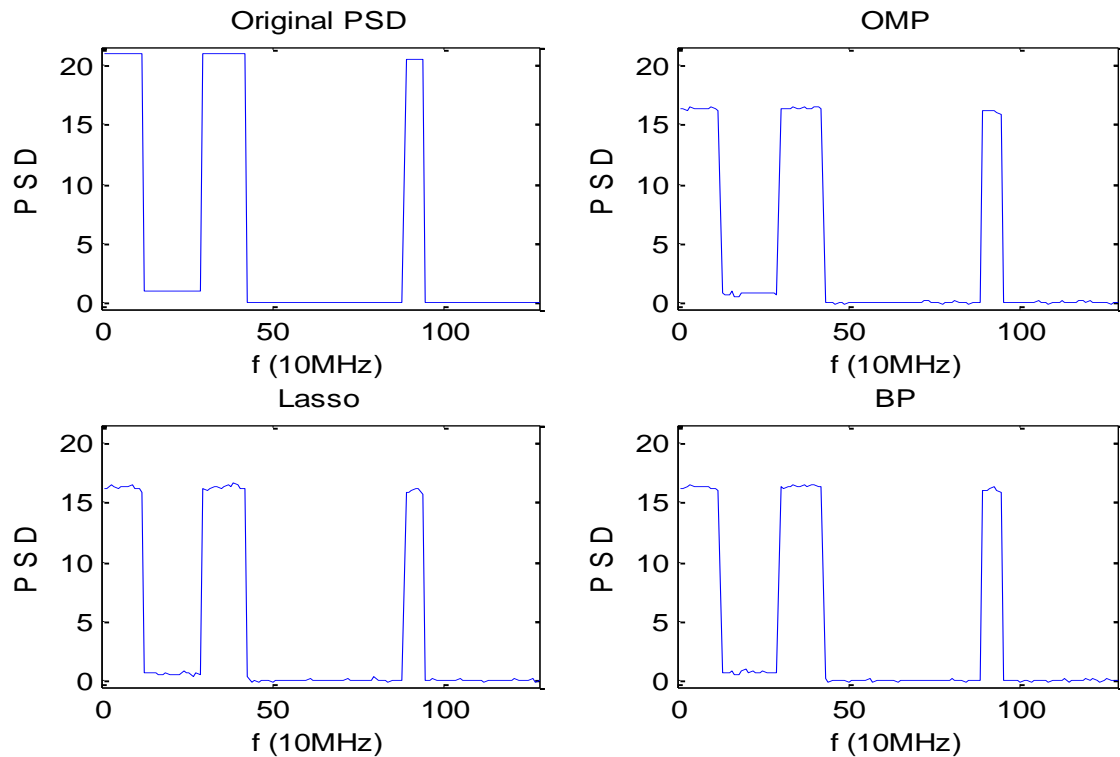


Figure 52 Frequency Response of PSD Passed through Fading Channel at 10 Max. Doppler Shift

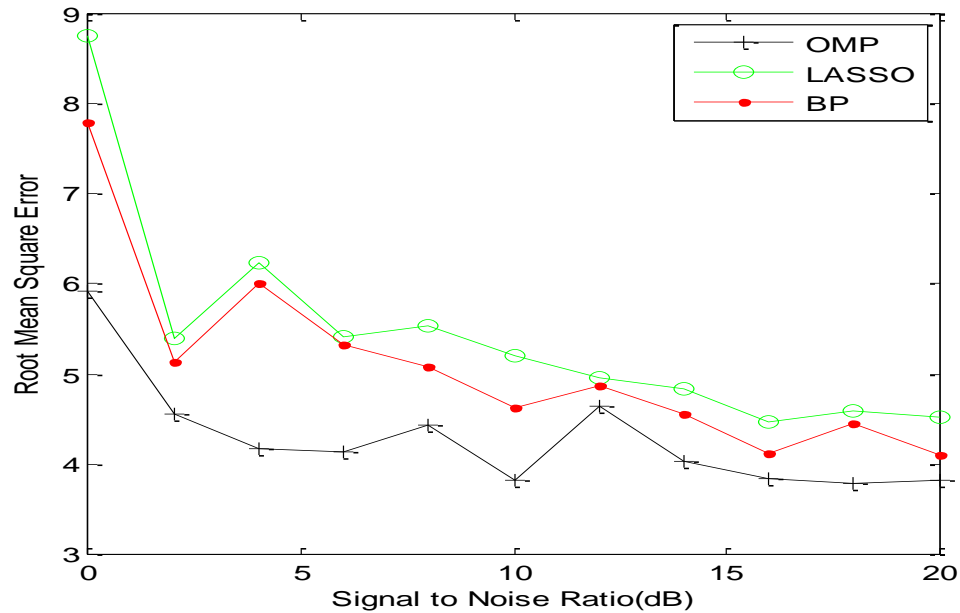


Figure 53 Root Mean Square Error of CS Algorithms in (Fading plus AWGN) Environment at 10 Max. Doppler Shift

Figures 48, 50 and 52 consider the effect of Doppler shift on the system performance at different maximum Doppler shifts. As the Doppler shift increases, the channel varies more rapidly, and thus the system performance becomes worse. One can also see that in the low SNR region, the system performance changes only slightly when using the sinc interpolator which is not related to channel state parameters. The results obtained shows that though LASSO perform worst at 150 and 100 Maximum Doppler shift, the result at 10 maximum Doppler shift for all the three algorithms is relatively close.

However, in the high SNR region ($\text{SNR} > 10 \text{ dB}$) as shown in Figures 49, 51 and 53), the performance changes significantly. The reason for this is for small SNR values, the AWGN is the dominant factor affecting the accuracy of channel estimation. However, in the high SNR region, mismatch of the sinc interpolator with the channel variations become the dominant cause limiting the system performance.

It has been shown that it is possible to determine the available spectrum bandwidth using compressive sampling based signal reconstruction methods. This approach is robust whether in an additive white Gaussian noisy channel or a Rayleigh fading channel. Although significantly error occurs in the magnitude of the characterization based on Rayleigh fading channel plus AWGN in comparison to just AWGN channel, this is not necessarily a problem since the goal is to determine the occupied/unoccupied frequency band in the spectrum. From the results obtained we noticed that the compression ratio has a significant effective on the efficacy of CS algorithms used for dynamic spectrum access. Edge detection algorithms can be employed in determining the unoccupied frequency bands.

3. ERGODIC CAPACITY OF COOPERATIVE AIRBORNE NETWORKS WITH ADAPTIVE SOURCE TRANSMISSION

3.1 Methods, Assumption and Procedures for Efficient Computation of Ergodic Capacity for Cooperative Relay Networks

While the range, capacity, and reliability of a radio link can always be improved by increasing transmit power, this solution is limited by several practical considerations: battery-life, power amplifier size/weight, interference to co-channel and neighboring nodes, and probability-of-intercept requirements, all render this strategy ineffective. An important *modus operandi* to mitigate the deleterious effects of wireless channel impairments is the use of diversity. Although multiple-input-multiple output (MIMO) architectures could drastically improve the range and reliability of beyond line-of-sight and/or over-the-horizon communication links without increasing transmit-power – the cost, weight, and poor aero-dynamics of antenna arrays may prohibit their use on both unmanned vehicles and dismounted tactical war-fighters.

In multi-vehicle cooperative operations, networked nodes in a tight cluster may coordinate both their transmissions and/or receptions to mimic a space-time processing system as if they were part of a single antenna array platform (e.g., [37]-[38]). Thus cooperative airborne networking could significantly increase the range and reliability of a long-haul inter-cluster communication, thereby improving platform endurance with enhanced LPI/LPD capability, without using an antenna array. Several standardization groups such as IEEE 802.16 and IEEE 802.11 have also incorporated cooperative relaying into their emerging wireless standards (e.g., Mobile Multihop Relaying Group has defined a multihop relay architecture in the baseline IEEE 802.16j standard).

Although an intermediate (relay) node in a cooperative airborne network (CAN) may either amplify what it receives (in case of amplify-and-forward relaying) or digitally decodes, and re-encodes the source message (in case of decode-and-forward relaying) before re-transmitting it to the destination node, we shall focus on the amplify-and-forward (analog) relaying scheme in this report because it does not require “sophisticated” transceivers at the relays. Nevertheless, our framework is also applicable for digital relaying once the moment generating function (MGF) of signal-to-noise ratio (SNR) is found. While this protocol can achieve full diversity using a virtual antenna array, there is a loss of spectral efficiency due to its inherent half-duplex operation. But this penalty could be “recovered” to some extent by combining the cooperative diversity with a link adaptation mechanism wherein the power level, signal constellation size, coding rate or other transmission parameters are adapted autonomously in response to fluctuations in the channel conditions. Moreover, fixed transmission methods that are designed to provide the required quality of service in the “worst-case” scenario are very inefficient when better channel conditions prevail.

But the art of adaptive link layer in a CAN is still in its infancy especially when optimized in a cross-layer design paradigm. Majority of the literature on cooperative diversity were limited to both fixed signaling rate and/or constant transmit power for all communication nodes. It is also not very clear as to how link adaptation (e.g., distributed power control) could be performed with limited channel side-information (CSI), and what

are the benefits of jointly optimizing the upper layer protocols with an adaptable PHY layer? For instance, while [39]-[41] have studied the problem of optimal power allocation in a cooperative wireless network, source rate-adaptation [42] was not considered, and more critically its solution requires the knowledge of CSI of all links (i.e., large overhead). Motivated by these observations, [43] derived bounds for the ergodic capacity of a non-regenerative adaptive-link cooperative diversity system with limited CSI, in which the rate and/or power level at the source node is adapted according to the prevailing channel condition (i.e., only the effective SNR at the destination node needs to be feedback to the source node) while the relays simply amplify and forward the signals. Nevertheless, their analysis and results were limited to Rayleigh fading. But in a CAN, it is much more reasonable to model the channel gain of each communication link as a Nakagami-m or a Rice random variable (due to the increased likelihood of the presence of strong specular components in an airborne platform).

Therefore, the main objective of this study is to develop a unified framework based of the MGF method (i.e., since the MGF of the end-to-end SNR is perhaps much easier to compute or may be readily available owing to its widespread use in the outage probability and error rate analysis) for evaluating the ergodic capacity of cooperative analog relaying systems under different adaptive source transmission policies in a myriad of fading environments. Aside from its utility in the assessment of mean achievable transmission rates in an adaptive-link CAN, our development is also interesting because several authors [44]-[46] have recently argued that although the MGF approach has been successfully and extensively applied for evaluating the performance of wireless relaying systems in terms of outage probability and error rates, there have been very limited contributions on ergodic capacity of fading relay channels [44, pp. 2286] (which may be attributed to the difficulty in evaluating the probability density function of the end-to-end SNR in closed-form) or explicitly highlighted the complexity of generalizing the MGF approach for channel capacity computation [45]. In [43], the authors circumvented this difficulty by evaluating upper and lower bounds of the ergodic capacity instead (since its PDF for the Rayleigh fading case can be expressed in closed-form), while [44] resorted to the method of moments (also restricted to Rayleigh channels). In [46], the authors proposed a general method for channel capacity analysis using an integral relation known as E_i -transform, but their solution requires the derivatives of the MGF and/or its auxiliary function, which can be very cumbersome. Moreover, the ergodic capacity formula for the OPRA policy is an approximation while the ergodic capacity for the TCIFR policy was not considered. In this report, we will present two unified yet novel and efficient approaches for evaluating the ergodic capacity of cooperative relay networks: (i) cumulative distribution function (CDF) method – which utilizes the MGF of end-to-end SNR in conjunction with a fixed-Talbot method [47]; (ii) MGF method – which exploits an “exponential-type” integral representation for the logarithm function that facilitates the averaging problem over generalized fading channels.

3.2 System Model

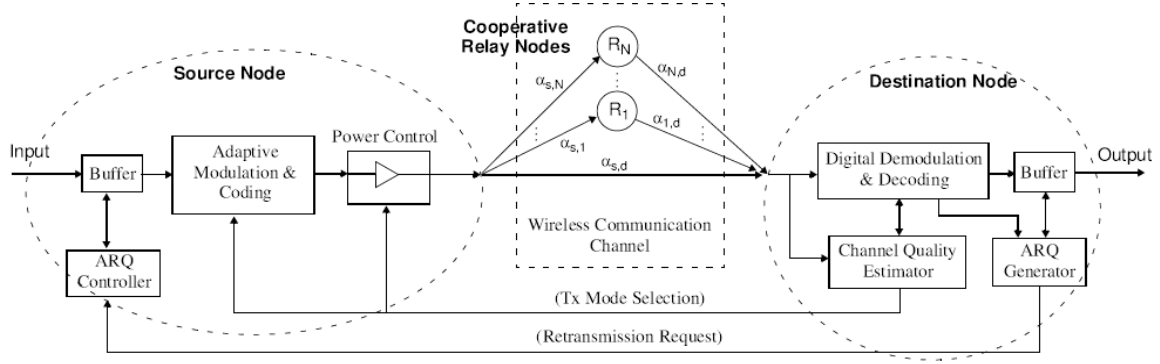


Figure 54: Link-adaptive cooperative diversity system model.

Figure 54 illustrates a cooperative wireless network model. The system model goal is to ensure the connectivity and network stability needed to support varying quality-of-service requirements in an airborne platform. The source node S communicates with destination node D via direct-link and through N amplify-and-forward relays, $R_i, i \in \{1, 2, \dots, N\}$, in two transmission phases. During the initial Phase I, S transmits signal x to D as well as to the relays R_i , where the channel fading coefficients between S and D , S and the i -th relay node R_i , and R_i and D are denoted by $\alpha_{s,d}$, $\alpha_{s,i}$ and $\alpha_{i,d}$, respectively. The received signals at the destination node and i -th relay node are given by

$$y_{s,d} = \sqrt{P_{s,d}} \alpha_{s,d} x + \eta_{s,d} \quad (46)$$

$$y_{s,i} = \sqrt{P_{s,i}} \alpha_{s,i} x + \eta_{s,i} \quad (47)$$

where $P_{s,d} = P_{s,i}$ is the transmitted power at the source, while $\eta_{s,d}$, $\eta_{s,i}$ are the additive noises introduced between source to destination, and source to relay, respectively. During the second phase of cooperation, each of the N relays transmits the received signal after amplification via orthogonal transmissions (e.g., TDMA in a round-robin fashion and/or FDMA). Suppose $P_{i,d}$ is the transmit power of the i -th relay while transmitting its signal to the destination node. The received signal at the destination during the second phase of operation is given by [37]

$$y_{i,d} = G_i \alpha_{i,d} y_{s,i} + \eta_{i,d} = \frac{\sqrt{P_{i,d}}}{\sqrt{P_{s,i} |\alpha_{s,i}|^2 + N_0}} \alpha_{i,d} y_{s,i} + \eta_{i,d} \quad (48)$$

where G_i is the i -th relay amplifier gain, denoted as [1], $G_i = \sqrt{P_{i,d}} / \sqrt{P_{s,i} |\alpha_{s,i}|^2 + N_0}$, $\eta_{i,d}$ is the noise introduced between i -th relay and destination. We further assume that the total transmitted power $P_{s,d} + \sum_{i=1}^N P_{i,d} = P_T$ is fixed. Substituting (47) into (48), we obtain

$$y_{i,d} = \frac{\sqrt{P_{s,i}} \sqrt{P_{i,d}}}{\sqrt{P_{s,i} |\alpha_{s,i}|^2 + N_0}} \alpha_{s,i} \alpha_{i,d} x + \hat{\eta}_{i,d} \quad (49)$$

where $\hat{\eta}_{i,d} = \frac{\sqrt{P_{i,d}}}{\sqrt{P_{s,d}|\alpha_{s,d}|^2 + N_o}}\alpha_{i,d}\eta_{s,i} + \eta_{i,d}$, is a zero-mean complex Gaussian random variable with variance $\left(\frac{P_{i,d}|\alpha_{i,d}|^2}{P_{s,d}|\alpha_{s,d}|^2 + N_o} + 1\right)N_o$ by assuming that $\eta_{s,i}$ and $\eta_{i,d}$ are independent random variables.

Suppose a maximum-ratio combining (MRC) is employed at the destination node to combine all the signals received during Phase I and Phase II, the output of the MRC detector is given by

$$y_T = b_1 y_{s,d} + \sum_{i=1}^N b_i y_{i,d}, \quad (50)$$

where $b_1 = \frac{\sqrt{P_{s,d}}\alpha_{s,d}^*}{N_o}$ and $b_i = \frac{\sqrt{\frac{P_{s,d}P_{i,d}}{P_{s,d}|\alpha_{s,d}|^2 + N_o}}\alpha_{s,d}^*\alpha_{i,d}^*}{\left(\frac{P_{i,d}|\alpha_{i,d}|^2}{P_{s,d}|\alpha_{s,d}|^2 + N_o} + 1\right)N_o}$. Thus the total received SNR can be shown as [1]

$$\gamma_T = \gamma_{s,d} + \sum_{i=1}^N \frac{\gamma_{s,i}\gamma_{i,d}}{1 + \gamma_{s,i} + \gamma_{i,d}} \cong [\gamma_{TB} = \gamma_{s,d} + \sum_{i=1}^N \gamma_i] \quad (51)$$

where $\gamma_{s,i} = |\alpha_{s,i}|^2 P_{s,i} T_s / N_o$ and $\gamma_{i,d} = |\alpha_{i,d}|^2 P_{i,d} T_s / N_o$ denote the instantaneous SNR of the source-relay and relay-destination links, respectively. The approximation on the right-side of (51) is obtained by recognizing that the instantaneous SNR of a two hops path can be accurately estimated to be the harmonic mean of individual link SNRs especially at moderate and high SNR regimes [50]-[51]. Assuming $\gamma_{s,d}$, $\gamma_{s,i}$, $\gamma_{i,d}$ are independent random variables, it is rather straight forward to show that the MGF of γ_{TB} can be evaluated as

$$\phi_\gamma(s) = \phi_{\gamma_{s,d}}(s) \prod_{i=1}^N \phi_{\gamma_i}(s) \quad (52)$$

Note that the MGF of $\gamma_i = \gamma_{s,i}\gamma_{i,d}/(\gamma_{s,i} + \gamma_{i,d})$ in a Rayleigh channel with independent but non-identically distributed (i.n.d) fading statistics well-known, and is given by [50]

$$\phi_{\gamma_i}(s) = \left[(1/\Omega_{s,i} - 1/\Omega_{i,d})^2 + (1/\Omega_{s,i} + 1/\Omega_{i,d})s \right] / \Delta^2 + \frac{2s}{\Delta^3 \Omega_{s,i} \Omega_{i,d}} \ln \left(\left(s + \Delta + \frac{1}{\Omega_{s,i}} + \frac{1}{\Omega_{i,d}} \right)^2 \frac{\Omega_{s,i} \Omega_{i,d}}{4} \right) \quad (53)$$

where $\Omega_{a,b} = E[\gamma_{a,b}]$ corresponds to the mean link SNR and $\Delta = \sqrt{(1/\Omega_{s,i} - 1/\Omega_{i,d})^2 + 2s(1/\Omega_{s,i} + 1/\Omega_{i,d}) + s^2}$. Moreover, the MGF of γ_i in a Nakagami channel with independent identically distributed (i.i.d) fading statistics is given by [51]

$$\phi_{\gamma_i}(s) = {}_2F_1 \left(m, 2m; m + \frac{1}{2}; -\frac{\Omega s}{4m} \right) \quad (54)$$

If a closed-form expression for γ_i is not available (e.g., Nakagami-m or Rice channels with i.n.d fading statistics), but does exist for $\tilde{\gamma}_i = \min(\gamma_{s,i}, \gamma_{i,d})$, we may then resort to the

development of capacity bounds using the inequality used in [43], (i.e., $[\gamma_{LB} = \gamma_{s,d} + \frac{1}{2} \sum_{i=1}^N \tilde{\gamma}_i] \leq \gamma_{TB} \leq [\gamma_{UB} = \gamma_{s,d} + \sum_{i=1}^N \tilde{\gamma}_i]$) viz.,

$$\phi_{\gamma_{s,d}}(s) \prod_{i=1}^N \phi_{\tilde{\gamma}_i}(s) \leq \phi_{\gamma}(s) \leq \phi_{\gamma_{s,d}}(s) \prod_{i=1}^N \phi_{\tilde{\gamma}_i}(s/2) \quad (55)$$

In this case, the MGF of $\tilde{\gamma}_i$ for a 2-hops path may be derived as

$$\phi_{\tilde{\gamma}_i}(s) = \sum_{\substack{k \in \{(s,i),(i,d)\} \\ j \neq k}} \int_0^\infty e^{-sx} f_{\gamma_k}(x) [1 - F_{\gamma_j}(x)] dx \quad (56)$$

For instance, it is not difficult to show that the MGF of $\tilde{\gamma}_i$ in a Nakagami-m channel with i.n.d fading statistics is given by

$$\begin{aligned} \phi_{\tilde{\gamma}_i}(s) = & \sum_{\substack{k \in \{(s,i),(i,d)\} \\ j \neq k}} \frac{\Gamma(m_k + m_j)}{m_k \Gamma(m_k) \Gamma(m_j)} \left(\frac{\Omega_j m_k}{s \Omega_j \Omega_k + \Omega_j m_k + \Omega_k m_j} \right)^{m_k} \\ & \times {}_2F_1 \left(1 - m_j, m_k; 1 + m_k; \frac{(s \Omega_k + m_k) \Omega_j}{s \Omega_j \Omega_k + \Omega_j m_k + \Omega_k m_j} \right) \end{aligned} \quad (57)$$

Once the MGF of γ_i or $\tilde{\gamma}_i$ is found, we can compute the outage probability (i.e., it's CDF) efficiently using a fixed-Talbot (multi-precision Laplace transform inversion) method [47], viz.,

$$F_x(x) \cong \frac{r}{M} \sum_{k=1}^{M-1} \text{Re} \{ e^{xs(\theta_k)} \phi(s(\theta_k)) \frac{1 + j\sigma(\theta_k)}{s(\theta_k)} \} + \frac{1}{2M} \phi_x(r) e^{rx} \quad (58)$$

where $r = 2M/(5x)$, $\sigma(\theta_k) = \theta_k + (\theta_k \cot(\theta_k) - 1) \cot(\theta_k)$, $\theta_k = k\pi/M$, and $s(\theta_k) = r\theta_k(j + \cot(\theta_k))$.

In Section 3.3, it will be shown that the ergodic capacities of ORA, TCIFR, and OPRA source adaptive transmission policies can be expressed in terms of the complementary CDF and/or the MGF of end-to-end SNR alone. Hence the upper limit on bandwidth-normalized link spectral efficiency of cooperative relay networks may be evaluated readily for all of the cases discussed above owing to the availability of the MGF of γ_i or $\tilde{\gamma}_i$ in closed-form. For example, (56) (or (61)), (63) and (66) (or (67)) in conjunction with (55), (57) and (58) generalize the results in [43] to i.n.d Nakagami-m channels. Similarly, precise estimates of the ergodic capacities with different source adaptive transmission techniques in i.n.d Rayleigh fading [or i.i.d Nakagami-m fading] can be obtained by substituting (52) and (53) [or (54) for i.i.d Nakagami-m fading] into (60), (63) and (66).

In Section 3.4, it will be shown that the outage probability can be expressed in terms of CDF. Whereas, achievable spectral efficiency and average bit error rate can be expressed in terms of difference of two CDF terms; and/or MGF, in conjunction with fixed-Talbot method, Once the MGF of γ_i or $\tilde{\gamma}_i$ is available in closed form. For example, (74) in conjunction with (55) and (57); and (64) in conjunction with (52), (53) and (55) generalize the results in [52] for average spectral efficiency of ACR in i.n.d Nakagami-m channels and i.n.d. Rayleigh fading channel respectively. Similarly, accurate estimates of average spectral efficiency of ADR in i.n.d Nakagami-m channels can be obtained by

substituting (76) (by computing CDF terms using the fixed-Talbot method), in to (75), once the MGF is available in closed form. Additionally, average bit error rate can be expressed by substituting (70) in to (67).

3.3 Ergodic Capacity Computation in Fading Channels

The well-known Shannon-Hartley law tells us that there is an absolute limit on the error-free bit rate R that can be transmitted within a certain channel bandwidth B at a specified SNR. This theoretical limit denotes the channel capacity C . Shannon's noisy channel coding theorem also states that, it is not possible to make the probability of error tend to zero if $R > C$ with any code design. Thus, it is clear that the metric C plays an important role in the design or appraisal of any communications system (since it serves as an upper limit on the transmission rate for reliable communications over a noisy communication channel). In this section, we will derive generic expressions for computing the ergodic capacity of cooperative relay networks with different adaptive source transmission techniques.

3.3.1 Optimal Rate Adaptation with Fixed Transmit Power (ORA)

When only the rate is adapted by changing channel conditions, the ergodic capacity is given by

$$\frac{\bar{C}_{ORA}}{B} = \frac{1}{N+1} \frac{1}{\ln 2} \int_0^\infty \ln(1+\gamma) f_\gamma(\gamma) d\gamma \quad (59)$$

Utilizing the “exponential-type” integral representation of $\ln(\gamma+1)$ (see Appendix A), we can facilitate the averaging problem in (48) given that $\phi_\gamma(\cdot)$ is available in closed form. Substituting (A.5) into (48), we obtain the ergodic capacity in terms of the MGF of γ alone, viz.,

$$\begin{aligned} \frac{\bar{C}_{ORA}}{B} &= \frac{1}{N+1} \frac{1}{\ln 2} \int_0^\infty \frac{e^{-2x}}{x} \left[\int_0^\infty (1-e^{-2xy}) f_\gamma(\gamma) d\gamma \right] dx \\ &= \frac{1}{N+1} \frac{1}{\ln 2} \int_0^\infty \frac{e^{-2x}}{x} [1 - \phi_\gamma(2x)] dx \\ &= \frac{1}{N+1} \frac{1}{\ln 2} \int_0^\infty \frac{e^{-y}}{y} [1 - \phi_\gamma(y)] dy \end{aligned} \quad (60)$$

Alternatively, using integration by parts (with $u = \ln(1+\gamma)$, $dv = f_\gamma(\gamma) d\gamma$ and $v = -\int_x^\infty f_\gamma(\gamma) d\gamma$), (48) can be expressed in terms of CDF of γ as

$$\frac{\bar{C}_{ORA}}{B} = \frac{1}{N+1} \frac{1}{\ln 2} \int_0^\infty \frac{F_\gamma^c(x)}{1+x} dx \quad (61)$$

where $F_\gamma^c(x) = 1 - F_\gamma(x) = \int_x^\infty f_\gamma(\gamma) d\gamma$ is the complementary CDF of γ .

It is also interesting to note that the new forms (49) and (50) allow us to show that the ergodic capacity of a point-to-point link increases with the increasing receiver diversity order regardless of the fading channel model or diversity combining technique employed. Gunther [49, pp. 401] suggested that while this is intuitive, it not easy to prove this trend mathematically for the ORA adaptation policy. However, recognizing that the CDF $F_\gamma(\gamma)$ will decrease with increasing order of receiver diversity for any given γ , the

numerator term $F_\gamma^c(x)$ in (61) will be much closer to unity in comparison with that of no-diversity or lower diversity order cases. Thus, we have shown that the capacity increases with diversity order as expected. Similarly, since $\phi_\gamma(s)$ is a monotonically decreasing function with respect to its argument and $0 \leq \phi_\gamma(s) \leq 1$, the term $1 - \phi_\gamma(y)$ in (60) approaches to much closer to unity as receiver diversity order increases.

3.3.2 Channel Inversion with Fixed Rate (CIFR)

In CIFR policy, the transmitter adapts its power to maintain a constant SNR at the receiver and uses fixed-rate modulation and fixed-code designs. This technique is the least complex to implement given that reliable channel estimates are available at the transmitter. However, when the channel experiences deep fades, the penalty in transmit power requirement with the CIFR policy will be enormous because channel inversion needs to compensate for the deep fades. To overcome this, a truncated channel inversion and fixed rate policy (TCIFR) was considered in [42] where the channel fading is only inverted above a fixed cutoff fade depth γ_0 . The data transmission is ceased if γ falls below γ_0 . In this case, it is easy to show that the outage probability is $P_{out} = F_\gamma(\gamma_0)$ and the ergodic channel capacity is given by

$$\frac{\bar{C}_{TCIFR}}{B} = \frac{1}{N+1} \log_2 \left(1 + \frac{1}{\int_{\gamma_0}^{\infty} \gamma^{-1} f_\gamma(\gamma) d\gamma} \right) F_\gamma^c(\gamma_0) \quad (62)$$

Substituting $f_\gamma(\gamma) = \frac{1}{\pi} \int_0^\infty \text{Re}\{\phi_\gamma(-j\omega) e^{-j\omega\gamma}\} d\omega$ (i.e., inverse Fourier transform of the characteristic function) in (51), we obtain (see details in Appendix B)

$$\frac{\bar{C}_{TCIFR}}{B} = \frac{1}{N+1} \log_2 \left(1 - \frac{1}{\nabla} \right) F_\gamma^c(\gamma_0) \quad (63)$$

where $\nabla = \frac{1}{\pi} \int_0^\infty \text{Re}\{\phi_\gamma(-j\omega) Ei(-j\omega\gamma_0)\} d\omega$ while the exponential integral $Ei(-jc) = -\int_1^\infty \frac{e^{-jt}}{t} dt$ can be evaluated in MATLAB using command line “`cosint(c) - j(-pi/2 + sinint(c))`”. Observe that, if the MGF of γ is known in closed-form, then the above integral can be evaluated efficiently via Gauss-Chebyshev quadrature method for a wide-range of fading channel models and diversity combining techniques employed (including maximal-ratio combining and selection diversity). The zero-outage ergodic capacity (i.e., CIFR policy) can be evaluated by setting $\gamma_0 = 0$ in (63).

3.3.3 Optimal Power and Rate Adaptation (OPRA)

In the OPRA strategy, both the transmission power and rate are matched to the varying channel condition through use of a multiplexed multiple codebook design. This leads to the highest achievable capacity with CSI. From [42], we have

$$\frac{\bar{C}_{OPRA}}{B} = \frac{1}{N+1} \frac{1}{\ln 2} \int_{\gamma_0}^{\infty} \ln \left(\frac{\gamma}{\gamma_0} \right) f_\gamma(\gamma) d\gamma \quad (64)$$

where γ_0 is the optimal cut-off SNR below which the data transmission is suspended. Substituting (A.4) into (53), and by re-arranging the integral terms, we obtain

$$\begin{aligned}\frac{\bar{C}_{OPRA}}{B} &= \frac{1}{N+1} \frac{1}{\ln 2} \int_0^\infty \frac{1}{x} \left[e^{-2x} \int_{\gamma_0}^\infty f_\gamma(\gamma) d\gamma - \int_{\gamma_0}^\infty e^{-\frac{2x\gamma}{\gamma_0}} f_\gamma(\gamma) d\gamma \right] dx \\ &= \frac{1}{N+1} \frac{1}{\ln 2} \int_0^\infty \frac{1}{x} \left[e^{-2x} [1 - F_\gamma(\gamma_0)] - \phi_\gamma(2x/\gamma_0, \gamma_0) \right] dx\end{aligned}\quad (65)$$

because $\int_{\gamma_0}^\infty f_\gamma(\gamma) d\gamma = 1 - F_\gamma(\gamma_0) = F_\gamma^c(\gamma_0)$ and $\int_{\gamma_0}^\infty e^{-\frac{2x\gamma}{\gamma_0}} f_\gamma(\gamma) d\gamma = \phi_\gamma(2x/\gamma_0, \gamma_0)$ denotes the marginal MGF. Since the desired marginal MGF is typically not available in closed-form, we circumvent this difficulty by computing this term via the ‘‘CDF’’ of an auxiliary function with a fixed-Talbot method (details shown in Appendix C), viz.,

$$\frac{\bar{C}_{OPRA}}{B} = \frac{1}{N+1} \frac{1}{\ln 2} \int_0^\infty \frac{1}{x} \left[e^{-2x} [1 - F_\gamma(\gamma_0)] - \phi_\gamma\left(\frac{2x}{\gamma_0}\right) + F_{\hat{\gamma}}(\gamma_0) \right] dx \quad (66)$$

If $\phi_\gamma(2x/\gamma_0)$ is available in the closed form, then the terms $F_\gamma(\gamma_0)$ and $F_{\hat{\gamma}}(\gamma_0)$ in (66) can be computed efficiently using the fixed-Talbot method (see (58)).

Alternatively, (64) can be concisely expressed in terms of the CDF of γ (using integration by parts with $u = \ln(\gamma)$ and $v = -\int_{\gamma_0}^\infty f_\gamma(x) dx$) (64) as

$$\frac{\bar{C}_{OPRA}}{B} = \frac{1}{N+1} \frac{1}{\ln 2} \int_1^\infty \frac{F_\gamma^c(\gamma_0 \gamma)}{\gamma} d\gamma. \quad (67)$$

To achieve the capacity (66) or (67), the channel fade level (i.e., CSI) tracked at the receiver must be conveyed to the transmitter on the feedback path for power and rate adaptation in accordance with the time-varying nature of the channel fading. When $\gamma < \gamma_0$, no data is transmitted, and thus the optimal policy suffers an outage probability given by $P_{out} = F_\gamma(\gamma_0)$, which equals to the probability of no transmission. The optimal cutoff SNR must satisfy

$$F_\gamma^c(\gamma_0) - \gamma_0 \left[1 + \int_{\gamma_0}^\infty \gamma^{-1} f_\gamma(\gamma) d\gamma \right] = 0 \quad (68)$$

The integral term in (34) can be evaluated efficiently similar to the development of (63) when the MGF is available. Furthermore, asymptotic analysis of (68) shows that $\gamma_0 \rightarrow 0$ when the mean SNR $\Omega \rightarrow 0$ because $F_\gamma(x) \rightarrow 1$ and $f_\gamma(x) \rightarrow 0$ (i.e., the effect of $\Omega \rightarrow 0$ can be predicted from the normalized PDF or the normalized CDF curve when its argument $x \rightarrow \infty$). When $\Omega \rightarrow \infty$, $F_\gamma(x) \rightarrow 0$ because this is equivalent to computing the CDF when its argument $x \rightarrow 0$. It is also well-known that $\phi_\gamma(\cdot) \rightarrow 0$ as $\Omega \rightarrow \infty$. Hence, $\gamma_0 \rightarrow 1$ as $\Omega \rightarrow \infty$. Thus γ_0 (can be determined by solving (68) numerically) always lies in the interval $[0, 1]$ regardless of the assumption on the fading channel model or the number of relay nodes employed.

3.4 Adaptive M-QAM Modulation

3.4.1 Adaptive Scheme

It has already been proved that optimal rate-fixed power adaptation policy has numerous practical advantages, in addition to other adaptive transmission schemes. Adaptive QAM method is commonly used to enhance the link spectral efficiency of system, by satisfying a certain required BER performance [53]-[56]; and in [53] the authors nicely propose and analyze a variable-rate variable power M-QAM for fading channels. By considering above facts, adaptive M -QAM is considered in this paper. The equation of bit error rate (BER) of a system, which incorporate M -QAM modulation over an Additive White Gaussian Noise (AWGN) channel, with coherent detection; and Gray coding can be represented as [53], [56]

$$BER(M_n, \gamma) \approx 0.2 \exp\left(\frac{3\gamma}{2(M-1)}\right) \quad (69)$$

where γ is the received SNR. As from [53], [56], (69) provide closed-form solution for further analysis, and it is invertible. By inverting (69), the spectral efficiency of the continuous-rate M -QAM can be approximated as [53], [56]:

$$\frac{R}{W} = \log_2 M = \log_2 \left(1 + \frac{3\gamma}{2K_0}\right) \quad (70)$$

where $K_0 = -\ln(5BER_0)$ and BER_0 represents the target BER.

We can effectively compute the spectral efficiently of Adaptive Continuous Rate M-QAM using (59). However, compared to ACR M-QAM, ADR M-QAM; in which the constellation size is limited to 2^n (where n is positive integer), is more realistic approach.

In ADR M -QAM, The range of the effective received SNR is divided into $T+1$ fading regions. In each region, a specific constellation of size M_n is used. A particular constellation, of size M_n is decided at the receiver, based on the overall total received SNR, when the fading causes the effective SNR to fall into the n th region ($n = 0, 1, \dots, T$). The partitioning of the effective received SNR depends on the desired BER level BER_0 and to reach a specific BER target of BER_0 , by using M_n -QAM; region boundaries are selected to the following range of SNR, to accomplish desired performance [56]:

$$\begin{aligned} \gamma_1 &= [erfc^{-1}(2BER_0)]^2, \\ \gamma_n &= \frac{2}{3} K_0 (2^n - 1); \quad n = 0, 2, 3, \dots, T, \\ \gamma_{T+1} &= +\infty \end{aligned} \quad (71)$$

where $erfc^{-1}()$ is the inverse complementary error function.

B. Probability of Outage

When $\gamma < \gamma_1$, no data is transmitted, and thus the optimal policy suffers an outage probability, given by $P_{out} = F_\gamma(\gamma_1)$ where,

$$F_{\gamma}(\gamma_1) = LT^{-1} \left[\frac{1}{s} \phi_{\gamma_{s,d}}(s) \prod_{i=1}^N \phi_{\gamma_i}(s) \right] \quad (72)$$

where γ_1 is the optimal cutoff SNR level, below which data transmission is suspended. Once the MGF of γ_i or $\tilde{\gamma}_i$ is found, we can compute the outage probability (i.e., it's CDF) efficiently using a fixed-Talbot (multi-precision Laplace transform inversion) method [47] (see (47)).

C. Achievable Spectral Efficiency

The average spectral efficiency for ACR is calculated by integrating (59) over the PDF of the received SNR [52].

$$\frac{R_{acr}}{B} = \frac{1}{N+1} \frac{1}{\ln 2} \int_0^{\infty} \ln \left(1 + \frac{3\gamma}{2K_0} \right) f_{\gamma}(\gamma) d\gamma \quad (73)$$

Utilizing the “exponential type” integral representation “of $\ln \left(1 + \frac{3\gamma}{2K_0} \right)$ ” (see Appendix A), we can efficiently compute achievable spectral efficiency given that, $\phi_{\gamma}(\cdot)$ is available in closed form. Substituting (A.5) into (52), we obtain the average spectral efficiency in terms of MGF of γ alone, viz.,

$$\begin{aligned} \frac{R_{acr}}{B} &= \frac{1}{N+1} \frac{1}{\ln 2} \int_0^{\infty} \frac{e^{-2x}}{x} \left[\int_0^{\infty} (1 - e^{-2\left(\frac{1.5}{K_0}\right)xy}) f_{\gamma}(\gamma) d\gamma \right] dx \\ &= \frac{1}{N+1} \frac{1}{\ln 2} \int_0^{\infty} \frac{e^{-2x}}{x} \left[1 - \phi_{\gamma} \left\{ 2 \left(\frac{1.5}{K_0} \right) x \right\} \right] dx \\ &= \frac{1}{N+1} \frac{1}{\ln 2} \int_0^{\infty} \frac{e^{-y}}{y} \left[1 - \phi_{\gamma} \left\{ y \left(\frac{1.5}{K_0} \right) \right\} \right] dy \end{aligned} \quad (74)$$

In comparison to achievable spectral efficiency of ACR, the achievable spectral efficiency of ADR is defined as the sum of data rates in each of the partition regions, weighted by the probability of occurrence of each region, and is given by [52],

$$\frac{R_{adr}}{B} = \frac{1}{N+1} \sum_{n=1}^T n p_n \quad (75)$$

where $n = \log_2(M_n)$ corresponds to the data rate of the n th region, p_n is denoted as the probability of occurrence that the effective received SNR, γ is in the n th partition region and is given as [16],

$$p_n = \int_{\gamma_n}^{\gamma_{n+1}} f_{\gamma}(\gamma) d\gamma = F_{\gamma}(\gamma_{n+1}) - F_{\gamma}(\gamma_n) \quad (76)$$

Here, the MGF of random variable γ is available and by (47), Abate's fixed Talbot method (multi-precision Laplace inversion formula) [47], we can efficiently evaluate the CDF terms $F_{\gamma}(\gamma_{n+1})$ and $F_{\gamma}(\gamma_n)$.

D. Average Bit Error Rate

The analysis of BER_{acr} is insignificant, because the value of ACR M -QAM constantly approaches the desired BER target. However, in the case of ADR M -QAM, the received SNR is divided in to discrete partitions, results in a conservative average BER. This limits the average BER_{adr} to be always smaller than the target BER. The average BER_{adr} can be approximated as [52],

$$BER_{adr} = \frac{\sum_{n=1}^T n \overline{BER}_n}{\sum_{n=1}^T n p_n} \quad (77)$$

$$\text{where } \overline{BER}_n = \int_{\gamma_n}^{\gamma_{n+1}} BER(M_n, \gamma) f_{\gamma}(\gamma) d\gamma \quad (78)$$

by substituting (14) in (23) we get,

$$\begin{aligned} \overline{BER}_n &= \int_{\gamma_n}^{\gamma_{n+1}} 0.2 \exp\left(\frac{3\gamma}{2(M-1)}\right) f_{\gamma}(\gamma) d\gamma \\ &= 0.2 \left[\int_{\gamma_n}^{\infty} \exp\left(\frac{3\gamma}{2(M-1)}\right) f_{\gamma}(\gamma) d\gamma - \int_{\gamma_{n+1}}^{\infty} \exp\left(\frac{3\gamma}{2(M-1)}\right) f_{\gamma}(\gamma) d\gamma \right] \end{aligned} \quad (79)$$

where, $f_{\hat{\gamma}}(x) = a_n \exp(-\beta x) f_{\gamma}(x)$ is an auxiliary function, in which $\beta = \frac{3}{2(M-1)}$ and

$$a_n = 0.2.$$

By using (C.1) (see Appendix C), we can re-write (45) in terms of marginal MGF, and subsequently in terms CDF as follows,

$$\begin{aligned} \overline{BER}_n &= 0.2 \{ \phi_{\gamma}(\beta, \gamma_n) - \phi_{\gamma}(\beta, \gamma_{n+1}) \} \\ &= 0.2 \left\{ \left(F_{\hat{\gamma}}(\infty) - F_{\hat{\gamma}}(\gamma_n) \right) - \left(F_{\hat{\gamma}}(\infty) - F_{\hat{\gamma}}(\gamma_{n+1}) \right) \right\} \\ &= 0.2 \left\{ F_{\hat{\gamma}}(\gamma_{n+1}) - F_{\hat{\gamma}}(\gamma_n) \right\} \end{aligned} \quad (80)$$

Here, the MGF of new random variable $\hat{\gamma}$ is available and by using (C.2), in conjunction with (58) Abate's fixed Talbot method (multi-precision Laplace inversion formula) [47], we can efficiently evaluate the CDF terms $F_{\hat{\gamma}}(\gamma_{n+1})$ and $F_{\hat{\gamma}}(\gamma_n)$.

Finally, using (76) and (80), in to (77), we can efficiently compute the average BER_{adr} .

3.5 Results and Discussions of Ergodic Capacity of Cooperative Networks

3.5.1 Ergodic Capacity of Cooperative Relay Networks

In this sub-section, selected numerical results will be presented for the ergodic capacities of cooperative analog relaying systems under different source adaptive transmission policies. The following mean link SNRs (arbitrarily chosen) will be used to generate the plots, unless stated otherwise: $\Omega_{s,1} = E_s/N_0$, $\Omega_{s,2} = 0.5E_s/N_0$, $\Omega_{1,d} = 0.5E_s/N_0$, $\Omega_{2,d} = E_s/N_0$, and $\Omega_{s,d} = 0.2E_s/N_0$.

Figure 55 depicts the comparison of ergodic capacities of three distinct source adaptive transmission policies in an i.n.d Rayleigh channel with two cooperative relays. As anticipated, there is no significant difference observed in the ergodic capacities of OPRA

and ORA at high SNRs. But the ergodic capacity of TCIFR policy (plotted for the cut-off SNR $\gamma_0 = 6$ dB) is considerably lower than the OPRA scheme. Although not shown in this figure, we also noticed that the curves corresponding to the “tight approximation” case (i.e., $\gamma_{TB} = \gamma_{s,d} + \sum_{i=1}^N \gamma_i$) are in good agreement with the Monte Carlo simulation results.

Moreover, the actual ergodic capacity is slightly closer to the lower bound (rather than the upper bound) at low SNRs. Although the authors in [43] have studied the channel capacities of cooperative relaying system in i.n.d Rayleigh channel, but their framework does not lend itself to the analysis of the “tight approximation” case or generalize to other fading channels, whereas our framework encapsulates all these cases in an unified way.

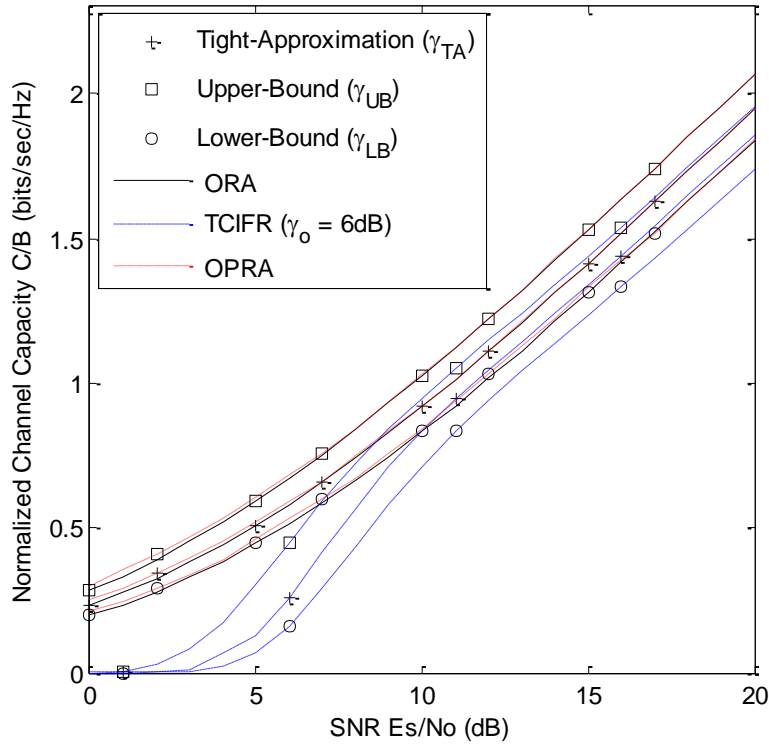


Figure 55 Ergodic capacities of ORA, OPRA and TCIFR policies in an i.n.d Rayleigh channel (N = 2).

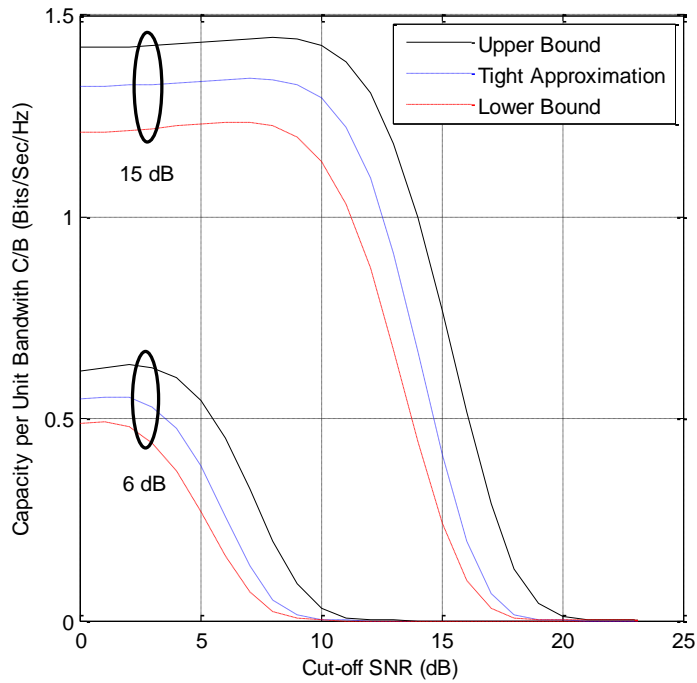


Figure 56 Ergodic capacity of TCIFR versus cut-off SNR (γ_0) in an i.n.d Rayleigh channel (N=2).

Figure 56 depicts the ergodic capacities of TCIFR scheme for $E_s/N_0 = 6\text{dB}$ and $E_s/N_0 = 15\text{dB}$ as a function of cut-off SNR (γ_0) in an i.n.d Rayleigh channel with two relays. It is evident that there exists an optimal choice for the cut-off SNR which maximizes the channel capacity when E_s/N_0 is fixed. But it should be also emphasized that the selection of γ_0 will directly affect the outage probability (i.e., probability of no transmission) of the TCIFR policy.

Figure 57 shows the ergodic capacities (i.e., for the “tight-approximation” case) for different source adaptive transmission schemes over i.i.d Nakagami- m channels (fading severity index $m = 0.5, 1, 1.5$ and 2). It is observed that the ergodic capacity increases with the increasing value of m (i.e., as channel experiences less severe fading) for all source adaptive transmission schemes. However, the gap between the curves corresponding to the ORA and OPRA policies widens as m decreases, although their achievable normalized average transmission rates is quite similar at high E_s/N_0 values.

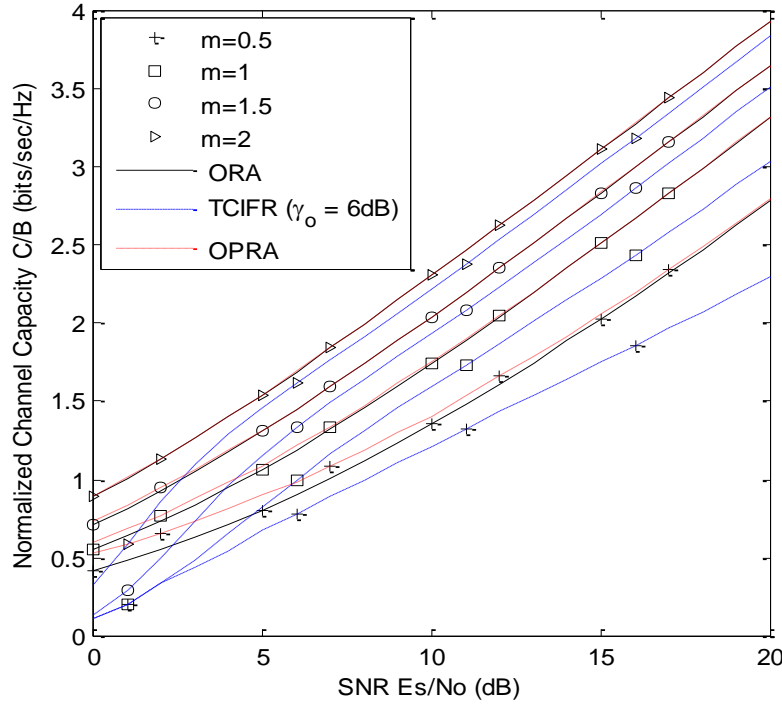


Figure 57 Ergodic capacities of ORA, OPRA and TCIFR policies in an i.i.d Nakagami channel ($N = 1$).

Figure 58 depicts the ergodic capacity of ORA in a Nakagami- m channel with one relay diversity ($N = 1$) in comparison to no relay case ($N = 0$) and for different transmit power assignments. Without any loss of generality, assume that the mean SNRs on different links are given as follows (which takes into account of the relative distances among the cooperating nodes):

$$\Omega_{s,l} = \left(\frac{d_{s,l}}{d_{s,d}} \right)^{-L_p} c \delta_{s,l} E_T / N_o, \quad \Omega_{l,d} = \left(\frac{d_{l,d}}{d_{s,d}} \right)^{-L_p} c \delta_{l,d} E_T / N_o, \quad \text{and} \quad \Omega_{s,d} = \left(\frac{d_{s,d}}{d_{s,d}} \right)^{-L_p} c \delta_{s,d} E_T / N_o, \quad \text{where } c \text{ is}$$

constant that is related to the carrier wavelength (i.e., $c = \left(\frac{\lambda}{4\pi} \right)^2$ for free space path loss),

L_p is the path loss exponent, $\delta_{s,d} = \delta_{s,i} = \frac{P_{s,i}}{P_T}$ while $\delta_{i,d} = (1 - \delta_{s,i}) = \frac{P_{i,d}}{P_T}$ since $\sum \delta_{a,b} = 1$, and

$d_{a,b}$ denotes the distance between link $a - b$. To generate Figure 58, we have arbitrarily chosen $d_{s,l} = d_{l,d} = 500m$, $c = 10^{-2}$, $d_{s,d} = 1000m$ and $L_p = 4$. It is evident that equal power allocation strategy may be reasonable but not optimal in all cases (i.e., optimum power allocation strategy is more beneficial when the channel experience more severe fading). We also observe that the tightness of upper and lower bounds on the ergodic capacity becomes looser as m increases. Comparison between the curves corresponding to the single relay and no relay cases reveal that the optimum power assignment is not strongly influenced by the source-destination link but rather on the link qualities of source-relay and relay-destination links.

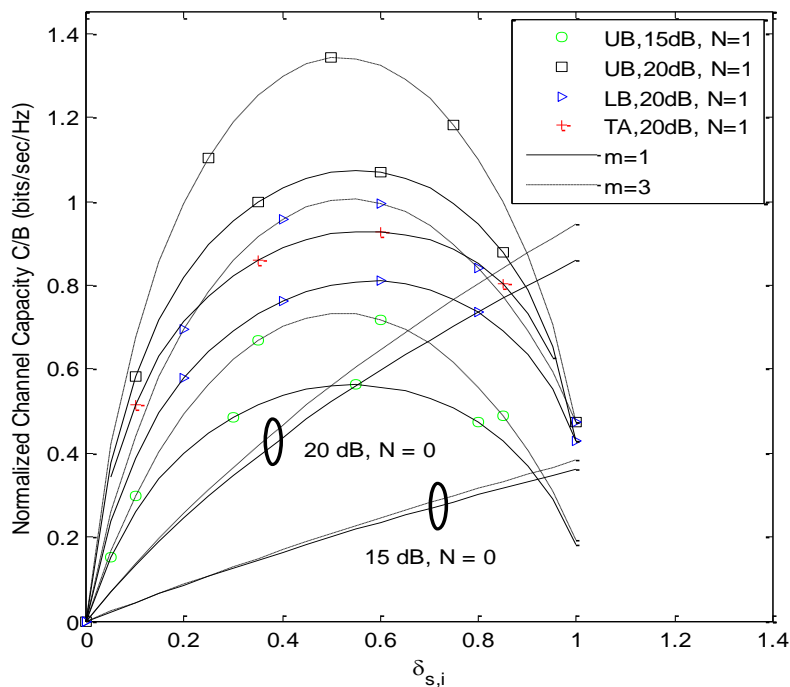


Figure 58 Ergodic capacity of N relays with ORA policy as a function of fixed transmit power assignment $\delta_{s,i}$ in a Nakagami- m channel.

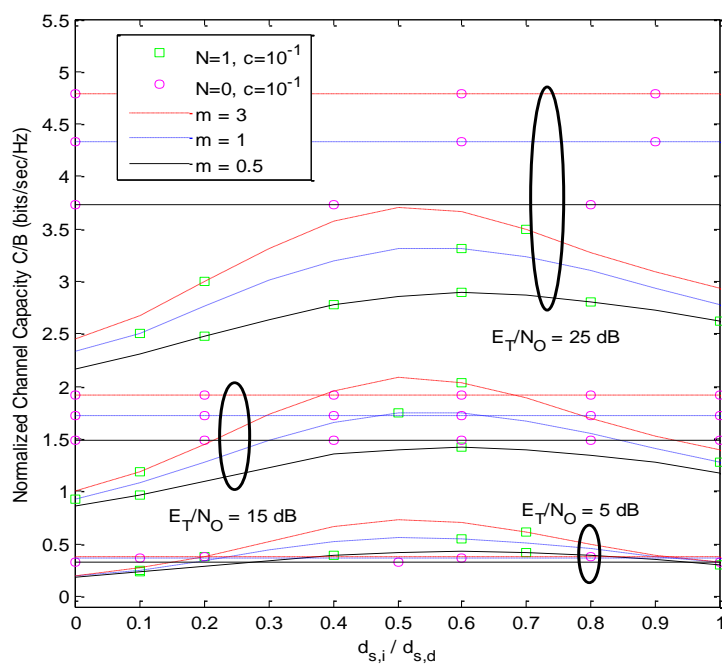


Figure 59a: Ergodic capacity ("Upper Bound Case") of N relays ($N=0, 1$) with ORA policy in a Nakagami- m channel

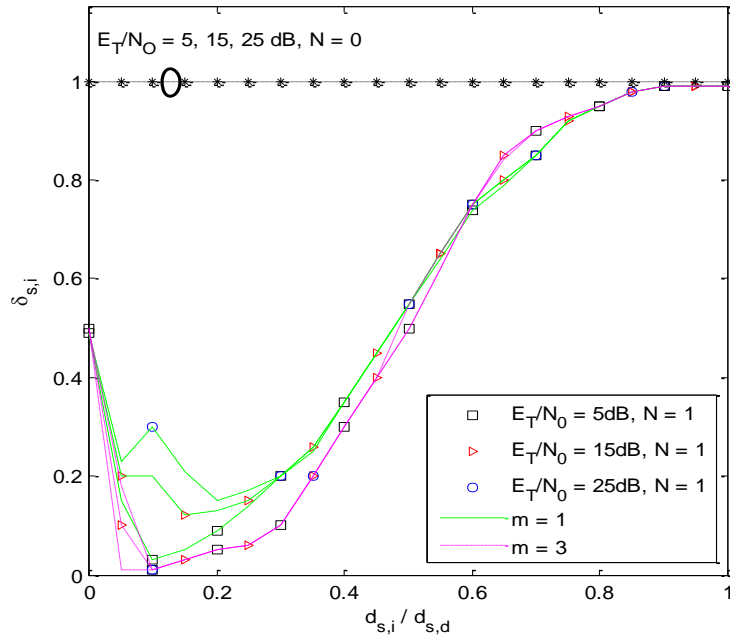


Figure 59b: Different transmit power assignment, $\delta_{s,i}$ (“Upper Bound Case”) of N relays ($N=0, 1$) with ORA policy ($c = 10^{-1}$)

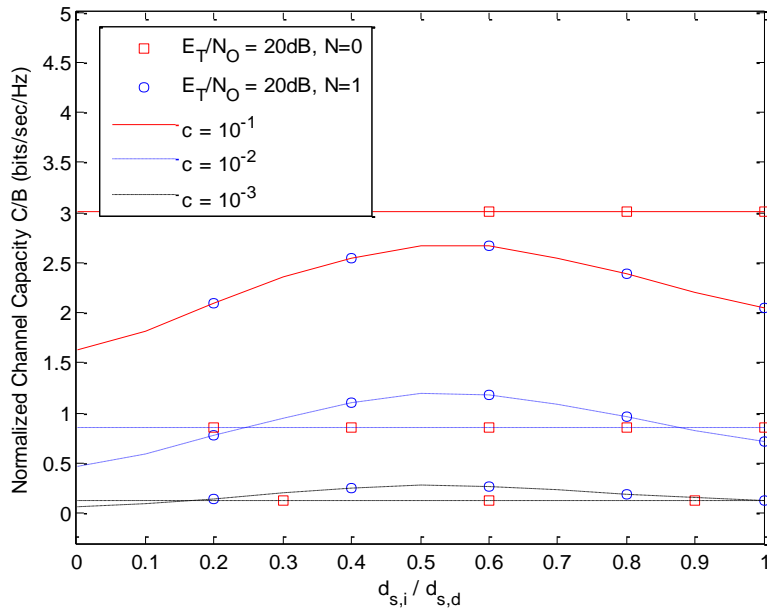


Figure 59c: Ergodic capacity (“Upper Bound” Case) of N relays ($N=0, 1$) with ORA policy in a Nakagami- m ($m=1.5$) fading channel.

Figure 59a shows the Ergodic capacity of ORA policy in Nakagami- m channel as a function of ratio of distances between source to relay and source to destination (i.e., $\frac{d_{s,i}}{d_{s,d}}$), which describe the important scenario of effect of node placement in cooperative

communication. For simplicity, explained here for only one relay case but, this analysis can be easily extended for any number of relays. The mathematical expressions and other parameters are assumed to be same as explained above for Figure 58, except c and the distances. We have arbitrarily chosen values of $d_{s,i}$ varied in the range of 0 - 1000 m with step size 100 m, $c = 10^{-1}$, $d_{s,d} = 1000\text{m}$, and $L_p = 4$. It is observed from the curves that, the position of relay near to the destination (i.e., for the distance ratio above 0.5) gives slightly higher spectral efficiency compared to the values when the relay near to the source (i.e., for the distance ratio below 0.5). Furthermore, comparison between curves corresponding to the no relay and single relay cases disclose that, for lower and medium values of fix transmitted power (i.e., $E_T/N_0 = 5\text{ dB}$ and 15 dB respectively), the role of relay is very important for chosen value of distance ratio, to achieve the higher spectral efficiency. But for the higher values of E_T/N_0 (i.e., 25 dB and above) it is obvious that the use of relay is not worth.

Figure 59b shows the Different transmit power assignment, $\delta_{s,i}$ (for “Upper Bound Case”) of a cooperative relay network consisting of N relays ($N=0, 1$) with ORA policy as a function of ratio of distances, $\frac{d_{s,i}}{d_{s,d}}$ in a Nakagami- m channel with same parameters as mentioned for Figure 59a. Furthermore, comparison between curves corresponding to the no relay case and single relay cases reveal that, with the single relay case, the distribution of transmit power is distance based. Which, indicates that, single relay case utilize optimum power compared to the no relay case.

Figure 59c describe the related scenario as explained in Figure 59a but, for the different values of c with Nakagami fading channel ($m=1.5$). It is observed from the curve that, as the distance between the source and destination increases (i.e., c increases from 10^{-1} to 10^{-3}) relay plays an important role to achieve desirable spectral efficiency. Finally From Figure(s) 59a, b and c, we can firmly conclude that, the spectral efficiency is not only a function of: (i) E_T/N_0 , (ii) fix transmit power assignment $\delta_{s,i}$; and (iii) fading index m , but also affected by the position of relay (node placement) with respect to source and destination and distance between source and destination (i.e., function of c).

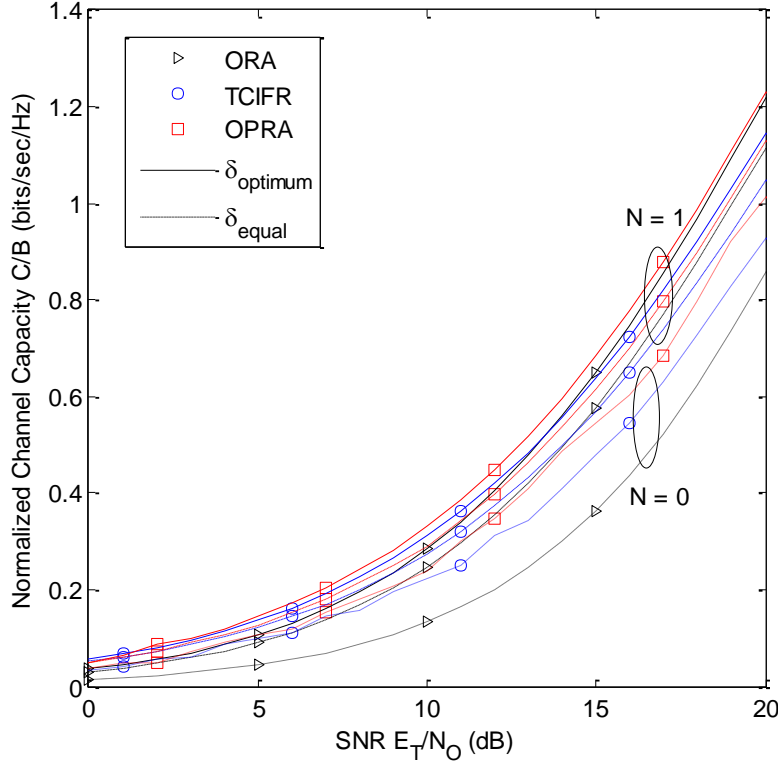


Figure 60 Ergodic capacities (“Upper Bound Case”) in an i.n.d Nakagami-m fading channel with N relays ($N=0, 1$)

Figure 60 shows the comparison of ergodic capacities of three distinct source adaptive transmission policies in an i.n.d Nakagami-m fading channel consisting of N relays ($N=0, 1$) with the following values of fading index on the corresponding link : $m_{s,1}=4, m_{1,d}=2, m_{s,d}=1$,

$m_{a,b}$, denotes the fading index between link $a-b$. Without any loss of generality, assume that the mean SNRs on different links are given as follows (which takes into account of the relative distances among the cooperating nodes):

$$\Omega_{s,1} = \left(\frac{d_{s,1}}{d_{s,d}} \right)^{-L_p} c \delta_{s,1} E_T / N_o, \Omega_{1,d} = \left(\frac{d_{1,d}}{d_{s,d}} \right)^{-L_p} c \delta_{1,d} E_T / N_o, \text{ and } \Omega_{s,d} = \left(\frac{d_{s,d}}{d_{s,d}} \right)^{-L_p} c \delta_{s,d} E_T / N_o, \text{ where } c \text{ is}$$

constant that is related to the carrier wavelength (i.e., $c = \left(\frac{\lambda}{4\pi} \right)^2$ for free space path loss),

L_p is the path loss exponent, $\delta_{s,d} = \delta_{s,i} = \frac{P_{s,i}}{P_T}$ while $\delta_{i,d} = (1 - \delta_{s,i}) = \frac{P_{i,d}}{P_T}$ since $\sum \delta_{a,b} = 1$, and

$d_{a,b}$ denotes the distance between link $a-b$. To generate Figure 60, we have arbitrarily chosen $d_{s,1} = 400m, d_{1,d} = 600m, c = 10^{-2}, d_{s,d} = 1000m$ and $L_p = 4$. To plot for $N = 1$, the parameters chosen are $\delta_{s,1} = 0.28, \delta_{1,d} = 0.72, \delta_{s,d} = 0.28$ for optimal power allocation strategy ($\delta_{optimum}$) and $\delta_{s,1} = 0.5, \delta_{1,d} = 0.5, \delta_{s,d} = 0.5$, for equal power allocation strategy (δ_{equal}). For the curves of $N=0$, the value of $\delta_{s,d} = 1$ for ORA, OPRA and TCIFR.

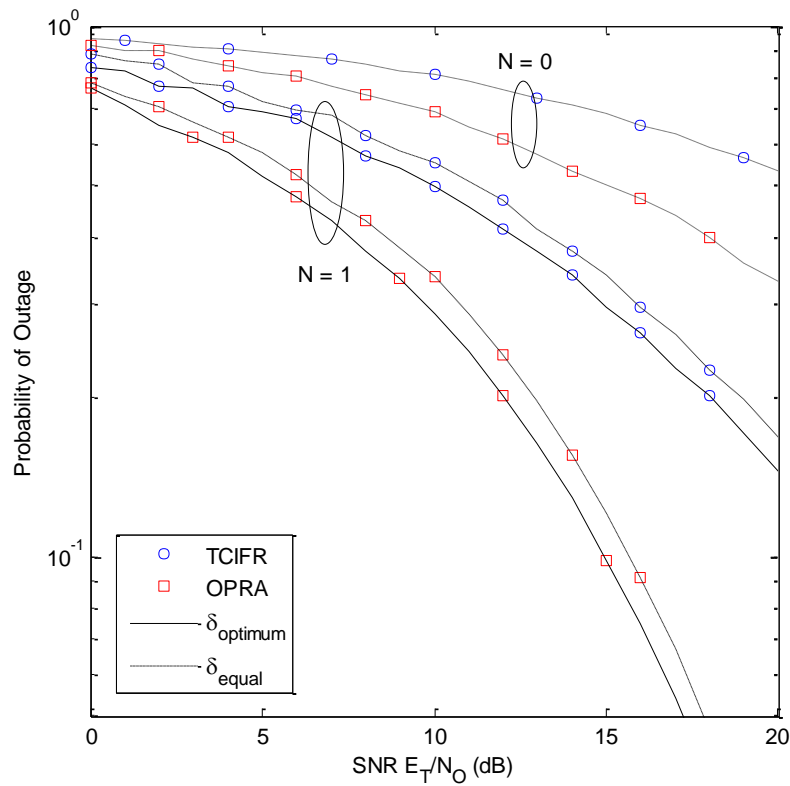


Figure 61a Outage probability (“Upper Bound Case”) of source adaptive policies in an i.n.d Nakagami-m fading channel with N relays (N=0, 1).

Figure 61a shows the comparison of probability of outage for the OPRA and TCIFR policies. Figure 61a is plotted based on the cut-off SNR values from Figure 61b for OPRA and TCIFR as a function of SNR. In the case of TCIFR, the optimal cut-off SNR is selected, which maximize the capacity at the cost of increased probability of outage.

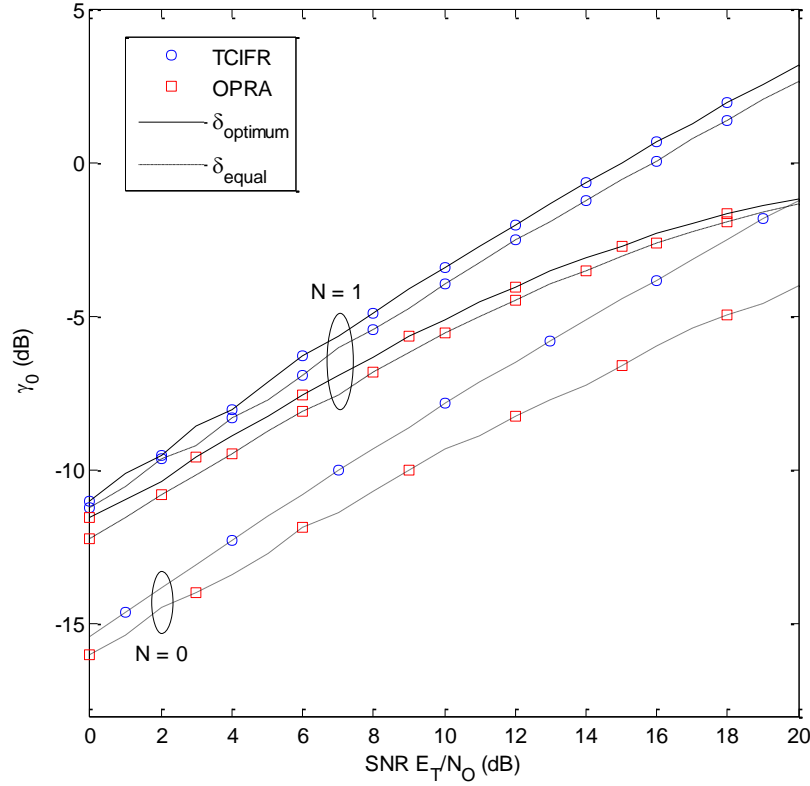


Figure 61b Cut-off SNR (γ_0) versus SNR E_s/N_0 (“Upper Bound Case”) in an i.i.d Nakagami-m fading channel

3.5.2 Adaptive M-QAM Modulation in Cooperative Relay Networks

In this sub-section, we have presented numerical results for the outage probability, achievable spectral efficiency, and BER analysis for cooperative systems with adaptive M-QAM transmissions under Nakagami-m channels. For all the numerical results, the system model as in [52] is considered. However, the authors in [52] have presented the above numerical results of cooperative relaying in i.i.d Rayleigh fading, but their framework does not lend itself to the analysis of the “tight-approximation” case or generalized to other fading channels (i.e., Nakagami-m or Rice), whereas our framework encapsulates all these cases in a unified way. In our analysis all the numerical results for the case of non-i.i.d. Nakagami-m fading, are obtained with two relays. The average SNR of the links are chosen arbitrarily as in [52] such that it represents a realistic model of a practical cooperative communication system. They are as follows: $\Omega_{s,1} = E_s/N_0$, $\Omega_{s,2} = 0.8E_s/N_0$, $\Omega_{1,d} = 0.3E_s/N_0$, $\Omega_{2,d} = 0.56E_s/N_0$, and $\Omega_{s,d} = 0.2E_s/N_0$.

In all of the non i.i.d cases, the fading index over each link is set as per the following 3 Cases with 2 relay diversity only.

Case 1: $m_{s,1}=1, m_{s,2}=1, m_{1,d}=1, m_{2,d}=1, m_{s,d}=1$, Case 2: $m_{s,1}=4, m_{s,2}=4, m_{1,d}=2, m_{2,d}=2, m_{s,d}=1$;

Case 3: $m_{s,1}=2, m_{s,2}=2, m_{1,d}=4, m_{2,d}=4, m_{s,d}=1$. where $m_{a,b}$, denotes the fading index between link a - b .

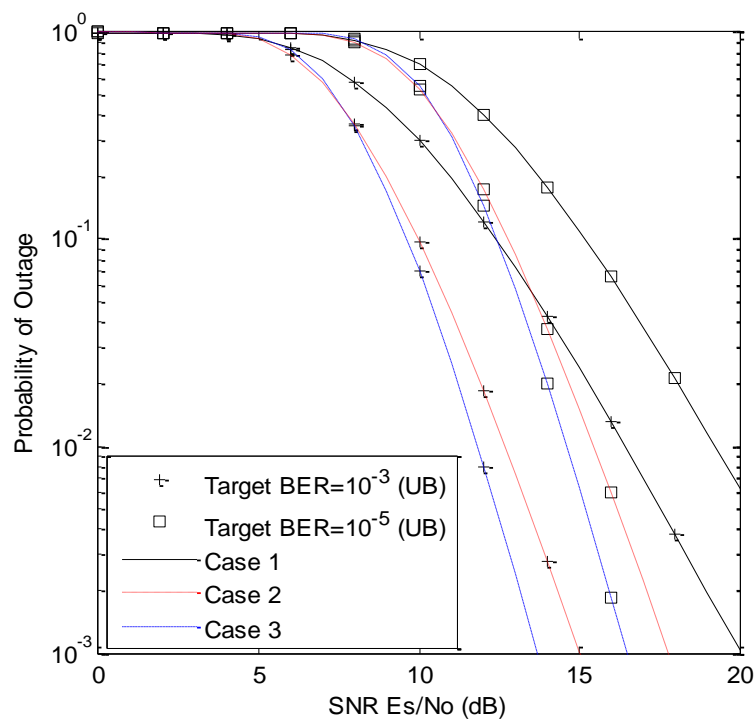


Figure 62 Outage probability of i.i.d. Nakagami-m fading channels with upper bound for 2 relay diversity.

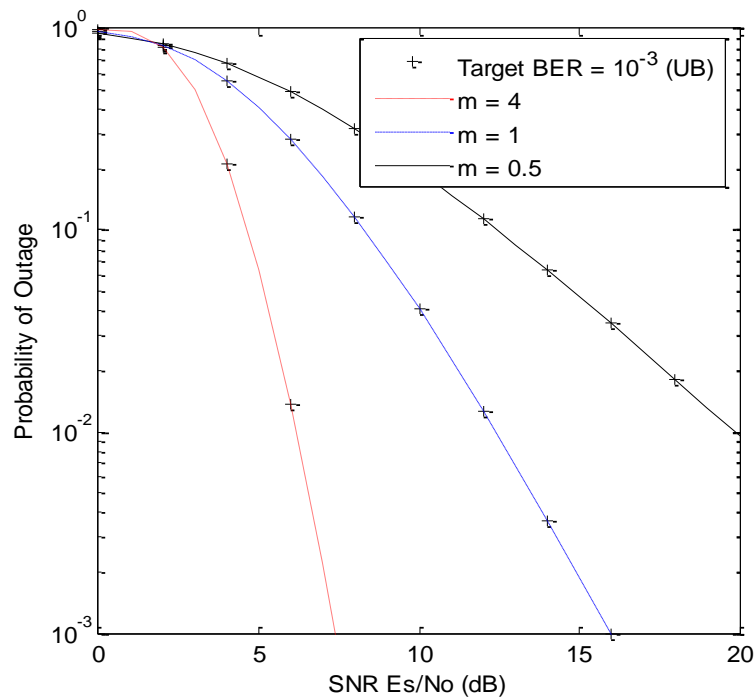


Figure 63 Outage probability of i.i.d. Nakagami-m fading channels for upper bound for 2 relay diversity.

Figure 62 show the probability of outage computed using the numerical method for inversion of Laplace transform (17). To validate the analysis, Case 1 exactly matches the results in [52] for non-i.i.d Rayleigh fading case. From figure, it can be concluded that, for a given different average SNRs over each relay link, links with better channel conditions (as a result of higher Nakagami fading index) performs better than the case; where all the links have the same fading index with $m=1$. It is also observed that outage probability performance of case 3 is better than that of case 2. Case 3 has higher fading index in the relay-to-destination links, compared to source-to-destination links. The average SNR on the relay-to-destination link are lower than the source-to-relay link. This suggests that a cooperative communication system can perform better with links, that experience better fading channels, even under lower average received SNRs. This means that transmitter power allocation over the relays can be adjusted to reduce power consumption by knowing the channel quality. If the fading index in the Nakagami- m channel is known to be higher than the power allocated to the transmitter, in those links it may be reduced without affecting the overall performance of the system.

Figure 63 depicts the outage probability of i.i.d. Nakagami- m fading channels for upper bound along with special case: Rayleigh fading channel (i.e., $m=1$), there is a surprising effect of increasing the Nakagami- m fading index on all the links. The average SNRs over each link is kept the same. The fading index over all the links are also kept the same. The diversity is provided with 2 relays. It can be observed that with increasing fading index, the outage probability performance improves drastically at higher SNRs (SNR > 10). The above analysis also concludes that, our analysis, is viable for the non-integer fading index Nakagami- m (i.e., $m=0.5, 1.5$ or 2.5) values.

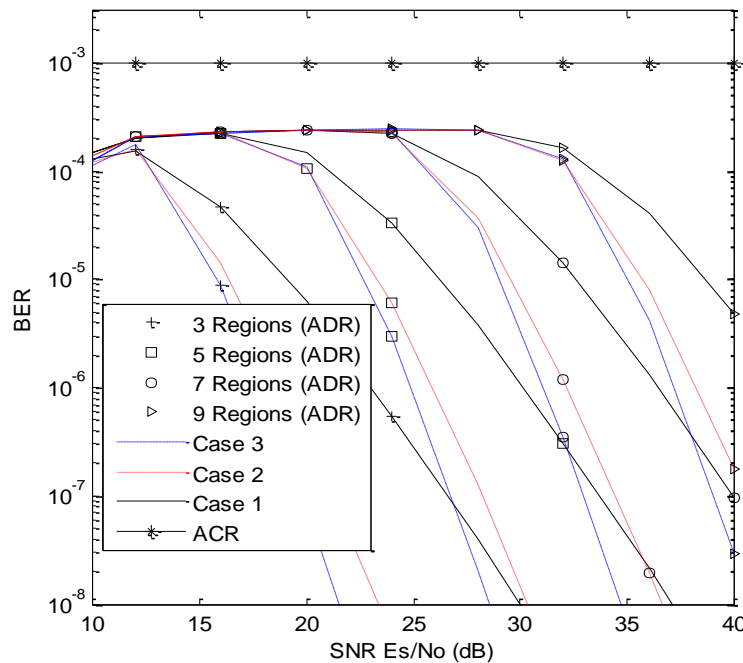


Figure 64 Average BER for i.n.d. Nakagami- m fading channel for upper bound for 2 relay diversity.

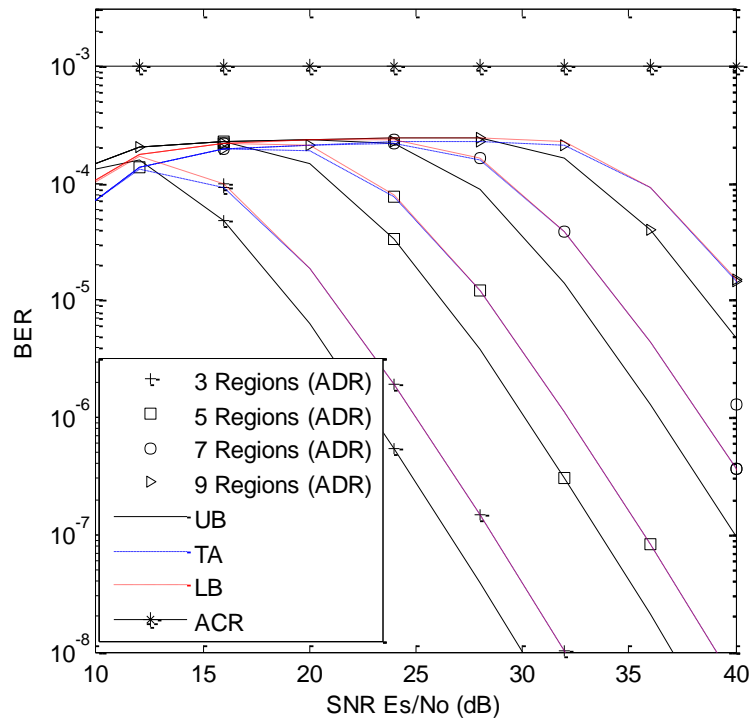


Figure 65 Average BER for i.n.d. Rayleigh fading channel for 2 relay diversity.

Figure 64 shows the BER computed using (23). The performance under case 2 and 3 are better than case 1. Performance under case 3 is slightly better than case 2. This is because a higher fading index in links with lower average SNRs improves end-to-end reliability. For links with higher SNR improvement in channel condition does not affect reliability significantly.

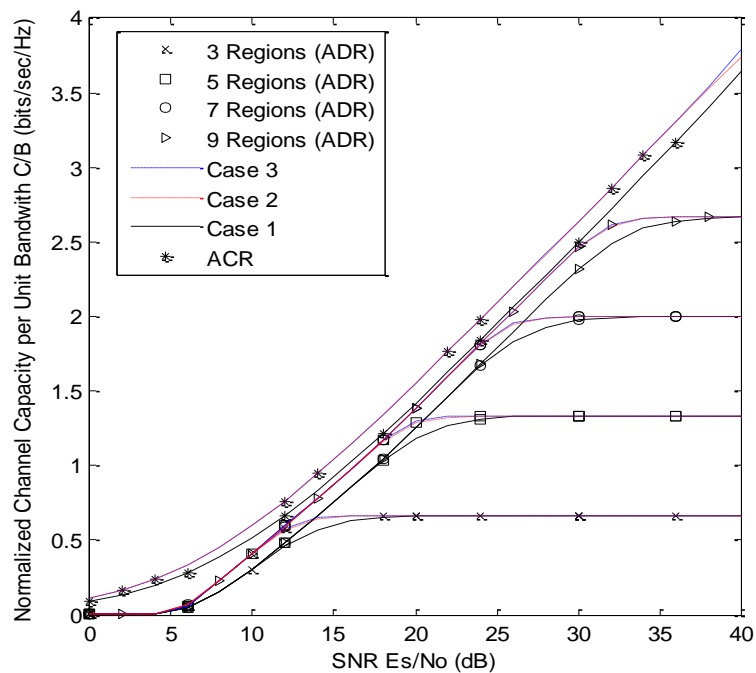


Figure 66 Achievable rates for i.n.d. Nakagami-m fading channels for 2 relay diversity.

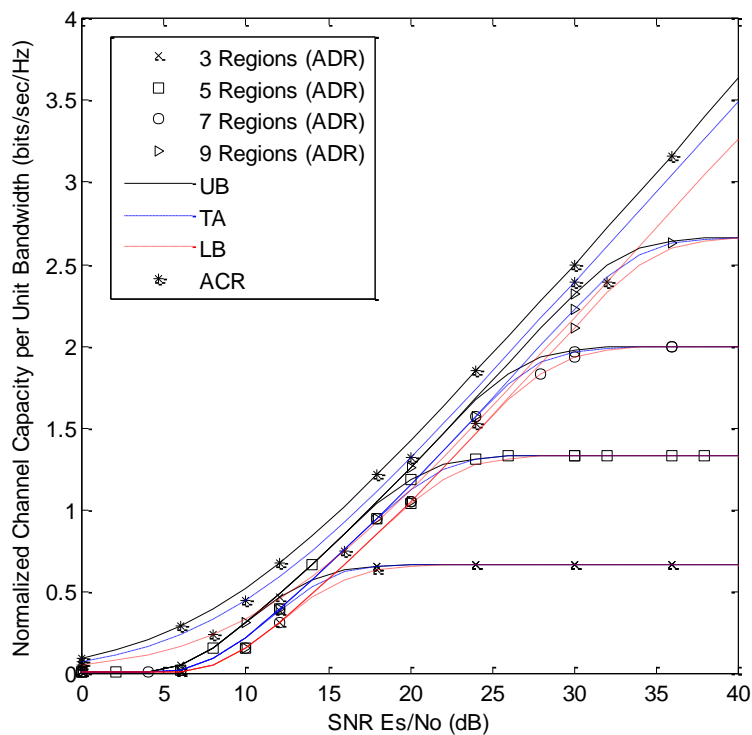


Figure 67 Achievable rates for i.n.d. Rayleigh fading channels for 2 relay diversity.

Figure 66 shows the achievable spectral efficiency for adaptive continuous rate M-QAM (19) and adaptive discrete rate M-QAM (20) systems for target BER level of $BER_0 = 10^{-3}$ for the non i.i.d fading model. The plot shows the comparison of three cases of Nakagami-m fading channels, along with the special case $m=1$ (Rayleigh fading). It can be observed that the capacity per unit bandwidth for case 2 and case 3 are higher than case 1. The difference in capacities between case 2 and 3 are negligible. Hence channel conditions do not have much effect on capacity. Adaptive discrete rate M-QAM suffers at least an additional 1.5 dB compared to the spectral efficiency of Adaptive continuous rate M-QAM.

4. CONCLUSIONS

In section 2.2, our investigation showed that although CS measurements may be performed with no apriori knowledge of the signal (other than the fact that the signal is sparse or compressible in some basis), the reconstruction error can depend strongly on the choice of basis function. Hence a means of determining the best sparsifying basis function is necessary. We were able to demonstrate that it is possible to predict the best sparsifying bases for a compressive sensing based signal reconstruction. Our investigation revealed that the Gini index and the l_0 -norm measure are a good predictor of best sparsifying bases. In section 2.3, we demonstrated that the CS based NYFR is capable of detecting signals in the spectrum without *a priori* information. The NYFR being a CS based system requires sub-Nyquist sampling rate to detect available signals in the spectrum. The accuracy of the prediction is very high and the automatic detection algorithm which was developed eliminates error associated with visual analyzes of the result and can aid in automated and embedded system. The system is robust both in additive Gaussian noise as well as in fading environment. Results obtained from our discussion in section 2.4 reveals that it is possible to determine the available spectrum bandwidth through Compressive Sensing based signal reconstruction. This is achievable with or without noisy channel condition. With the help of the results of section 2.2, we are able to determine the best sparsifying basis for achieving good reconstruction of the Power spectrum density is the Haar wavelet. The PSD is analogous to a block type signal and as such the Haar wavelet is the best sparsifying basis for use. Compressive sensing based signal reconstruction is scalable in its application. One can quickly scan through a broad frequency spectrum to determine availability and subsequently narrow down on a section of interest. We have investigated the effect of sample size, compressive sensing algorithm; on the quality of results as well as the effect of different channel noise. Our results reveal that OMP performs better with higher sampling size as compared to BP and LASSO. LASSO algorithm performs better as the sample size is reducing. However since the goal is to determine the occupied frequency band, our investigation revealed that the CS based method can efficiently reconstruct the PSD for adequate detection of occupied frequency band.

In section 3, we have derived the ergodic capacity bounds for non-regenerative (amplify-and-forward) cooperative relay networks with adaptive source transmission. Unlike previous related studies, we advocate a simple numerical procedure for unified analysis of ergodic capacity of source adaptive relay networks in a myriad of fading

environments. Specifically, two unified approaches have been presented for the ergodic capacity analysis over generalized fading channels: (i) moment generating function method; (ii) cumulative distribution function method. This framework allows us to gain insights as to how fade distributions and dissimilar fading statistics across the diversity paths affect the maximum mean achievable transmission rate, without imposing any restrictions on the fading parameters. Even for the specific case of Rayleigh fading, our framework lends itself to the development of a much tighter bound for the ergodic capacity of source adaptive relay networks. Moreover, our analytical framework also facilitates the investigation of optimal power assignment and node placement (i.e., position of relay with respect to source and destination) in cooperative relay networks. The three adaptive source transmission techniques considered were: (i) optimal simultaneous power and rate adaptation (OPRA); (ii) constant power with optimal rate adaptation (ORA); (iii) truncated channel inversion with fixed rate (TCIFR). Asymptotic bound is also derived which shows that constant power with optimal rate adaptation policy provides roughly the same ergodic capacity as the optimal simultaneous power and rate adaptation policy at high SNR regime. The gap between ORA and OPRA curves also becomes negligible as the channel experience less severe fading (higher fading index m). The new framework may be employed to solve a number of open research problems in adaptive relay networks such as node selection strategies, ergodic capacity analysis of decoding-and-forward relaying, resource allocation schemes among cooperating nodes, and the efficacy of distributed space-time coding.

5. REFERENCES

- [1] E. Candes, J Romberg and T. Tao, "Robust Uncertainty Principles: Exact Signal Reconstruction from Highly Incomplete Frequency Information," *IEEE Transactions on Information Theory*, Vol. 52, pp. 489 – 509, February 2006.
- [2] David Donoho, "Compressed Sensing," *IEEE Transactions on Information Theory*, Vol. 52, Issue 4, pp. 1289 – 1306, April 2006.
- [3] Stephane Mallat, and Zhifeng Zhang, "Matching Pursuits with Time Frequencies Dictionaries," *IEEE Transactions on Signal Processing*, Vol. 41, Issue 12, pp. 3397 – 3415, December 1993.
- [4] Jarvis Haupt, Robert Nowak, "Signal Reconstruction from Noisy Random Projections," *IEEE Transactions on Information Theory*, Vol. 52, Issue 9, pp. 4036 – 4048, September 2006.
- [5] Emmanuel Candès, "Compressive Sampling," *Proceedings of International Congress of Mathematics*, Madrid, Spain, pp. 1433-1452, 2006.
- [6] Stephane Mallat, *A Wavelet Tour of Signal Processing*, Academic press, 1999.
- [7] Cajetan M. Akujuobi, Olusegun Odejide and Gerald Fudge, "Development of Wavelet Based Signal Detection and Measurement Algorithm," *Proceedings of ASEE 6th Global Colloquium on Engineering. Education*, Istanbul, Turkey, pp. 567-576, Oct. 1-4, 2007.
- [8] Olusegun Odejide, Cajetan Akujuobi, Annamalai Annamalai, and Gerald Fudge, "Signal and Modulation Type detection using Wavelet Transform", *IEEE World Congress on Computer Science and Information Engineering*, Los Angeles/Anaheim, Vol. I, pp 457-460, March 31-April 2, 2009.
- [9] Davidson, K. R., Szarek, S. J., "Local Operator Theory, Random Matrices and Banach Spaces," In *Handbook of the Geometry of Banach Spaces* (ed. By W. B. Johnson, J. Lindenstrauss), Vol. I, North-Holland, Amsterdam, pp. 317–366, 2001.
- [10] Szarek, S. J., "Condition Numbers of Random Matrices," *Journal of. Complexity*, Vol. 7, pp. 131–149, 1991.
- [11] E. Candes and T. Tao, "Near-optimal Signal Recovery from Random Projections and Universal Encoding Strategies," *IEEE Transactions on Information Theory*, Vol. 52, Issue 12, pp. 5406–5425, December 2006.
- [12] Rudelson, M., Vershynin, R., "Sparse Reconstruction by Convex Relaxation: Fourier and Gaussian Measurements," *40th Annual Conference on Information Sciences and Systems*, pp. 207-212, 2006.
- [13] T. T. Do, T. D. Tran, and L. Gan, 'Fast Compressive Sampling with Structurally Random Matrices', *Proceedings of International Conference on Acoustics, Speech and Signal Processing (ICASSP)*, pp. 3369– 3372, May 2008.
- [14] David L. Donoho, Yaakov Tsaig, Iddo Drori, and Jean-Luc Starck, " Sparse Solution of Underdetermined Linear Equations by Stagewise Orthogonal Matching Pursuit," *Extension of compressed sensing, Signal processing*, 86(3): 549-571, March 2006
- [15] D. L. Donoho, "Sparse Components of Images and Optimal Atomic Decomposition," *Constructive Approximation*, Vol. 17, pp. 353–382, 2001.

- [16] J. Karvanen and A. Cichoki, "Measuring Sparseness of Noisy Signals," *4th International Symposium on Independent Component Analysis and Blind Signal Separation (ICA2003)*, Nara, Japan, pp. 125-130, April 2003.
- [17] N. Roman, D. Wang, and G. J. Brown, "Speech Segregation Based on Sound Localization," *Journal of the Acoustical Society of America*, pp. 2236-2252, 2003.
- [18] A. Hyvarinen and P. Hoyer, "A Two-layer Sparse Coding Model Learns Simple and Complex Cell Receptive Fields and Topography from Natural Images," *Vision Research*, Vol. 41(18), pp. 2413-2423, 2001.
- [19] N. Saito, B. M. Larson, and B. Benichou, "Sparsity vs Statistical Independence from Best-basis Viewpoint," *Proceedings of SPIE 4119, Wavelet Applications in Signal and Image Processing VIII*, pp. 474-486, 2000.
- [20] Scott Rickard, "Sparse Sources are Separated Sources," *Proceedings of the 16th annual European Signal Processing Conference*, Florence, Italy, 2006.
- [21] H. Dalton, "The Measurement of the Inequality of Incomes," *The Economic Journal*, Vol. 30, pp. 348-361, September, 1920.
- [22] A. Ghasemi, E. S. Sousa, "Spectrum sensing in cognitive radio networks: requirements, challenges and design trade-offs," *IEEE Comms. Magazine*, 32-39 (2008).
- [23] I. F. Akyildiz, W.-Y. Lee, M.C. Vuran, S. Mohanty, "Next generation/dynamic spectrum access/cognitive radio wireless networks: a survey", *Elsevier Comp. Netw. J.*, 50(13) 2127-2159 (2006)
- [24] K. N. Steadmann, A.D. Rose, T. T. N. Nguyen, "Dynamic spectrum sharing detectors," *Proc. 2nd IEEE Symp. New Frontiers in Dynamic Spectrum Access Networks*, Dublin, Ireland, 276-282 (2007).
- [25] M. Ghoszi, F. Marx, M. Dohler, J. Palicot, "Cyclostationarity based test for detection of vacant frequency bands," *Proc. 1st Int. Conf. Cognitive Radio Oriented Wireless Networks and Communications*, Mykonos, Greece, 1-5 (2006).
- [26] R. H. Walden, "Analog-to-digital converter survey and analysis," *IEEE Journal on Selected Areas in Communications*, 539-550 (1999).
- [27] Dennis Healy and David Brady, "Compression at the physical interface," *IEEE Signal Processing Magazine*, 67-71 (2008).
- [28] Zhuizhuan Yu, S. Hoyos, B.M. Sadler, "Mixed-signal parallel compressed sensing and reception for cognitive radio," *ICASSP*, 3861-3864 (2008).
- [29] G. Fudge, R. Bland, M. Chivers, S. Ravindran, J. Haupt, P. Pace, "A Nyquist folding analog-to-information receiver," *Proceedings of the 42nd Asilomar Conference on Signals, Systems, and Computers*, (2008).
- [30] J. A. Tropp, M. B. Wakin, M. F. Duarte, D. Baron, R. G. Baraniuk, "Random filters for compressive sampling and reconstruction," *ICASSP* (2006).
- [31] S. Kirolos, J. Laska, M. Wakin, M. Duarte, D. Baron, T. Ragheb, Y. Massoud, R. Baraniuk, "Analog-to-information conversion via random demodulation," (2006).
- [32] J. Laska, S. Kirolos, Y. Massoud, R. Baraniuk, A. Gilbert, M. Iwen, M. Strauss, "Random sampling for analog-to-information conversion of wideband signals," *IEEE Dallas / CAS Workshop on Design, Applications, Integration and Software* (2006)
- [33] L. Cohen, "Time-frequency distributions - A review," *Proc. IEEE* 77, 941-981 (1989).

- [34] L. Cohen, [Time-Frequency Analysis], Prentice Hall, Englewood Cliffs, New Jersey, (1995).
- [35] Olusegun Odejide, Cajetan Akujuobi, Annamalai Annamalai, and Gerald Fudge, "Application of analytic wavelet transform for signal detection in Nyquist Folding Analog-to-Information Receiver," *IEEE International Conference on Communication*, 1 - 5(2009).
- [36] Z. Tian and G. B. Giannakis, "Compressed Sensing for Wideband Cognitive Radio," *Proc. IEEE Int. Conf. on Acoustics Speech and Signal Processing (ICASSP)*, 1357-1360 (2007).
- [37] N. Laneman, D. Tse, and G. Wornell, "Cooperative Diversity in Wireless Networks: Efficient Protocols and Outage Behaviour," *IEEE Trans. Information Theory*, vol. 50, Dec.2004, pp. 3062-3080.
- [38] R. Palat, A. Annamalai and J. Reed, "Accurate Bit Error Rate Analysis of Bandlimited Cooperative OSTBC Networks under Timing Synchronization Errors," *IEEE Trans. Vehicular Technology*, vol. 58, June 2009, pp. 2191-2200.
- [39] A. Madsen and J. Zhang, "Capacity Bounds and Power Allocation for Wireless Relay Channels," *IEEE Trans. Information Theory*, vol. 51, pp. 2020-2040, June 2005.
- [40] D. Gunduz and E. Erkip, "Opportunistic Cooperation by Dynamic Resource Allocation," *IEEE Trans. Wireless Communications*, pp. 1446-1454, Apr. 2007.
- [41] Y. Zhao, R. Adve, and T. Lim, "Improving Amplify-and-Forward Relay Networks: Optimal Power Allocation versus Selection," *IEEE Trans. Wireless Comm.*, pp. 3114-3123, Aug. 2007.
- [42] A. Goldsmith and P. Varaiya, "Capacity of Fading Channels with Channel Side Information," *IEEE Trans. Information Theory*, vol. 43, pp. 1986-1992, Nov. 1997.
- [43] T. Nechiporenko, K. Phan, C. Tellambura, and H. Nguyen, "Capacity of Rayleigh Fading Cooperative Systems under Adaptive Transmission," *IEEE Trans. Wireless Communications*, vol. 8, April 2009, pp. 1626-1631.
- [44] G. Farhadi and N. Beaulieu, "On the Ergodic Capacity of Multi-Hop Wireless Relaying Systems," *IEEE Trans. Wireless Communications*, vol. 8, May 2009, pp. 2286-2291.
- [45] M. Alouini, A. Abdi, and M. Kaveh, "Sum of Gamma variates and Performance of Wireless Communication Systems over Nakagami Fading Channels," *IEEE Trans. Vehicular Technology*, pp. 1471-1480, Nov. 2001.
- [46] M. Di Renzo, F. Graziosi, and F. Santucci, "Ei-Transform: A Useful and General Framework for Channel Capacity Analysis over Fading Channels," *Proc. IEEE Sarnoff Symposium*, April 2009, Princeton, NJ.
- [47] R. Palat, A. Annamalai, and J. Reed, "An Efficient Method for Evaluating Information Outage Probability and Ergodic Capacity of OSTBC Systems," *IEEE Communications Letters*, March 2008, pp. 191-193.
- [48] I. S. Gradshteyn and I. M. Ryzhik, *Table of Integrals, Series and Products*, Academic Press, 1995.
- [49] C. Gunther, "Comment on 'Estimate of Channel Capacity in Rayleigh Fading Environment'," *IEEE Trans. Vehicular Technology*, vol. 45, May 1996, pp. 401-403.

- [50] Weifeng, Su., Ahmed K. S., & Ray Liu K. J. (2008). Cooperative Communication Protocols in Wireless Networks: Performance Analysis and Optimum Power Allocation. *Springer link Wireless Personal Communication*, vol. 44 pp. 181-217.
- [51] M. Hasna and M. Alouini "Harmonic Mean and End-to-End Performance of Transmission System with Relays," *IEEE Trans. Communications*, vol. 52, no.1, Jan 2004, pp. 130-135.
- [52] T. Nechiporenko, K. T. Phan, C. Tellambura, and H. H. Nguyen, "Performance analysis of adaptive M-QAM for Rayleigh fading cooperative systems," in Proc. IEEE ICC, May 2008, pp.3393–3399.
- [53] A. J. Goldsmith and S.G. Chua, "Variable-rate variable-power MQAM for fading channels," *IEEE Trans. Commun.*, vol. 45, pp. 1218–1230, Oct. 1997.
- [54] A. J. Goldsmith and S.G. Chua,"Adaptive coded modulation for fading channels," *IEEE Trans. Commun.*, vol. 46, no. 5, pp. 595-602, May 1998.
- [55] M. S. Alouini and A. Goldsmith, "Adaptive M-QAM modulation over Nakagami fading channels," in Proc. Communication Theory Mini- Conference (CTMC-VI) in conjunction with IEEE Global Commun. Conf. (GLOBECOM'97), Phoenix, AZ, Nov. 1997, pp. 218–223.
- [56] M.S. Alouini and A. J. Goldsmith, "Adaptive modulation over Nakagami fading channels," *Wireless Personal Comm.*, vol. 13, pp. 119–143, 2000.

APPENDIX A

In this appendix, a sketch of our derivation for an “exponential-type” integral representation of $\ln \gamma$ is provided. Such a representation will facilitate the averaging problem that typically encountered in capacity analysis over fading channels, and therefore leads to a unified approach for calculating the ergodic capacity of CANs in a myriad of fading environments and relaying strategies.

Utilizing [12, eq. (1.512.2)], we have

$$\ln \gamma = 2 \sum_{k=1, \text{ odd}}^{\infty} \frac{1}{k} \left(\frac{\gamma-1}{\gamma+1} \right)^k = 2 \sum_{k=1, \text{ odd}}^{\infty} \frac{1}{k} (y)^k, \quad \gamma > 0 \quad (\text{A.1})$$

where $y = \frac{\gamma-1}{\gamma+1}$. Substituting $y^k = \frac{1}{\Gamma(k)} \int_0^{\infty} x^{k-1} e^{-x/y} dx$ [12, eq. (3.381.4)] into (A.1), we obtain

$$\ln \gamma = 2 \sum_{k=1, \text{ odd}}^{\infty} \frac{1}{k} \left(\frac{1}{\Gamma(k)} \int_0^{\infty} x^{k-1} e^{-x/y} dx \right) = 2 \int_0^{\infty} e^{-x/y} \left(\sum_{k=1, \text{ odd}}^{\infty} \frac{1}{k!} x^{k-1} \right) dx \quad (\text{A.2})$$

Recognizing that $\frac{1}{x} \sinh x = \frac{e^x - e^{-x}}{x} = \sum_{k=1, \text{ odd}}^{\infty} \frac{1}{k!} x^{k-1}$ [12, Eq. (1.411.2)], (A.2) can be re-stated as

$$\ln \gamma = 2 \int_0^{\infty} e^{-x/y} \frac{1}{x} (e^x - e^{-x}) e^{-x \left(\frac{\gamma+1}{\gamma-1} \right)} dx \quad (\text{A.3})$$

Finally using variable substitution $x = z(\gamma-1)$, $dz = \frac{dx}{\gamma-1}$, we arrive at (A.4) after some routine algebraic manipulations:

$$\ln \gamma = \int_0^{\infty} \frac{1}{z} [e^{-2z} - e^{-2zy}] dz, \quad \gamma > 0 \quad (\text{A.4})$$

It is also obvious that

$$\ln(\gamma+1) = \int_0^{\infty} \frac{e^{-2z}}{z} [1 - e^{-2zy}] dz, \quad \gamma > -1 \quad (\text{A.5})$$

APPENDIX B

Let $\phi_X(s) = \int_0^{\infty} e^{-sx} f_X(x) dx$ and $\Phi_X(j\omega) = \int_0^{\infty} e^{j\omega x} f_X(x) dx$ denote the moment generating function (MGF) and the characteristic function (CHF) of random variable $X \geq 0$, respectively. In this case, the CHF is related to the MGF as $\Phi_X(j\omega) = \phi_X(-j\omega)$. The PDF of X (may be expressed as an inverse Fourier transform of its CHF) is given by

$$f_X(x) = \frac{1}{2\pi} \int_{-\infty}^{\infty} \phi_X(-j\omega) e^{-j\omega x} d\omega \quad (\text{B.1})$$

Let us express the CHF of random variable X in its polar form $\Phi_X(j\omega) = |\Phi_X(j\omega)| e^{j\theta(\omega)}$. Hence (B.1) may be re-stated as

$$\begin{aligned}
f_x(x) &= \frac{1}{2\pi} \int_0^\infty \Phi_x(j\omega) e^{-j\omega x} d\omega + \frac{1}{2\pi} \int_{-\infty}^0 \Phi_x(j\omega) e^{-j\omega x} d\omega \\
&= \frac{1}{2\pi} \int_0^\infty [\Phi_x(j\omega) e^{-j\omega x} + \Phi_x(-j\omega) e^{j\omega x}] d\omega \\
&= \frac{1}{\pi} \int_0^\infty |\Phi_x(j\omega)| \left[\frac{e^{j(\theta(\omega) - \omega x)} + e^{-j(\theta(\omega) - \omega x)}}{2} \right] d\omega \\
&= \frac{1}{\pi} \int_0^\infty |\Phi_x(j\omega)| \cos(\theta(\omega) - \omega x) d\omega \\
&= \frac{1}{\pi} \int_0^\infty \text{Re}\{\Phi_x(j\omega) e^{-j\omega x}\} d\omega
\end{aligned} \tag{B.2}$$

and consequently, we can simplify the integral

$$\begin{aligned}
\int_1^\infty \gamma^{-1} f_\gamma(\gamma_0 \gamma) d\gamma &= \frac{1}{\pi} \int_0^\infty \text{Re} \left\{ \Phi_\gamma(j\omega) \left(\int_1^\infty \frac{e^{-j\omega \gamma_0 \gamma}}{\gamma} d\gamma \right) \right\} d\omega, \\
&= -\frac{1}{\pi} \int_0^\infty \text{Re} \{ \phi_\gamma(-j\omega) \text{Ei}(-j\omega \gamma_0) \} d\omega
\end{aligned} \tag{B.3}$$

with the aid of identities (B.2) and (D.1).

APPENDIX C

It is important to note that the knowledge of marginal MGF of end-to-end SNR may be required while evaluating the ergodic capacity with OPRA policy (e.g., see (20)). However, this quantity is generally not available in closed-form. But if a closed-form expression for the MGF $\phi_\gamma(\cdot)$ is available, we may then use Abate's fixed Talbot method (multi-precision Laplace inversion formula) for computing the desired marginal MGF efficiently as highlighted below.

Let us define an auxiliary function $f_{\hat{\gamma}}(x) = e^{-\beta x} f_\gamma(x)$. Hence,

$$\phi_\gamma(\beta, \alpha) = \int_\alpha^\infty e^{-\beta \gamma} f_\gamma(\gamma) d\gamma = F_{\hat{\gamma}}(\infty) - F_{\hat{\gamma}}(\alpha) \tag{C.1}$$

where $F_{\hat{\gamma}}(y) = \int_0^y f_{\hat{\gamma}}(x) dx = \int_0^y e^{-\beta x} f_\gamma(x) dx$. It is obvious that

$$F_{\hat{\gamma}}(\infty) = \int_0^\infty e^{-\beta x} f_\gamma(x) dx = \phi_\gamma(0) = \phi_\gamma(\beta) \tag{C.2}$$

Furthermore, we have

$$\begin{aligned}
\phi_{\hat{\gamma}}(s) &= \int_0^\infty e^{-sx} f_{\hat{\gamma}}(x) dx, \\
&= \int_0^\infty e^{-(s+\beta)x} f_\gamma(x) dx, \\
&= \phi_\gamma(s + \beta)
\end{aligned} \tag{C.3}$$

Substituting (C.2) and (13) (in conjunction with (C.3)) into (C.1), we arrive at a numerically efficient method for evaluating the required marginal MGF in a generalized fading channel.

APPENDIX D

While the exponential-integral $Ei(x)$ is usually defined for real $x < 0$, in the following we will show that this function is also well-defined even if its argument is purely imaginary. This is particularly interesting because our unified expression for the ergodic capacity of CANs with truncated channel inversion policy and the transcendental equation for computing the optimal cut-off SNR γ_0 for the OPRA policy are expressed in terms of $Ei(-jc)$ where $c > 0$ is real.

Letting $q = \pm jy$ (y is real), we have

$$Ei(-q) = -\int_q^\infty \frac{e^{-t}}{t} dt = -\int_1^\infty \frac{e^{-qt}}{t} dt \quad (D.1)$$

Utilizing the Euler identity $e^{\pm jy} = \cos(y) \pm j\sin(y)$, (D.1) can be re-stated in terms of the more familiar sine-integral and cosine-integral, viz.,

$$\begin{aligned} Ei(\pm jy) &= -\int_1^\infty \frac{1}{t} \cos(yt) dt \pm \int_1^\infty \frac{1}{t} \sin(yt) dt, \\ &= ci(y) \mp jsi(y) \end{aligned} \quad (D.2)$$

with the aid of [12, Eqs. (3.721.2) and (3.721.3)]. The sine-integral and cosine-integral may be computed efficiently via rapidly converging series representations:

$$si(y) = -\int_y^\infty \frac{\sin(t)}{t} dt = -\frac{\pi}{2} + \sum_{k=1}^\infty \frac{(-1)^{k+1} y^{2k-1}}{(2k-1)(2k-1)!}, \quad (D.3)$$

$$ci(y) = -\int_y^\infty \frac{\cos(t)}{t} dt = C + \ln(y) + \sum_{k=1}^\infty \frac{(-1)^k y^{2k}}{(2k)(2k)!}, \quad (D.4)$$

where $C = 0.57721566\dots$ is Euler's constant. Alternatively, the quantity $Ei(-jc)$ can be evaluated in MATLAB using command line “`cosint(c) - j(-pi/2 + sinint(c))`”.

PUBLICATIONS

The following articles have been accepted for publication/published as a result of this funded research effort and collaborative research with AFRL:

- A. Annamalai, B. Modi, and R. Palat, "On the Ergodic Capacity of Cooperative Analog Relaying with Source Adaptive Transmission Policies," to appear in the Proc. IEEE Consumer Communications and Networking Conference (CCNC'11), Las Vegas, January 2011.
- A. Annamalai, B. Modi, and R. Palat, "Analysis of Amplify-and-Forward Cooperative Relaying with Adaptive Modulation in Nakagami-m Fading Channels," to appear in the Proc. IEEE Consumer Communications and Networking Conference (CCNC'11), Las Vegas, January 2011.
- J. James, O.Odejide, A. Annamalai and D. Vaman, "Adaptive Multiresolution Modulation for Multimedia Traffic," to appear in the Proc. IEEE Consumer Communications and Networking Conference (CCNC'11), Las Vegas, January 2011.
- A. Annamalai, B. Modi, and R. Palat, "Unified Analysis of Ergodic Capacity of Cooperative Non-Regenerative Relaying with Adaptive Source Transmission Policies," to appear in the Proc. IEEE GLOBECOM Workshop on Heterogeneous, Multi-Hop, Wireless and Mobile Networks (HeterWMN'10), Miami, Dec. 6-10, 2010.
- A. Annamalai, B. Modi, R. Palat and J. Matyjas, "Tight Bounds on the Ergodic Capacity of Cooperative Analog Relaying with Adaptive Source Transmission Techniques" Proc. IEEE Personal, Indoor and Mobile Radio Communications (PIMRC'10), Istanbul, Turkey, Sept. 26-30, 2010.
- Olusegun Odejide, A. Annamalai and C. Akujobi, "Efficacy of Compressive Sensing for Dynamic Spectrum Access," Proc. SPIE Defense, Security, and Sensing Conference, Orlando, April 2010, Vol. 7707, 770706 (2010).
- Olusegun Odejide, A. Annamalai, and C. Akujobi, "Wideband Signal Detection using a Nyquist-Folding Analog-to-Information Receiver in Multipath Fading Environment," Proc. SPIE Defense, Security, and Sensing Conference, Orlando, April 2010, Vol. 7707, 770707 (2010).
- Annamalai, R. Palat, and J. Matyjas, "Estimating Ergodic Capacity of Cooperative Analog Relaying under Different Adaptive Source Transmission Techniques," Proc. IEEE Sarnoff Symposium, Princeton, April 12 - 14, 2010.
- R. Palat, A. Annamalai, and J. Reed, "Energy Efficiency in Selective Decode-and-Forward Cooperative Communications," Proc. IEEE Sarnoff Symposium, Princeton, April 12-14, 2010.
- A. Annamalai and Q. Zhao, "Further Results on Optimum Selection Diversity for BPSK Signals in Nakagami-m Fading," Proc. IEEE Consumer Communications and Networking Conference (CCNC'10), Las Vegas, January 9-12, 2010.
- A. Annamalai, J. Matyjas and M. Medley, "Integrated Design of Hierarchical Modulation and Retransmission Diversity for Multimedia Wireless Networks," Proc. IEEE Consumer Communications and Networking Conference (CCNC'10), Las Vegas, January 9-12, 2010.

- O. Odejide, C. Akujuobi, A. Annamalai and G. Fudge, "Joint-Design of Source-Channel Coding for Compressive Sampling Systems," Proc. IEEE Consumer Communications and Networking Conference, Las Vegas, January 9-12, 2010.
- A. Bhatnagar, S. Kumar, A. Annamalai and A. Janarthanan, "A Multilevel Unequal Protection Scheme for Robust H.264/AVC Video Transmission over Wireless Channels," Proc. IEEE Military Communications Conference (MILCOM'09), Boston, October 18-21, 2009.
- O. Odejide, C. Akujuobi, A. Annamalai and G. Fudge, "Application of Analytic Wavelet Transform for Signal Detection in Nyquist-Folding Analog-to-Information Receiver," Proc. IEEE International Conference on Communications (ICC'09), Dresden, June 14-18, 2009.
- O. Odejide, C. Akujuobi, A. Annamalai and G. Fudge, "Determination of Best Sparsifying Basis for Compressive Sampling," *International Review of Electrical Engineering*, pp. 327 – 335, April 2009.
- O. Odejide, C. Akujuobi, A. Annamalai, and G. Fudge, "Signal Modulation Type Detection using Wavelet Transform," Proc. IEEE World Congress on Computer Science and Information Engineering, Los Angeles, March 31-April 02, 2009, pp. 457-460.
- A. Annamalai, D. Vaman, J. Matyjas, and M. Medley, "Cross-Layer Design of Embedded Modulation and ARQ Protocol for Prioritized Packet Transmission in Wireless Networks," Proc. IEEE Consumer Communications and Networking Conference (CCNC'09), Las Vegas, January 10-13, 2009.
- A. Annamalai, C. Tellambura, and J. Matyjas, "A New Twist on the Generalized Marcum Q-Function with Fractional-Order and Its Applications," Proc. IEEE Consumer Communications and Networking Conference (CCNC'09), Las Vegas, January 10-13, 2009.
- A. Annamalai, D. Vaman, J. Matyjas, and M. Medley, "Joint-Design of Multiresolution Modulation and ARQ Protocol for Prioritized Packet Transmission in Wireless Ad-Hoc Networks," Proc. IEEE Military Communications Conference (MILCOM'2008), San Diego, November 17-19, 2008.

LIST OF ABBREVIATIONS

ACR	Adaptive Continuous Rate
ADC	Analog to Digital Converter
ADR	Adaptive Discrete Rate
AWGN	Additive White Gaussian Noise
BP	Basis Pursuit
CAN	Cooperative Airborne Network
CDF	Cumulative Distribution Function
CIFR	Channel Inversion with Fixed Rate
CR	Cognitive Radio
CRN	Cognitive radio Network
CS	Compressive Sampling or Compressed Sensing
CSI	Channel Side Information
DCT	Discrete Cosine Transform
DSA	Dynamic Spectrum Access
DWT	Discrete Wavelet Transform
FDMA	Frequency Division Multiple Access
FFT	Fast Fourier Transform
GP	Gradient Pursuit
i.i.d	independent, identical and distributive
i.n.d	independent, non-identical and distributive
LAR	Least Angle Regression
LASSO	Least Absolute shrinkage Selection Operator

LB	Lower Bound
LOS	Line of Sight
MIMO	Multiple-Input-Multiple Output
MP	Matching Pursuit
MRC	Maximum-Ratio Combining
MGF	Moment Generating Function
NLOS	Non Line of Sight
NYFR	Nyquist Folding Analog-to-Information Receiver
OMP	Orthogonal Matching Pursuit
ORA	Optimal Rate Adaptation
OPRA	Optimal joint Power and Rate Adaptation
PDF	Probability Density Function
PSD	Power Spectral Density
PU	Primary User
QAM	Quadrature Amplitude Modulation
RF	Radio frequency
RMSE	Root Mean Square Error
SNR	Signal to Noise Ratio
StOMP	Stagewise Orthogonal Matching Pursuit
SU	Secondary User
TA	Tight Approximation
TDMA	Time Division Multiple Access
TCIFR	Fixed Rate with Truncated Channel Inversion

TOMP	Tree Orthogonal Matching Pursuit
UB	Upper Bound
WGN	White Gaussian Noise